2015-09

Rapid slewing of flexible space structures

Wojdakowski, Steven W.

Monterey, California: Naval Postgraduate School

NAVAL POSTGRADUATE SCHOOL

MONTEREY, CALIFORNIA

THESIS

RAPID SLEWING OF FLEXIBLE SPACE STRUCTURES

by

Steven W. Wojdakowski

September 2015

Thesis Advisor:	Mark Karpenko
Second Reader:	I. Michael Ross

THIS PAGE INTENTIONALLY LEFT BLANK

REPORT DOCUMENTATION PAGE

Form Approved OMB No. 0704-0188

1. AGENCY USE ONLY *(Leave blank)*	**2. REPORT DATE** September 2015	**3. REPORT TYPE AND DATES COVERED** Master's Thesis

4. TITLE AND SUBTITLE
RAPID SLEWING OF FLEXIBLE SPACE STRUCTURES

5. FUNDING NUMBERS

6. AUTHOR(S) Wojdakowski, Steven W.

7. PERFORMING ORGANIZATION NAME(S) AND ADDRESS(ES)
Naval Postgraduate School
Monterey, CA 93943-5000

8. PERFORMING ORGANIZATION REPORT NUMBER

9. SPONSORING /MONITORING AGENCY NAME(S) AND ADDRESS(ES)
N/A

10. SPONSORING/MONITORING AGENCY REPORT NUMBER

11. SUPPLEMENTARY NOTES The views expressed in this thesis are those of the author and do not reflect the official policy or position of the Department of Defense or the U.S. Government. IRB Protocol number ____N/A____.

12a. DISTRIBUTION / AVAILABILITY STATEMENT
Approved for public release; distribution is unlimited

12b. DISTRIBUTION CODE

13. ABSTRACT (maximum 200 words)

This thesis addresses the problem of computing rapid slew maneuvers for a spacecraft antenna mounted on a double-axis gimbal with elastic joints. The performance of the system can be enhanced by designing antenna maneuvers in which the flexible effects are properly constrained, thus reducing the load on the spacecraft control system. The motion of a mass-spring-damper system is shown to be analogous to a spacecraft antenna slew with linear dynamics. This model is extended to a nonlinear double-gimbal mechanism with flexible joints, which better represents real spacecraft antenna dynamics. Rather than increase maneuver times to control flexible motion, this thesis presents optimal solutions that decrease maneuver times while allowing designers to easily constrain flexibility. Since it is impossible to recast the nonlinear system into a modal representation, an innovative approach is used to map the nonlinear dynamics into a linear system with a fictitious force. The fictitious force captures the effects of the nonlinearities so the vibrational motion can be constrained for a time-optimal slew. It is shown that by constructing an appropriate optimal control problem, the maneuver time for a flexible DGM can be decreased by approximately 42% compared to a conventional computed torque control solution.

14. SUBJECT TERMS
multibody systems, modal analysis, optimal control, satellite, flexible space structure, maneuver design, slew design

15. NUMBER OF PAGES
151

16. PRICE CODE

17. SECURITY CLASSIFICATION OF REPORT	**18. SECURITY CLASSIFICATION OF THIS PAGE**	**19. SECURITY CLASSIFICATION OF ABSTRACT**	**20. LIMITATION OF ABSTRACT**
Unclassified	Unclassified	Unclassified	UU

NSN 7540-01-280-5500

Standard Form 298 (Rev. 2-89)
Prescribed by ANSI Std. 239-18

THIS PAGE INTENTIONALLY LEFT BLANK

Approved for public release; distribution is unlimited

RAPID SLEWING OF FLEXIBLE SPACE STRUCTURES

Steven W. Wojdakowski
Major, United States Army
B.S., United States Military Academy, 2002

Submitted in partial fulfillment of the
requirements for the degree of

MASTER OF SCIENCE IN ASTRONAUTICAL ENGINEERING

from the

NAVAL POSTGRADUATE SCHOOL
September 2015

Author: Steven W. Wojdakowski

Approved by: Mark Karpenko
Thesis Advisor

I. Michael Ross
Second Reader

Garth V. Hobson
Chair, Department of Mechanical and Aerospace Engineering

THIS PAGE INTENTIONALLY LEFT BLANK

ABSTRACT

This thesis addresses the problem of computing rapid slew maneuvers for a spacecraft antenna mounted on a double-axis gimbal with elastic joints. The performance of the system can be enhanced by designing antenna maneuvers in which the flexible effects are properly constrained, thus reducing the load on the spacecraft control system. The motion of a mass-spring-damper system is shown to be analogous to a spacecraft antenna slew with linear dynamics. This model is extended to a nonlinear double-gimbal mechanism with flexible joints, which better represents real spacecraft antenna dynamics. Rather than increase maneuver times to control flexible motion, this thesis presents optimal solutions that decrease maneuver times while allowing designers to easily constrain flexibility. Since it is impossible to recast the nonlinear system into a modal representation, an innovative approach is used to map the nonlinear dynamics into a linear system with a fictitious force. The fictitious force captures the effects of the nonlinearities so the vibrational motion can be constrained for a time-optimal slew. It is shown that by constructing an appropriate optimal control problem, the maneuver time for a flexible DGM can be decreased by approximately 42% compared to a conventional computed torque control solution.

THIS PAGE INTENTIONALLY LEFT BLANK

TABLE OF CONTENTS

LIST OF FIGURES

THIS PAGE INTENTIONALLY LEFT BLANK

LIST OF TABLES

THIS PAGE INTENTIONALLY LEFT BLANK

LIST OF ACRONYMS AND ABBREVIATIONS

$\mathbb{C}$	Set of complex numbers
$\mathbb{R}$	Set of real numbers
DGM	Double-gimbal mechanism
DOF	Degrees of freedom
FRF	Frequency response function
IRF	Impulse response function
NASA	National Aeronautics and Space Administration
PD	Proportional-derivative
PID	Proportional-integral-derivative
TDRS	Tracking and data relay satellite

THIS PAGE INTENTIONALLY LEFT BLANK

ACKNOWLEDGEMENTS

I would like to thank my advisors, Dr. Karpenko and Dr. Ross, for their unwavering patience and confidence in me. I also want to thank my parents for teaching me to strive for success, my wife, Stacie, for being my rock, and my son, Henry—you can do anything.

THIS PAGE INTENTIONALLY LEFT BLANK

I. INTRODUCTION

NASA established the Tracking and Data Relay Satellite (TDRS) program in 1973 to provide continuous global services to critical missions in low-earth orbit while minimizing reliance on international ground stations. Since the first launch in 1983, NASA has commissioned and operated 11 TDRS in space (a twelfth satellite was destroyed in the Space Shuttle Challenger explosion in 1986) [1]. The current constellation consists of nine active TDRS at various positions in geosynchronous orbit (see Figure 1) to provide global relay capability for NASA missions such as the International Space Station and the Hubble Space Telescope [2].

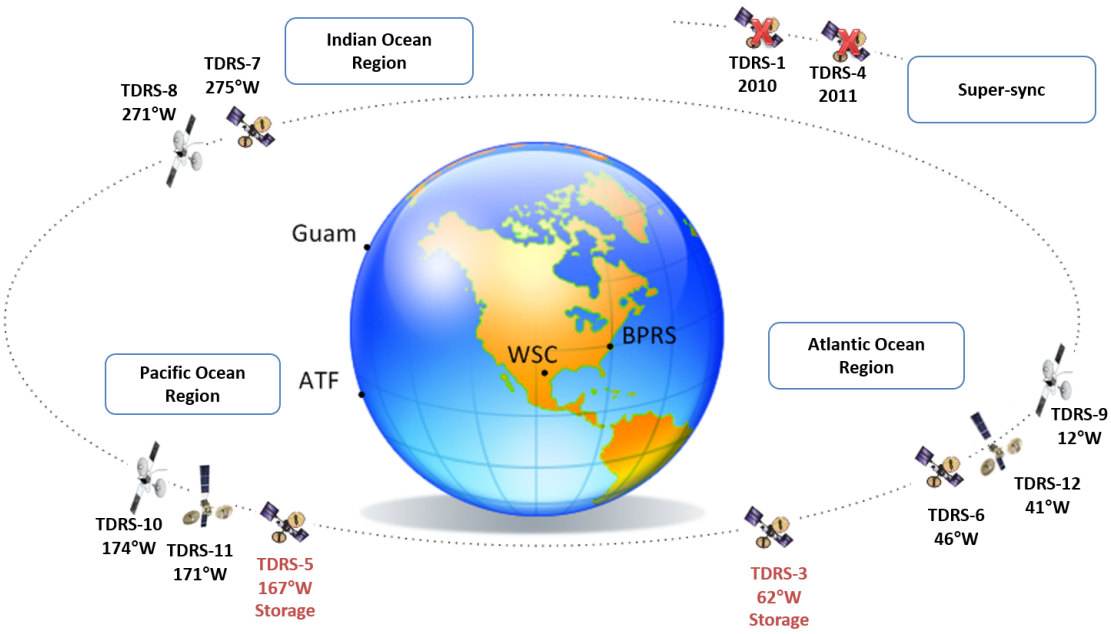

Figure 1. TDRS constellation, from [2].

Each TDRS uses multiple antennas to service its customers in an effort to reduce the number of satellites needed on orbit. Third-generation TDRS, for example, host a payload with two single access antennas and a multiple access antenna with 32 transmit and 15 receive elements [2]. Each of these antennas

must be steerable in order to service moving targets in the low-earth orbital regime. This presents a unique problem in satellite design and operation in that the TDRS attitude control system must continuously accommodate the effects of slewing multiple antennas in order to maintain its orientation and minimize the associated disturbances on the spacecraft bus and other payloads. The actuators controlling the antenna gimbals must supply appropriate levels of torque to slew the antenna at a desired rate in addition to regulating flexible effects and mitigating pointing errors caused by the motion of other appendages. These functions are accomplished using various control modes. However, for slews, maneuvers are typically done slowly to avoid exciting the flexible modes of the satellite structures. In contrast, the spacecraft operators endeavor to maximize the utility of the TDRS by servicing as many customers as the control system will allow. Thus, the TDRS program faces a difficult problem in that demand for access is high and availability is limited due to the capabilities of the various satellite control systems [3].

A. CONTROL METHODS FOR A FLEXIBLE STRUCTURE

Several methods exist to enhance antenna control to increase user throughput. The antenna can be modeled as a manipulator arm connected to a controlling body through joints with some defined range of motion. The conventional method of computed torque control incorporates a simple approach for controlling the motion of such an arm [4]. A proportional-derivative (PD) or proportional-integral-derivative (PID) feedback controller is common in computed torque control because these feedback laws can provide a near-linear response even for a system with nonlinear multi-body dynamics. A simple double integrator can then be used to model the motion of each joint of the arm for maneuver design. The feedback mechanism allows the controller to track the desired maneuver profiles [4], [5]. This method of simplified maneuver design and implementation, while effective, typically dictates that the system be operated conservatively in order to reduce undesired vibrations in the antenna and other systems on a satellite.

Another method for antenna control applies Pontryagin's principle to develop an optimal control based on the system dynamics and given boundary conditions [6]. Pontryagin's principle was applied in [3] and [5] to find minimum-time solutions to the TDRS antenna-slewing problem. The results show the potential for considerable savings in terms of time and increased customer access.

For simplicity, most models, including the ones in [3], assume all bodies are rigid. Realistically, however, space structures typically exhibit some amount of flexibility. All materials possess physical properties that contribute to their response to forces, specifically impulses. The difficulty, however, lies in how to model this flexibility. Models typically require comparison to actual test results to ensure accuracy. As pointed out in [7], mathematical models help engineers understand the behavior of flexible systems in response to (or in the absence of) external input. These models, however, are usually simplified to avoid nonlinear dynamics because the nonlinearities cause unpredictable behavior, especially in the realm of flexible-body motion. Thus, modeling of flexible effects in mechanical systems is typically linear. This thesis explores the use of one such model to optimize antenna maneuvers while taking advantage of the physical properties of materials.

B. THESIS OBJECTIVES AND SCOPE

A significant challenge in designing control systems is to produce rapid slew maneuvers while minimizing the impact of flexible motion. An antenna must point at its targets with a certain degree of accuracy to ensure link closure and error-free transmission. A rapid slew is ineffective if it causes an antenna to "wobble" off target. Figure 2 provides a simple illustration of this phenomenon. The antenna or ground station must increase power to overcome the inaccuracy and maintain the link. To develop rapid slew maneuvers, the effects of flexibility must be considered. To this end, this thesis explores the concepts of modal analysis by looking at general linear mass-spring-damper systems with two and

three degrees of freedom (DOF). These linear systems are notional approximations of two-axis spacecraft antennas with linear dynamics. Applying modal analysis to these linear systems helps designers to understand and constrain vibrational effects of flexible systems.

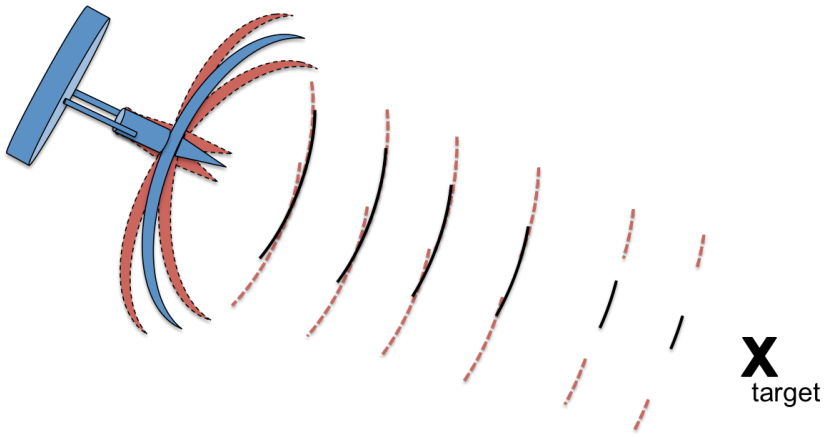

Figure 2. Illustration of a double-axis gimbaled antenna vibrating off target.

Mapping modal analysis concepts to the antenna slew problem is difficult because the dynamics of the antenna motion are nonlinear. Hence, a goal of this thesis is to develop an approach for solving rapid antenna slews for nonlinear antennas that enables the flexible effects to be properly constrained in the modal space.

Chapter II describes the basic concepts in modal analysis and discusses the value of frequency and impulse response functions to understanding the behavior of the flexible system. Two methods for producing a modal model are presented, one in the frequency domain and one in the Laplace domain. Chapter III expands the model to a 3-DOF system, representative of a notional spacecraft with an antenna mounted to a two-axis gimbal. Computed torque control is used to implement conventional slews to illustrate the behavior of flexible-body motion for the baseline system. In Chapter IV, optimal control theory is applied to minimize slew time in the context of several different

approaches for constraining flexible effects. Finally, in Chapter V, these results are applied to a more realistic spacecraft antenna model with nonlinear dynamics. Chapter V presents and illustrates an innovative approach for marrying modal analysis with nonlinear dynamical systems by treating the contributions of the nonlinear terms as a fictitious torque input. It is shown that the “new” system can be analyzed and optimized as a series of linear single-DOF systems but without the deleterious effects of a conventional linearization process. The thesis is brought to a close with some summary remarks and suggestions for future work in Chapter VI.

THIS PAGE INTENTIONALLY LEFT BLANK

II. BACKGROUND ON MODAL ANALYSIS

In modal analysis theory, the analysis of flexible effects is conducted in three phases. First, one must derive the governing equations of motion. That is, one must determine the values that populate the mass, damping, and stiffness matrices for the system. These second-order models are applicable because vibrational amplitudes are usually small and within the linear range of material properties. Second, one must perform a free vibration analysis of the system by setting any external forces to zero. The second phase of analysis produces a set of natural frequencies and damping ratios that lead to a matching set of mode shape vectors. These data are called the modal properties of the flexible system [7]. The mode "shape" is defined as a unique "displacement pattern" [8] that describes the "relative displacements of all parts of the system" [7]. Simply put, a vibration "mode" is one component of a set of ways by which a system oscillates in response to an input. The mode shape describes how each part moves relative to the others. Third, the forced response can be analyzed to understand the behavior of a flexible structure in response to an external input [7], which is of interest in many engineering systems.

The general form of the governing equation of motion for a mass-spring-damper system with n degrees of freedom is

$$\mathbf{M}\ddot{\mathbf{x}}(t)+\mathbf{C}\dot{\mathbf{x}}(t)+\mathbf{K}\mathbf{x}(t)=\mathbf{f}(t) \tag{2.1}$$

where $\mathbf{M}\in\mathbb{R}^{n\text{x}n}$ is a diagonal matrix of mass values, $\mathbf{C}\in\mathbb{R}^{n\text{x}n}$ is a matrix of damping coefficients, $\mathbf{K}\in\mathbb{R}^{n\text{x}n}$ is a matrix of spring constants, $\mathbf{f}(t)\in\mathbb{R}^{n\text{x}1}$ is a vector of external forces acting on each mass, and $\mathbf{x}(t)\in\mathbb{R}^{n\text{x}1}$ is a vector of the displacement of each DOF with respect to its equilibrium position.

Consider the two-mass system shown in Figure 3.

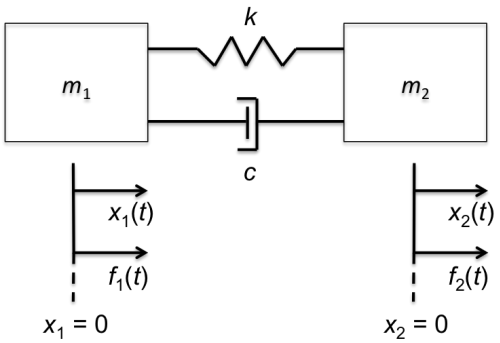

Figure 3. Example mass-spring-damper system with two degrees of freedom.

The schematic describes a 2-DOF system in motion in a frictionless environment. The equations of motion for each mass are

$$f_1 = m_1\ddot{x}_1 + c\dot{x}_1 + kx_1 - c\dot{x}_2 - kx_2 \tag{2.2}$$

$$f_2 = m_2\ddot{x}_2 - c\dot{x}_1 - kx_1 + c\dot{x}_2 + kx_2 \ . \tag{2.3}$$

Using (2.2) and (2.3), the mass, damping, and stiffness matrices in (2.1) may be assembled as $\mathbf{M} = \begin{bmatrix} m_1 & 0 \\ 0 & m_2 \end{bmatrix}$, $\mathbf{C} = \begin{bmatrix} c & -c \\ -c & c \end{bmatrix}$, and $\mathbf{K} = \begin{bmatrix} k & -k \\ -k & k \end{bmatrix}$. The state and force vectors are $\mathbf{x}(t) = \begin{bmatrix} x_1(t) \\ x_2(t) \end{bmatrix}$ and $\mathbf{f}(t) = \begin{bmatrix} f_1(t) \\ f_2(t) \end{bmatrix}$. The 2-DOF system is used in this chapter to illustrate the different ways in which the modal properties of a flexible system can be evaluated. Undamped motion and motion with viscous damping will be studied in the absence and presence of external forces to understand the behavior of the system shown in Figure 3.

A. NATURAL MODAL PROPERTIES

A system without external excitation will exhibit unique modal properties. These properties are referred to as natural modal properties [7]. The natural modal properties of a system describe the behavior of a forced system with

respect to certain frequencies. To find the natural modal properties, first consider the undamped case $(c=0)$ with $\mathbf{f}(t)=\mathbf{0}$:

$$\mathbf{M}\ddot{\mathbf{x}}(t)+\mathbf{K}\mathbf{x}(t)=\mathbf{0}. \tag{2.4}$$

Assume the solution to (2.4) is of the form $\mathbf{x}(t)=\mathbf{X}e^{i\omega t}$, where $\mathbf{X}\in\mathbb{R}^{n\text{x}1}$ denotes a vector of time-independent amplitudes. This leads to $\ddot{\mathbf{x}}(t)=-\omega^2\mathbf{X}e^{i\omega t}$, which shows that the system oscillates following simple harmonic motion with frequencies ω and amplitudes $\mathbf{X}$ [7]. Substituting $\mathbf{x}(t)=\mathbf{X}e^{i\omega t}$ into (2.4) gives the general eigensolution of the form

$$\begin{aligned} -\mathbf{M}\omega^2\mathbf{X}e^{i\omega t}+\mathbf{K}\mathbf{X}e^{i\omega t}&=\mathbf{0} \\ (\mathbf{K}-\lambda_r\mathbf{M})\mathbf{X}_r&=\mathbf{0} \end{aligned} \tag{2.5}$$

where λ_r is the r-th eigenvalue. The corresponding eigenvectors, $\mathbf{X}_r$, are scaled versions of amplitudes $\mathbf{X}$. For a system with n degrees of freedom, $r=1\ldots n$ and $\lambda_r=\omega_r^2$ where ω_r is the r-th undamped natural frequency. Eigenvectors, $\mathbf{v}_r$, for each eigenvalue must be computed to determine the mode shapes of the system. The mode shape describes how the system responds at the corresponding natural frequency, and this shape is dominant at that frequency [9]. In (2.5), $(\mathbf{K}-\lambda_r\mathbf{M})=\mathbf{0}$ must be true; otherwise, $\mathbf{X}_r=\mathbf{0}$, the trivial solution. Let $\mathbf{V}\in\mathbb{C}^{n\text{x}1}$ be a matrix whose columns are eigenvectors such that $\mathbf{V}=\begin{bmatrix}\mathbf{v}_1 & | & \mathbf{v}_2 & | & \cdots & | & \mathbf{v}_n\end{bmatrix}$. Thus, the modal model of a system is completely described by the two eigenmatrices

$$[\lambda_r]=\begin{bmatrix} \lambda_1 & 0 & 0 & 0 \\ 0 & \lambda_2 & 0 & 0 \\ 0 & 0 & \ddots & 0 \\ 0 & 0 & 0 & \lambda_n \end{bmatrix} \tag{2.6}$$

and

$$\mathbf{V}=\begin{bmatrix}\mathbf{v}_1 & | & \mathbf{v}_2 & | & \cdots & | & \mathbf{v}_n\end{bmatrix}. \tag{2.7}$$

For the system given in Figure 3, it is desired to find the eigenvalues. Since this is a system with two degrees of freedom $(n=2)$ there are two modes, two eigenvalues, and two eigenvectors. Applying (2.5) gives

$$\begin{bmatrix} k-\lambda_r m_1 & -k \\ -k & k-\lambda_r m_2 \end{bmatrix} \mathbf{X}_r = \mathbf{0}. \tag{2.8}$$

The eigenvalues, λ_r, may be solved as

$$\det\begin{bmatrix} k-\lambda_r m_1 & -k \\ -k & k-\lambda_r m_2 \end{bmatrix} = m_1 m_2 \lambda_r^2 - (m_1+m_2)k\lambda_r = 0 \tag{2.9}$$

$$\begin{aligned} \lambda_1 &= \omega_1{}^2 = 0 \\ \lambda_2 &= \omega_2{}^2 = \frac{(m_1+m_2)k}{m_1 m_2} \end{aligned}. \tag{2.10}$$

The eigenvectors can be found by substituting the eigenvalues back into (2.8) and solving for $\mathbf{v}_r$ (MATLAB's eig command can do this symbolically). For $\lambda_1 = 0$,

$$\begin{bmatrix} k-\lambda_1 m_1 & -k \\ -k & k-\lambda_1 m_2 \end{bmatrix} \mathbf{v}_1 = \mathbf{0}$$

$$\left[\begin{array}{cc|c} k-\lambda_1 m_1 & -k & 0 \\ -k & k-\lambda_1 m_2 & 0 \end{array}\right] = \left[\begin{array}{cc|c} k & -k & 0 \\ -k & k & 0 \end{array}\right] = \left[\begin{array}{cc|c} 1 & -1 & 0 \\ 0 & 0 & 0 \end{array}\right]$$

$$\begin{aligned} v_{11} - v_{21} &= 0 \\ v_{11} &= v_{21} \\ \mathbf{v}_1 = \alpha \begin{bmatrix} v_{11} \\ v_{21} \end{bmatrix} &= \alpha \begin{bmatrix} v_{11} \\ v_{11} \end{bmatrix} \end{aligned} \tag{2.11}$$

where α is a scaling factor. Choosing $\alpha = \frac{1}{v_{11}}$ gives

$$\mathbf{v}_1 = \begin{bmatrix} 1 \\ 1 \end{bmatrix}. \tag{2.12}$$

For $\lambda_2 = \dfrac{(m_1+m_2)k}{m_1 m_2}$,

$$\begin{bmatrix} k-\lambda_2 m_1 & -k \\ -k & k-\lambda_2 m_2 \end{bmatrix}\mathbf{v}_2 = \mathbf{0}$$

$$\left[\begin{array}{cc|c} k-\lambda_2 m_1 & -k & 0 \\ -k & k-\lambda_2 m_2 & 0 \end{array}\right] \tag{2.13}$$

$$= \left[\begin{array}{cc|c} k-\dfrac{(m_1+m_2)k}{m_1 m_2}m_1 & -k & 0 \\ -k & k-\dfrac{(m_1+m_2)k}{m_1 m_2}m_2 & 0 \end{array}\right]$$

Equation (2.13) gives

$$\left[\begin{array}{cc|c} k-\dfrac{(m_1+m_2)k}{m_2} & -k & 0 \\ -k & k-\dfrac{(m_1+m_2)k}{m_1} & 0 \end{array}\right] = \left[\begin{array}{cc|c} 1 & \dfrac{m_2}{m_1} & 0 \\ 0 & 0 & 0 \end{array}\right]$$

$$v_{12} + \frac{m_2}{m_1}v_{22} = 0 \tag{2.14}$$

$$v_{12} = -\frac{m_2}{m_1}v_{22}$$

$$\mathbf{v}_2 = \alpha\begin{bmatrix} v_{12} \\ v_{22} \end{bmatrix} = \alpha\begin{bmatrix} -\dfrac{m_2}{m_1}v_{22} \\ v_{22} \end{bmatrix}$$

Choosing $\alpha = \frac{1}{v_{22}}$,

$$\mathbf{v}_2 = \begin{bmatrix} -\frac{m_2}{m_1} \\ 1 \end{bmatrix}. \tag{2.15}$$

Therefore,

$$\mathbf{V} = \begin{bmatrix} \mathbf{v}_1 & \mathbf{v}_2 \end{bmatrix} = \begin{bmatrix} 1 & -\frac{m_2}{m_1} \\ 1 & 1 \end{bmatrix}. \tag{2.16}$$

In the first mode (described by the first column of V), both masses move in the same direction with the same amplitude, since both elements of $\mathbf{v}_1$ have the same sign and value. The second mode is characterized by the masses moving in opposite directions due to the negative sign, and the relative amplitude of motion is determined by the ratio of the masses (i.e., $\frac{m_2}{m_1}$ [10]). Because the columns of (2.16) are eigenvectors, they are scalable in amplitude. However, the shapes of the modes, and hence the relative behavior of the two masses, will not change [7]. The undamped free motion of the 2-DOF system is therefore completely described by

$$\left[\lambda_r\right] = \left[\omega_r^2\right] = \begin{bmatrix} 0 & 0 \\ 0 & \frac{(m_1 + m_2)k}{m_1 m_2} \end{bmatrix}$$

and (2.17)

$$\mathbf{V} = \begin{bmatrix} 1 & -\frac{m_2}{m_1} \\ 1 & 1 \end{bmatrix}$$

where $\left[\lambda_r\right]$ denotes a diagonal matrix of eigenvalues and $\left[\omega_r^2\right]$ denotes a diagonal matrix of natural frequencies, and $r = 1 \ldots n$.

B. DIAGONALIZING THE MASS AND STIFFNESS MATRICES

An important property called orthogonality can be used to diagonalize the mass and stiffness matrices in order to transform the original spatial model, which describes the motion in terms of displacements, $\mathbf{x}$, to the so-called modal model, which describes the motion in a new set of coordinates. The transformation relies on the fact that

$$\begin{aligned} \overline{\mathbf{M}} &= \mathbf{V}^T \mathbf{M} \mathbf{V} \\ \overline{\mathbf{K}} &= \mathbf{V}^T \mathbf{K} \mathbf{V} \end{aligned} \tag{2.18}$$

where $\overline{\mathbf{M}} \in \mathbb{R}^{nxn}$ is a diagonal matrix of modal masses, $\bar{m}_r$, and $\overline{\mathbf{K}} \in \mathbb{R}^{nxn}$ is a diagonal matrix of modal stiffness values, $\bar{k}_r$, leading to $\lambda_r = \omega_r^2 = \frac{\bar{k}_r}{\bar{m}_r}$. The modal mass and modal stiffness matrices are not unique. Rather, they are based on how the eigenvectors are scaled. However, the ratio of these quantities is unique and fixed, giving unique modal frequencies, as in (2.17). The modal mass matrix is generally used to normalize the mode shape vectors. The normalized mode shape vectors can then be used to derive useful quantities such as effective mass or effective stiffness [7]. The mass-normalized mode shape vector $\phi_r \in \mathbb{R}^{n\text{x}1}$ is calculated as

$$\phi_r = \frac{\mathbf{v}_r}{\sqrt{\bar{m}_r}} \tag{2.19}$$

such that column matrix $\Phi \in \mathbb{R}^{nxn}$ is

$$\Phi = \left[\begin{array}{c|c|c|c} \phi_1 & \phi_2 & \cdots & \phi_n \end{array} \right] \tag{2.20}$$

which has the property

$$\Phi^{-1} = (\Phi^T)^{-1} \tag{2.21}$$

For the 2-DOF system given in Figure 3, the modal masses and stiffness values are

$$\overline{\mathbf{M}} = \mathbf{V}^T\mathbf{M}\mathbf{V} = \begin{bmatrix} 1 & 1 \\ -\frac{m_2}{m_1} & 1 \end{bmatrix}\begin{bmatrix} m_1 & 0 \\ 0 & m_2 \end{bmatrix}\begin{bmatrix} 1 & -\frac{m_2}{m_1} \\ 1 & 1 \end{bmatrix}$$

$$= \begin{bmatrix} m_1 & m_2 \\ -m_2 & m_2 \end{bmatrix}\begin{bmatrix} 1 & -\frac{m_2}{m_1} \\ 1 & 1 \end{bmatrix} \qquad (2.22)$$

$$= \begin{bmatrix} m_1 + m_2 & 0 \\ 0 & \frac{{m_2}^2}{m_1} + m_2 \end{bmatrix}$$

and

$$\overline{\mathbf{K}} = \mathbf{V}^T\mathbf{K}\mathbf{V} = \begin{bmatrix} 1 & 1 \\ -\frac{m_2}{m_1} & 1 \end{bmatrix}\begin{bmatrix} k & -k \\ -k & k \end{bmatrix}\begin{bmatrix} 1 & -\frac{m_2}{m_1} \\ 1 & 1 \end{bmatrix}$$

$$= \begin{bmatrix} 0 & 0 \\ -k\frac{(m_1+m_2)}{m_1} & k\frac{(m_1+m_2)}{m_1} \end{bmatrix}\begin{bmatrix} 1 & -\frac{m_2}{m_1} \\ 1 & 1 \end{bmatrix} \quad . \qquad (2.23)$$

$$= \begin{bmatrix} 0 & 0 \\ 0 & k\frac{(m_1+m_2)^2}{{m_1}^2} \end{bmatrix}$$

Using (2.22) and (2.23), it is possible to verify that $[\lambda_r] = \overline{\mathbf{M}}^{-1}\overline{\mathbf{K}}$ as required:

$$[\lambda_r] = \overline{\mathbf{M}}^{-1}\overline{\mathbf{K}} = \begin{bmatrix} m_1 + m_2 & 0 \\ 0 & \frac{m_2^2}{m_1} + m_2 \end{bmatrix}^{-1} \begin{bmatrix} 0 & 0 \\ 0 & \frac{k(m_1+m_2)^2}{m_1^2} \end{bmatrix}$$

$$= \begin{bmatrix} \frac{1}{m_1+m_2} & 0 \\ 0 & \frac{m_1}{m_2(m_1+m_2)} \end{bmatrix} \begin{bmatrix} 0 & 0 \\ 0 & \frac{k(m_1+m_2)^2}{m_1^2} \end{bmatrix} \quad . \qquad (2.24)$$

$$= \begin{bmatrix} 0 & 0 \\ 0 & \frac{(m_1+m_2)k}{m_1 m_2} \end{bmatrix}$$

The mass-normalized mode shape vectors are

$$\mathbf{\Phi} = \begin{bmatrix} \phi_1 & | & \phi_2 \end{bmatrix} = \begin{bmatrix} (m_1+m_2)^{-1/2} & -\frac{m_2}{m_1}\left(\frac{m_1}{(m_1+m_2)m_2}\right)^{1/2} \\ (m_1+m_2)^{-1/2} & \left(\frac{m_1}{(m_1+m_2)m_2}\right)^{1/2} \end{bmatrix} . \qquad (2.25)$$

Figure 4 and Figure 5 show an example of the relationship between the mode shapes and the displacement of each mass, for a sample system where $m_1 = m_2 = k = 1$. The values of $\phi_1 = \begin{bmatrix} \frac{\sqrt{2}}{2} & \frac{\sqrt{2}}{2} \end{bmatrix}^T \approx \begin{bmatrix} 0.7071 & 0.7071 \end{bmatrix}^T$ (solid line) mean that each mass will move in phase and with the same amplitude at the frequency of the first mode, as seen in Figure 5(a). For the second mode, each mass will move in opposite directions but with the same magnitude. The motion is out of phase. In Figure 5(b), which shows the free motion of the 2-DOF system, mass 1 oscillates at the same amplitude as mass 2 but in the opposite direction.

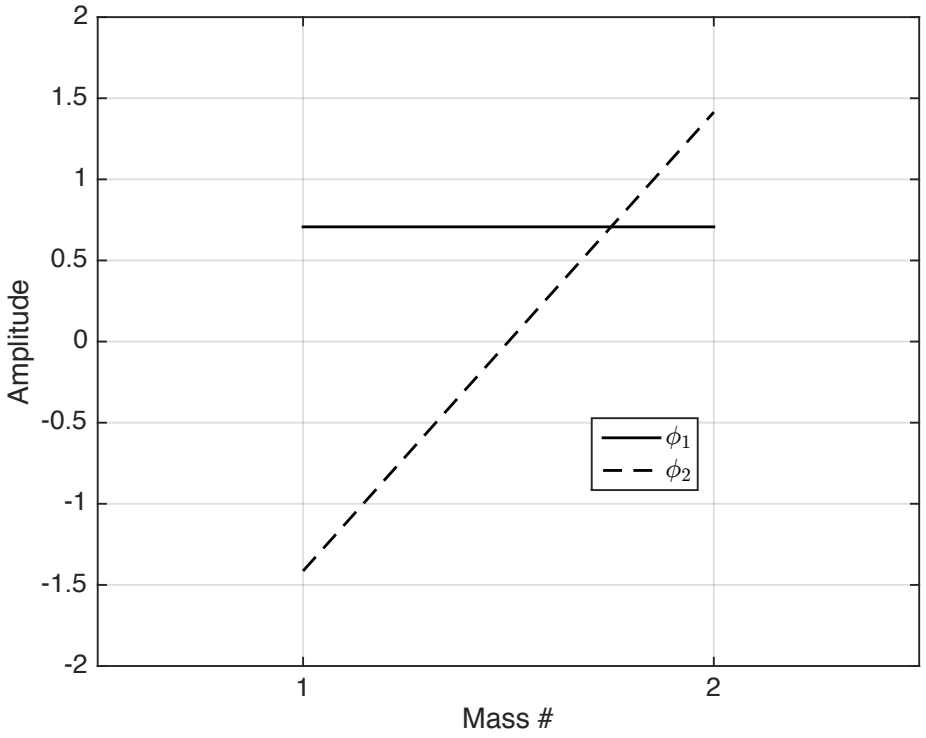

Figure 4. Mass-normalized mode shapes for a 2-DOF system.

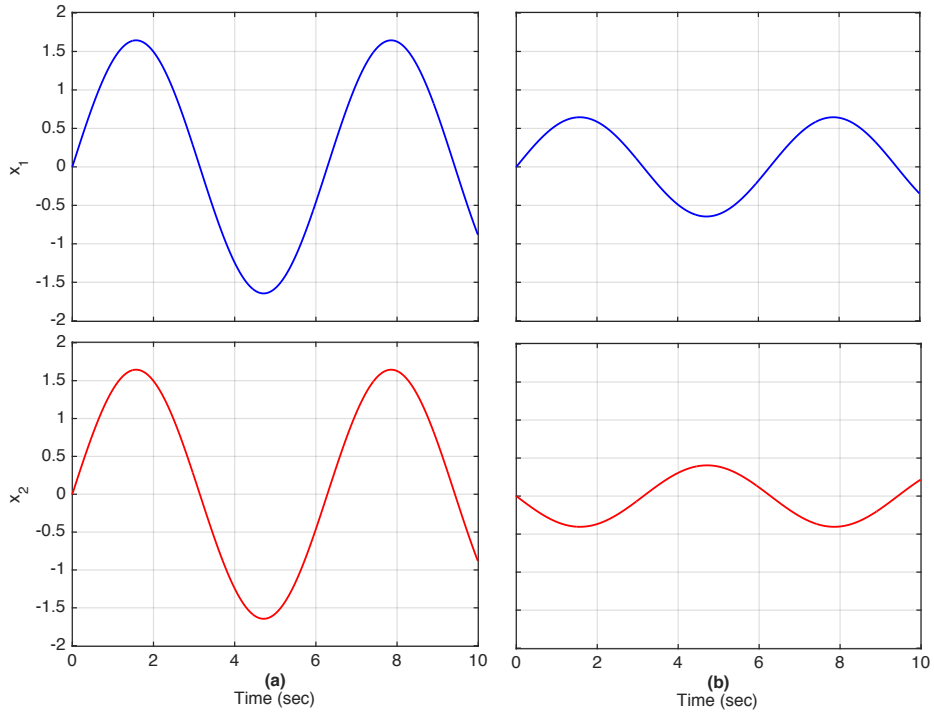

Figure 5. Normalized displacements: (a) mode 1; (b) mode 2.

C. UNDAMPED CASE WITH AN EXTERNAL FORCE

Adding a forcing function, $\mathbf{f}(t)$, to the 2-DOF system gives

$$\mathbf{M}\ddot{\mathbf{x}}(t)+\mathbf{K}\mathbf{x}(t)=\mathbf{f}(t). \tag{2.26}$$

The presence of the forcing function changes the procedure for modal analysis. In this case, the force vector can be written as $\mathbf{f}=\mathbf{F}e^{i\omega t}$ where $\mathbf{F}\in\mathbb{C}^{n\times 1}$ is a vector of complex amplitudes and ω is the frequency [7]. The variable ω does not represent an output frequency as in (2.5); rather, it denotes an input frequency for the forcing function. The eigensolution in (2.5) then becomes

$$(\mathbf{K}-\omega^2\mathbf{M})\mathbf{X}e^{i\omega t}=\mathbf{F}e^{i\omega t}\ . \tag{2.27}$$

Following the procedure in [7], let

$$\mathbf{X}=\mathbf{H}(\omega)\mathbf{F} \tag{2.28}$$

such that $\mathbf{H}\in\mathbb{R}^{nxn}$ and

$$\mathbf{H}(\omega)=(\mathbf{K}-\omega^2\mathbf{M})^{-1}. \tag{2.29}$$

In (2.29), matrix $\mathbf{H}$ is called a receptance frequency response function (FRF); it represents the system's displacement in response to an input given in the frequency domain [7]. Using the modal properties of the system, we may multiply by the matrix Φ and its transpose, as shown:

$$\Phi^T\mathbf{H}(\omega)^{-1}\Phi=\Phi^T(\mathbf{K}-\omega^2\mathbf{M})\Phi=\Phi^T\mathbf{K}\Phi-\Phi^T\omega^2\mathbf{M}\Phi\ . \tag{2.30}$$

Since Φ is mass-normalized, the quantity $\Phi^T\mathbf{K}\Phi$ gives a diagonal matrix of $\frac{\bar{k}_r}{\bar{m}_r}=\omega_r^2$ values. It also follows that $\Phi^T\omega^2\mathbf{M}\Phi=\omega^2\Phi^T\mathbf{M}\Phi=\mathrm{diag}(\omega^2)$. Therefore, (2.30) may be rewritten as

$$\Phi^T\mathbf{H}(\omega)^{-1}\Phi=\mathrm{diag}[(\omega_r^2-\omega^2)] \tag{2.31}$$

and further manipulated to give

$$\mathbf{H}(\omega)^{-1}=(\Phi^T)^{-1}\mathrm{diag}[(\omega_r^2-\omega^2)]\Phi^{-1}\ . \tag{2.32}$$

Recalling that $(\mathbf{AB})^{-1} = \mathbf{B}^{-1}\mathbf{A}^{-1}$, we obtain

$$\mathbf{H}(\omega) = \Phi(\text{diag}[(\omega_r^2 - \omega^2)])^{-1}\Phi^T \quad . \tag{2.33}$$

From (2.33), it is apparent that matrix $\mathbf{H}$ is symmetric. Because $\mathbf{H}$ represents the relationship between displacement and force, its components can be computed as

$$\mathbf{H}_{jk}(\omega) = \frac{\mathbf{X}_j}{\mathbf{F}_k} \tag{2.34}$$

where $j = 1 \ldots n$ and $k = 1 \ldots n$. In other words, $\mathbf{H}_{jk}$ is the FRF for the displacement of the j-th mass due to the k-th element of the force vector, superposed over all the modes. The same relationship will be explored later in the Laplace domain. This "element-wise" relationship is useful to study the response due to certain forces on specific masses in the system [7]. Equation (2.33) could also be used to find the full matrix of FRFs.

$$\mathbf{H}_{jk}(\omega) = \sum_{r=1}^{n} \frac{\Phi_{jr}\Phi_{kr}}{\omega_r^2 - \omega^2} = \sum_{r=1}^{n} \frac{\mathbf{V}_{jr}\mathbf{V}_{kr}}{\bar{m}_r\left(\omega_r^2 - \omega^2\right)} = \sum_{r=1}^{n} \frac{{}_r\mathbf{R}_{jk}}{\omega_r^2 - \omega^2} \, . \tag{2.35}$$

The modal constant ${}_r\mathbf{R}_{jk} \in \mathbb{C}^{1\text{x}1}$ is the specific receptance linking coordinates j and k for mode r [7]. The notion of the modal constant, or "residue," will also be seen later in the Laplace domain.

Equation (2.35) highlights the principle of superposition with respect to modes—the total response of a system is the sum of the responses of each mode. In other words,

$$\mathbf{H}(\omega) = \sum_{r=1}^{n} {}_r\mathbf{H}(\omega) \tag{2.36}$$

where ${}_r\mathbf{H}(\omega)$ denotes the FRF for mode r. In other words,

$$\mathbf{X}_j = \sum_{r=1}^{n}\sum_{k=1}^{n} {}_r\mathbf{H}_{jk}\mathbf{F}_k \quad . \tag{2.37}$$

For the 2-DOF system shown in Figure 3, the first mode dictates motion of both masses in the same direction and with the same amplitude. Thus, the receptance FRFs are the same.

$$ {}_1\mathbf{H}_{11}(\omega) = \frac{(m_1+m_2)^{-1/2}(m_1+m_2)^{-1/2}}{-\omega^2} = \frac{-1}{\omega^2(m_1+m_2)} \ . \tag{2.38} $$

Using (2.38) gives

$$ {}_1\mathbf{H}(\omega) = \begin{bmatrix} {}_1\mathbf{H}_{11} & {}_1\mathbf{H}_{12} \\ {}_1\mathbf{H}_{21} & {}_1\mathbf{H}_{22} \end{bmatrix} = \begin{bmatrix} \dfrac{-1}{\omega^2(m_1+m_2)} & \dfrac{-1}{\omega^2(m_1+m_2)} \\ \dfrac{-1}{\omega^2(m_1+m_2)} & \dfrac{-1}{\omega^2(m_1+m_2)} \end{bmatrix} . \tag{2.39} $$

For the second mode, the amplitude of motion is the same for each mass, but the directions oppose each other. The symbolic representation for the second mode is cumbersome, so ${}_2\mathbf{H}(\omega)$ is not provided here. A numerical example is given later to clarify the details.

D. VISCOUS DAMPING

So far, only the undamped case has been studied. More realistic is the presence of damping in some form. Two general cases are discussed in [7]: structural (or hysteretic) damping and viscous damping. While realistic to some degree, there are advantages and disadvantages for each case. In this thesis, only viscous damping is considered.

In the case of viscous damping, we first seek to determine the natural modes of the system by examining the unforced system, for which the general equation of motion is

$$ \mathbf{M}\ddot{\mathbf{x}}(t) + \mathbf{C}\dot{\mathbf{x}}(t) + \mathbf{K}\mathbf{x}(t) = \mathbf{0} . \tag{2.40} $$

The properties of each matrix are the same as previously defined for an n-DOF system. For the unforced case, with a solution of the form $\mathbf{x} = \mathbf{X}e^{\lambda t}$, where $\lambda = i\omega$, the equation of motion yields

$$(\mathbf{M}\bar{\lambda}^2 + \mathbf{C}\bar{\lambda} + \mathbf{K})\mathbf{X} = \mathbf{0} \ . \tag{2.41}$$

The solution to this equation is a complex eigenproblem, with complex-conjugate-pairs of eigenvalues $\bar{\lambda}$ and eigenvectors $\bar{\mathbf{v}}$ such that

$$(\mathbf{M}\bar{\lambda}^2 + \mathbf{C}\bar{\lambda} + \mathbf{K})\bar{\mathbf{v}} = \mathbf{0} \ . \tag{2.42}$$

The bar symbol over the eigenvalue and eigenvector variables is used to distinguish them from the ones computed for the undamped free case. Each eigenvalue, $\bar{\lambda}_r$, can be expressed as

$$\bar{\lambda}_r = \omega_r\left(-\zeta_r + i\sqrt{1-\zeta_r^2}\right) \tag{2.43}$$

so that the eigensolution of (2.42) can be described as

$$\begin{matrix} \bar{\lambda}_r, \bar{\lambda}_r^* \\ \text{and} \\ \bar{\mathbf{v}}_r, \bar{\mathbf{v}}_r^* \end{matrix} \ , \tag{2.44}$$

where $r = 1 \ldots n$. In (2.44), the * notation is used to denote the complex conjugate, (i.e., $\bar{\lambda}_r^* = \omega_r\left(-\zeta_r - i\sqrt{1-\zeta_r^2}\right)$). The orthogonality conditions are much more complicated than in the previous case. Let $\bar{\mathbf{v}}_q$ be the eigenvector for the q-th mode; the same notation applies for $\bar{\lambda}_q$. Ewins [7] derives the following orthogonality conditions:

$$\begin{matrix} (\bar{\lambda}_r + \bar{\lambda}_q)\bar{\mathbf{v}}_q^T\mathbf{M}\bar{\mathbf{v}}_r + \bar{\mathbf{v}}_q\mathbf{C}\bar{\mathbf{v}}_r = \mathbf{0} \\ \text{and} \\ \bar{\lambda}_r\bar{\lambda}_q\bar{\mathbf{v}}_q^T\mathbf{M}\bar{\mathbf{v}}_r + \bar{\mathbf{v}}_q\mathbf{K}\bar{\mathbf{v}}_r = \mathbf{0} \end{matrix} \ . \tag{2.45}$$

If, and only if, $\overline{\mathbf{v}}_q = \overline{\mathbf{v}}_r^*$ and $\overline{\lambda}_q = \omega_r\left(-\zeta_r - i\sqrt{1-\zeta_r^2}\right) = \overline{\lambda}_r^*$ then it is possible to determine the so-called natural frequencies ω_r and critical damping ratios ζ_r of the system.[1] In this case, (2.45) leads to

$$2\omega_r\zeta_r = \frac{\overline{\mathbf{v}}_r{}^H\mathbf{C}\overline{\mathbf{v}}_r}{\overline{\mathbf{v}}_r{}^H\mathbf{M}\overline{\mathbf{v}}_r} = \frac{\overline{c}_r}{\overline{m}_r}$$
$$\text{and} \tag{2.46}$$
$$\omega_r{}^2 = \frac{\overline{\mathbf{v}}_r{}^H\mathbf{K}\overline{\mathbf{v}}_r}{\overline{\mathbf{v}}_r{}^H\mathbf{M}\overline{\mathbf{v}}_r} = \frac{\overline{k}_r}{\overline{m}_r}$$

where the superscript H denotes the Hermitian (complex conjugate) transpose. The similarity to the conditions in (2.18) is evident.

The presence of damping makes the analysis of the forced system given in (2.47) more difficult to manipulate than for the undamped case.

$$\mathbf{M}\ddot{\mathbf{x}}(t) + \mathbf{C}\dot{\mathbf{x}}(t) + \mathbf{K}\mathbf{x}(t) = \mathbf{f}(t)\ . \tag{2.47}$$

To develop the FRF for the forced response, first recast (2.47) into state-space form [11]. This can be accomplished using the following procedure if, and only if, the roots of the characteristic equation of the system have multiplicity one. Define state variable $\mathbf{y} \in \mathbb{R}^{2n\text{x}1}$ as

$$\mathbf{y} = \begin{bmatrix} \mathbf{x} \\ \dot{\mathbf{x}} \end{bmatrix} \tag{2.48}$$

so that the unforced equation of motion can be recast as

$$\begin{bmatrix} \mathbf{C} & \mathbf{M} \end{bmatrix}\dot{\mathbf{y}} + \begin{bmatrix} \mathbf{K} & \mathbf{0} \end{bmatrix}\mathbf{y} = \mathbf{0}\ . \tag{2.49}$$

This produces a system of n equations with $2n$ unknowns, which is not helpful. Therefore, we make use of the identity equation

$$\begin{bmatrix} \mathbf{M} & \mathbf{0} \end{bmatrix}\dot{\mathbf{y}} + \begin{bmatrix} \mathbf{0} & -\mathbf{M} \end{bmatrix}\mathbf{y} = \mathbf{0} \tag{2.50}$$

[1] This "natural frequency" matches the "undamped natural frequency" for single-DOF systems or systems exhibiting proportional viscous damping only [7].

together with (2.49) to form a set of $2n$ equations to give

$$\begin{bmatrix} \mathbf{C} & \mathbf{M} \\ \mathbf{M} & \mathbf{0} \end{bmatrix}\dot{\mathbf{y}} + \begin{bmatrix} \mathbf{K} & \mathbf{0} \\ \mathbf{0} & -\mathbf{M} \end{bmatrix}\mathbf{y} = \mathbf{0} \ . \tag{2.51}$$

This equation simplifies to canonical state-space form

$$\mathbf{A}\dot{\mathbf{y}} + \mathbf{B}\mathbf{y} = \mathbf{0} \tag{2.52}$$

where $\mathbf{A} \in \mathbb{R}^{2n\text{x}2n}$ and $\mathbf{B} \in \mathbb{R}^{2n\text{x}2n}$ are each square matrices. The eigensolution, assuming a solution to (2.52) of the form $\mathbf{y} = \mathbf{Y}e^{\bar{\lambda}t}$, produces $2n$ complex-conjugate-pair eigenvalues and $2n$ complex-conjugate-pair eigenvectors $\varphi_r \in \mathbb{C}^{2n\text{x}1}$**.** The eigenvalues and eigenvectors satisfy the general eigensolution

$$(\bar{\lambda}_r\mathbf{A} + \mathbf{B})\varphi_r = \mathbf{0} \tag{2.53}$$

where $r = 1\ldots 2n$. Orthogonality is useful here as well. Let $\vartheta \in \mathbb{C}^{2n\text{x}2n}$ be a matrix whose columns are the eigenvectors, φ_r, of the uncoupled system. Then, we may write

$$\begin{aligned} \left[a_r\right] &= \vartheta^T\mathbf{A}\vartheta \\ \left[b_r\right] &= \vartheta^T\mathbf{B}\vartheta \end{aligned} \tag{2.54}$$

such that

$$\bar{\lambda}_r = -\frac{b_r}{a_r} \tag{2.55}$$

where a_r and b_r are the r-th elements of diagonal matrices $\left[a_r\right] \in \mathbb{C}^{2n\text{x}2n}$ and $\left[b_r\right] \in \mathbb{C}^{2n\text{x}2n}$, respectively. It is important to note that the transpose operation in (2.54) is the non-conjugate transpose of the eigenvector matrix (versus the Hermitian transpose used in (2.46)) [7].

The forcing function $\mathbf{F}$ can now be expressed as

$$\mathbf{P} = \begin{bmatrix} \mathbf{F} \\ \mathbf{0} \end{bmatrix} \tag{2.56}$$

where $\mathbf{P} \in \mathbb{C}^{2n\text{x}1}$. To find the FRF, recall the procedure used in (2.28)–(2.35). The FRF can then be written as

$$\begin{bmatrix} X \\ \vdots \\ i\omega X \end{bmatrix} = \sum_{r=1}^{2n} \frac{\varphi_r^T \mathbf{P} \varphi_r}{a_r (i\omega - \bar{\lambda}_r)} \tag{2.57}$$

which leads to the following individual receptance FRFs for the forced system (with viscous damping):

$$\mathbf{H}_{jk}(\omega) = \sum_{r=1}^{n} \left(\frac{\vartheta_{jr}\vartheta_{kr}}{a_r\left(\omega_r\zeta_r + i\left(\omega - \omega_r\sqrt{1-\zeta_r^2}\right)\right)} + \frac{\vartheta_{jr}^*\vartheta_{kr}^*}{a_r^*\left(\omega_r\zeta_r + i\left(\omega + \omega_r\sqrt{1-\zeta_r^2}\right)\right)} \right) . \tag{2.58}$$

The relationship in (2.55) points to a useful coordinate transformation provided by the eigenvector matrix ϑ. Let $\mathbf{y} = \vartheta\mathbf{q}$ where $\mathbf{q} \in \mathbb{C}^{2n\text{x}1}$ is the so-called modal coordinate. From (2.53), one can see that $\mathbf{q} = e^{\bar{\lambda}t}$. As a result, (2.52) becomes

$$\mathbf{A}\vartheta\dot{\mathbf{q}} + \mathbf{B}\vartheta\mathbf{q} = \mathbf{P} \tag{2.59}$$

The transformation by ϑ puts the equations of motion in terms of modal coordinates to simplify further analysis. Premultiplying by ϑ^T yields

$$\vartheta^T\mathbf{A}\vartheta\dot{\mathbf{q}} + \vartheta^T\mathbf{B}\vartheta\mathbf{q} = \vartheta^T\mathbf{P} \ . \tag{2.60}$$

So, for the r-th mode, (2.54) can be used to get

$$\begin{gathered} \vartheta_r^T\mathbf{A}\vartheta_r\dot{\mathbf{q}}_r + \vartheta_r^T\mathbf{B}\vartheta_r\mathbf{q}_r = \vartheta_r^T\mathbf{P} = \mathbf{P}_r' \\ a_r\dot{\mathbf{q}} + b_r\mathbf{q}_r = \mathbf{P}_r' \end{gathered} \ . \tag{2.61}$$

Here, the r-th mode corresponds to the r-th element in the vector $\mathbf{q}$ [11]. This transformation will be discussed further below.

E. PROPORTIONAL VISCOUS DAMPING

A special case of viscous damping is called proportional (or classical) damping [12]. Proportional damping offers advantages in analysis over the more general case in that the mode shapes of a proportionally damped system are the same as those for the undamped system, and the natural frequencies are similar [7]. The general equation of motion is the same as in (2.40), but now the damping matrix is proportional to the mass and stiffness matrices such that

$$\mathbf{C} = \beta\mathbf{K} + \gamma\mathbf{M} \tag{2.62}$$

where β and γ are scalar constants. As a result, $\mathbf{C}$ is diagonalizable by the eigenvector matrix $\mathbf{V}$ to produce

$$\overline{\mathbf{C}} = \mathbf{V}^T\mathbf{C}\mathbf{V} \tag{2.63}$$

where the r-th diagonal element of $\overline{\mathbf{C}} \in \mathbb{R}^{nxn}$ is the modal damping constant, $\overline{c}_r$, for the r-th mode.

For the 2-DOF system in Figure 3, the modal damping matrix is

$$\begin{aligned}\overline{\mathbf{C}} = \mathbf{V}^T\mathbf{C}\mathbf{V} &= \begin{bmatrix} 1 & 1 \\ -\frac{m_2}{m_1} & 1 \end{bmatrix}\begin{bmatrix} c & -c \\ -c & c \end{bmatrix}\begin{bmatrix} 1 & -\frac{m_2}{m_1} \\ 1 & 1 \end{bmatrix} \\ &= \begin{bmatrix} 0 & 0 \\ -c\frac{(m_1+m_2)}{m_1} & c\frac{(m_1+m_2)}{m_1} \end{bmatrix}\begin{bmatrix} 1 & -\frac{m_2}{m_1} \\ 1 & 1 \end{bmatrix} \\ &= \begin{bmatrix} 0 & 0 \\ 0 & c\frac{(m_1+m_2)^2}{m_1^{\,2}} \end{bmatrix}\end{aligned} \tag{2.64}$$

because $\beta = \frac{k}{c}$ exists and $\gamma = 0$.

The modal transformation of a proportionally damped system is also more straightforward. The unforced system, from (2.18) and (2.63), is

$$\overline{\mathbf{M}}\ddot{\mathbf{q}} + \overline{\mathbf{C}}\dot{\mathbf{q}} + \overline{\mathbf{K}}\mathbf{q} = \mathbf{0} \tag{2.65}$$

where $\mathbf{q} = \mathbf{V}^{-1}\mathbf{x}$. Thus, the forced case is written in modal coordinates as

$$\overline{\mathbf{M}}\ddot{\mathbf{q}} + \overline{\mathbf{C}}\dot{\mathbf{q}} + \overline{\mathbf{K}}\mathbf{q} = \mathbf{V}^T\mathbf{f}(t) = \mathbf{f}'(t) \ . \tag{2.66}$$

For the r-th mode,

$$\overline{m}_r\ddot{\mathbf{q}}_r + \overline{c}_r\dot{\mathbf{q}}_r + \overline{k}_r\mathbf{q}_r = \mathbf{f}_r'(t) \tag{2.67}$$

Equation (2.67) is clearly the equation of motion for a set of single-DOF mass-spring-damper systems, which represents the modes of a multiple-DOF system. Assuming a solution to the equation of the form $\mathbf{q} = \mathbf{Q}e^{\lambda t}$, where λ is complex due to the presence of the damping terms, the r-th complex conjugate eigenvalue is computed from the characteristic polynomial

$$\begin{gathered} \overline{m}_r\lambda_r^2 + \overline{c}_r\lambda_r + \overline{k}_r = 0 \\ \lambda_r = \frac{-\overline{c}_r \pm \sqrt{\overline{c}_r^2 - 4\overline{m}_r\overline{k}_r}}{2\overline{m}_r} = -\omega_r\zeta_r \pm i\omega_r\sqrt{1-\zeta_r^2} \end{gathered} \tag{2.68}$$

where, because of the proportional relationship in (2.62),

$$\begin{gathered} \omega_r = \sqrt{\frac{\overline{k}_r}{\overline{m}_r}} \\ \text{and} \qquad . \\ \zeta_r = \frac{\overline{c}_r}{2\sqrt{\overline{m}_r\overline{k}_r}} = \frac{\beta\omega_r}{2} + \frac{\gamma}{2\omega_r} \end{gathered} \tag{2.69}$$

The damped natural frequency ω_r' is written as

$$\omega_r' = \omega_r\sqrt{1-\zeta_r^2} \tag{2.70}$$

We note that as long as ζ_r is small, $\omega_r' \approx \omega_r$.

For the 2-DOF system shown in Figure 3, by inspection, $\omega_1 = \omega_1' = \zeta_1 = \lambda_1 = 0$, and for the second mode,

$$\omega_2 = \sqrt{\frac{\bar{k}_2}{\bar{m}_2}} = \sqrt{\frac{\dfrac{k(m_1+m_2)^2}{m_1^2}}{\dfrac{m_2^2}{m_1}+m_2}} = \sqrt{\frac{k(m_1+m_2)}{m_1 m_2}} \tag{2.71}$$

$$\zeta_2 = \frac{\bar{c}_2}{2\sqrt{\bar{m}_2\bar{k}_2}} = \frac{\dfrac{c(m_1+m_2)^2}{m_1^2}}{2\sqrt{\left(\dfrac{m_2^2}{m_1}+m_2\right)\left(\dfrac{k(m_1+m_2)^2}{m_1^2}\right)}} = \frac{c(m_1+m_2)}{2m_1\sqrt{k\left(\dfrac{m_2^2}{m_1}+m_2\right)}} \ . \tag{2.72}$$

For analysis of the forced response, it is possible to make use of (2.29) to get

$$\mathbf{H}(\omega) = \left(\mathbf{K} + i\omega\mathbf{C} - \omega^2\mathbf{M}\right)^{-1} \tag{2.73}$$

$$\mathbf{V}^T\mathbf{H}(\omega)\mathbf{V} = \mathbf{V}^T\left(\mathbf{K} + i\omega\mathbf{C} - \omega^2\mathbf{M}\right)^{-1}\mathbf{V} \ . \tag{2.74}$$

Thus, the individual FRFs are represented by

$$\mathbf{H}_{jk}(\omega) = \sum_{r=1}^{n} \frac{\mathbf{V}_{jr}\mathbf{V}_{kr}}{\bar{k}_r + i\omega\bar{c}_r - \omega^2\bar{m}_r} \ , \tag{2.75}$$

where each term in the sum is the FRF corresponding to the r-th mode.

For the 2-DOF system shown in Figure 3, the same symmetry exists in $\mathbf{H}$ when assuming proportional damping. For the first mode, $r=1$, the FRFs are the same as for the undamped system (this may not always be the case) in (2.39). For $r=2$,

$$\begin{aligned} {}_2\mathbf{H}_{11}(\omega) &= \frac{\mathbf{V}_{12}\mathbf{V}_{12}}{\bar{k}_2 - i\omega\bar{c}_2 - \omega^2\bar{m}_2} \\ &= \frac{\left(\dfrac{m_2}{m_1}\right)^2}{\dfrac{k\left(m_1+m_2\right)^2}{m_1^2} + i\omega\dfrac{c\left(m_1+m_2\right)^2}{m_1^2} - \omega^2\left(\dfrac{m_2^2}{m_1}+m_2\right)} \\ &= \frac{m_2^2}{k\left(m_1+m_2\right)^2 + i\omega c\left(m_1+m_2\right)^2 - \omega^2\left(m_1m_2^2 + m_1^2m_2\right)} \end{aligned} \ , \tag{2.76}$$

and so on. Numerical examples are discussed below that further illustrate the features of the modal analysis.

F. NUMERICAL EXAMPLE

Assume a nominal case where $m_1 = m_2 = c = k = 1$. For the undamped case with free vibration,

$$[\lambda_r] = \begin{bmatrix} 0 & 0 \\ 0 & \dfrac{(m_1+m_2)k}{m_1 m_2} \end{bmatrix} = \begin{bmatrix} 0 & 0 \\ 0 & 2 \end{bmatrix} \quad . \qquad (2.77)$$

$$\mathbf{V} = \begin{bmatrix} 1 & -\dfrac{m_2}{m_1} \\ 1 & 1 \end{bmatrix} = \begin{bmatrix} 1 & -1 \\ 1 & 1 \end{bmatrix}$$

It follows that $\omega_1 = 0$ and $\omega_2 = \sqrt{2}$. Column vector $\mathbf{v}_2$ indicates that the amplitudes of motion of both masses in mode 2 will be equal but in opposite directions. Thus, the modal matrices and mass-normalized mode shape vectors are

$$\overline{\mathbf{M}} = \begin{bmatrix} m_1+m_2 & 0 \\ 0 & \dfrac{m_2{}^2}{m_1}+m_2 \end{bmatrix} = \begin{bmatrix} 2 & 0 \\ 0 & 2 \end{bmatrix}$$

$$\overline{\mathbf{K}} = \begin{bmatrix} 0 & 0 \\ 0 & \dfrac{k(m_1+m_2)^2}{m_1{}^2} \end{bmatrix} = \begin{bmatrix} 0 & 0 \\ 0 & 4 \end{bmatrix} \qquad (2.78)$$

with

$$\boldsymbol{\Phi} = \begin{bmatrix} (m_1+m_2)^{-1/2} & -\dfrac{m_2}{m_1}\left(\dfrac{m_1}{(m_1+m_2)m_2}\right)^{1/2} \\ (m_1+m_2)^{-1/2} & \left(\dfrac{m_1}{(m_1+m_2)m_2}\right)^{1/2} \end{bmatrix} = \begin{bmatrix} \dfrac{\sqrt{2}}{2} & -\dfrac{\sqrt{2}}{2} \\ \dfrac{\sqrt{2}}{2} & \dfrac{\sqrt{2}}{2} \end{bmatrix}. \qquad (2.79)$$

Note that with different scaling of the eigenvectors in $\mathbf{V}$, the modal matrices will contain different values, but the relationship $\lambda_r = \omega_r^2 = \dfrac{\bar{k}_r}{\bar{m}_r}$ will be preserved.

To analyze the frequency response in an undamped system with an external force, use (2.33) to get

$$\begin{aligned} \mathbf{H}(\omega) &= \begin{bmatrix} \dfrac{\sqrt{2}}{2} & -\dfrac{\sqrt{2}}{2} \\ \dfrac{\sqrt{2}}{2} & \dfrac{\sqrt{2}}{2} \end{bmatrix} \begin{bmatrix} -\omega^2 & 0 \\ 0 & 2-\omega^2 \end{bmatrix}^{-1} \begin{bmatrix} \dfrac{\sqrt{2}}{2} & \dfrac{\sqrt{2}}{2} \\ -\dfrac{\sqrt{2}}{2} & \dfrac{\sqrt{2}}{2} \end{bmatrix} \\ &= \begin{bmatrix} -\dfrac{1}{2\omega^2} - \dfrac{1}{2(\omega^2-2)} & \dfrac{1}{\omega^2(\omega^2-2)} \\ \dfrac{1}{\omega^2(\omega^2-2)} & -\dfrac{1}{2\omega^2} - \dfrac{1}{2(\omega^2-2)} \end{bmatrix} \end{aligned}. \qquad (2.80)$$

Alternatively, each element of $\mathbf{H}$ can be computed individually using (2.35). For example,

$$\mathbf{H}_{12}(\omega) = \frac{\left(\dfrac{\sqrt{2}}{2}\right)\left(\dfrac{\sqrt{2}}{2}\right)}{-\omega^2} + \frac{\left(-\dfrac{\sqrt{2}}{2}\right)\left(\dfrac{\sqrt{2}}{2}\right)}{2-\omega^2} = \frac{1}{\omega^2(\omega^2-2)}. \qquad (2.81)$$

A plot of the impulse response for the FRF in (2.81) is shown in Figure 6(a) as an oscillating linear growth toward infinity. Response to other inputs would show growth to infinity as well. This is not helpful in studying the oscillatory effects only, because the rigid-body motion of the system and the

oscillations are superposed, (i.e., the time history of Figure 6(a) is the sum of the rigid motion in Figure 6(b) and the oscillatory motion in Figure 6(c)).

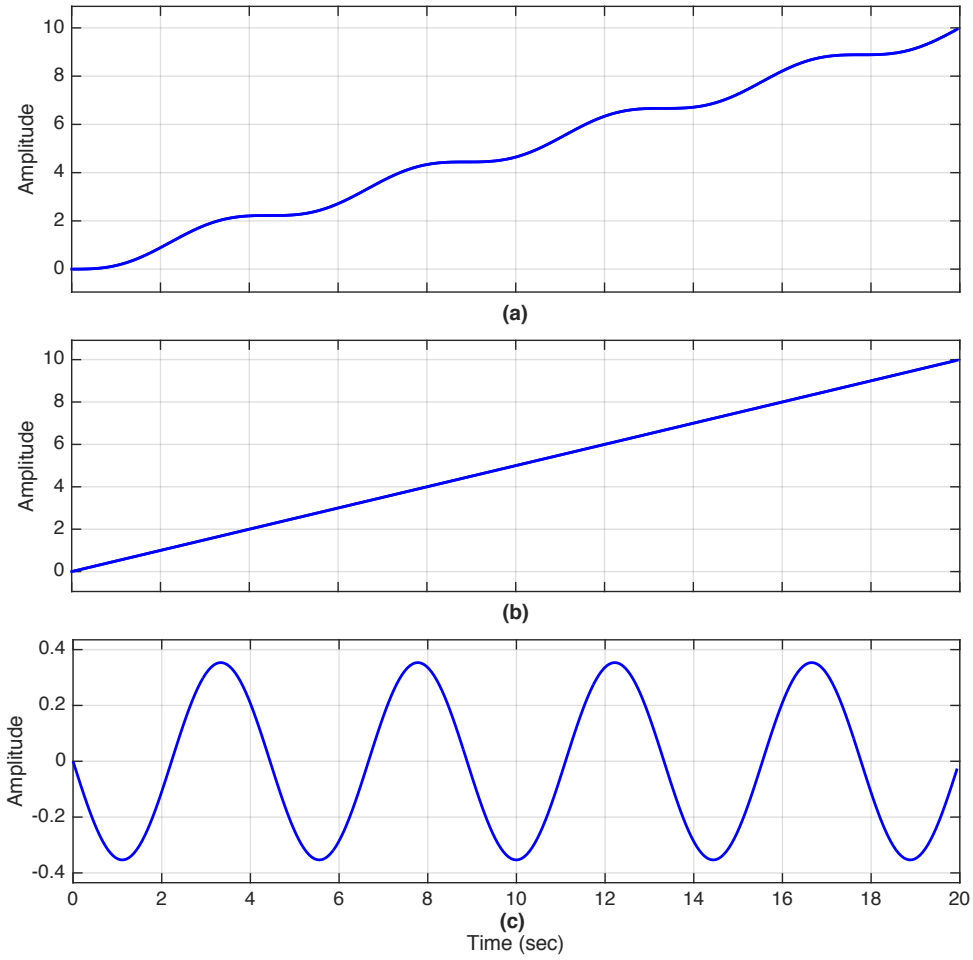

Figure 6. Undamped impulse responses in time domain: (a) $\mathbf{H}_{12} = {}_1\mathbf{H}_{12} + {}_2\mathbf{H}_{12}$; (b) ${}_1\mathbf{H}_{12}$; (c) ${}_2\mathbf{H}_{12}$.

For reference, the FRF for the first mode (from (2.81)) is

$$ {}_1\mathbf{H}_{12}(\omega) = -\frac{\frac{1}{2}}{\omega^2} \tag{2.82}$$

and the FRF for the second mode is

$$ {}_2\mathbf{H}_{12}(\omega) = -\frac{\frac{1}{2}}{2-\omega^2} \ . \tag{2.83} $$

Since the damping matrix of the system shown in Figure 3 is proportional to the stiffness and mass matrices ($\beta = 1$, $\gamma = 0$), this system exhibits proportional damping and is straightforward to analyze. However, for completeness, the general complex modal case is computed to illustrate the steps. First, the unforced case is analyzed to compute the natural frequencies and damping ratios. First, we find the eigenvalues in (2.42).

$$ \begin{gathered} \det\left(\bar{\lambda}^2\mathbf{M} + \bar{\lambda}\mathbf{C} + \mathbf{K}\right) = \mathbf{0} \\ \det\left(\begin{bmatrix} \bar{\lambda}^2 & 0 \\ 0 & \bar{\lambda}^2 \end{bmatrix} + \begin{bmatrix} \bar{\lambda} & -\bar{\lambda} \\ -\bar{\lambda} & \bar{\lambda} \end{bmatrix} + \begin{bmatrix} 1 & -1 \\ -1 & 1 \end{bmatrix}\right) \\ = \det\begin{bmatrix} \bar{\lambda}^2 + \bar{\lambda} + 1 & -\bar{\lambda} - 1 \\ -\bar{\lambda} - 1 & \bar{\lambda}^2 + \bar{\lambda} + 1 \end{bmatrix} \\ = \bar{\lambda}_r{}^4 + 2\bar{\lambda}_r{}^3 + 2\bar{\lambda}_r{}^2 = 0 \\ \bar{\lambda}_r{}^4 + 2\bar{\lambda}_r{}^3 + 2\bar{\lambda}_r{}^2 = \bar{\lambda}_r{}^2\left(\bar{\lambda}_r{}^2 + 2\bar{\lambda}_r + 2\right) = 0 \end{gathered} \tag{2.84} $$

Therefore, $\bar{\lambda}_1 = \bar{\lambda}_1^* = 0$. The quadratic formula yields $\bar{\lambda}_2 = -1 \pm i$ from the second term. Following the same process in (2.11), for $\bar{\lambda}_1 = \bar{\lambda}_1^* = 0$, we obtain the first eigenvector:

$$ \begin{gathered} \left[\begin{array}{cc|c} \bar{\lambda}_1^2 + \bar{\lambda}_1 + 1 & -\bar{\lambda}_1 - 1 & 0 \\ -\bar{\lambda}_1 - 1 & \bar{\lambda}_1^2 + \bar{\lambda}_1 + 1 & 0 \end{array}\right] = \left[\begin{array}{cc|c} 1 & -1 & 0 \\ -1 & 1 & 0 \end{array}\right] = \left[\begin{array}{cc|c} 1 & -1 & 0 \\ 0 & 0 & 0 \end{array}\right] \\ \bar{\mathbf{v}}_1 = \begin{bmatrix} 1 \\ 1 \end{bmatrix} \pm i \begin{bmatrix} 0 \\ 0 \end{bmatrix} \end{gathered} \tag{2.85} $$

For $\bar{\lambda}_2 = -1 + i$,

$$\left[\begin{array}{cc|c} (-1+i)^2+(-1+i)+1 & -(-1+i)-1 & 0 \\ -(-1+i)-1 & (-1+i)^2+(-1+i)+1 & 0 \end{array}\right]$$

$$=\left[\begin{array}{cc|c} -i & -i & 0 \\ -i & -i & 0 \end{array}\right]=\left[\begin{array}{cc|c} 1 & 1 & 0 \\ 0 & 0 & 0 \end{array}\right] \quad . \tag{2.86}$$

$$\bar{\mathbf{v}}_2=\left[\begin{array}{c} 1 \\ -1 \end{array}\right]\pm i\left[\begin{array}{c} 0 \\ 0 \end{array}\right]$$

Recall that the eigenvectors occur in complex conjugate pairs, hence the $\pm$ sign.

Use these eigenvectors and (2.46) to find the natural frequencies and critical damping ratios for each mode. For mode 1,

$$\begin{aligned} 2\omega_1\zeta_1=\frac{\bar{c}_1}{\bar{m}_1}=\frac{\bar{\mathbf{v}}_1{}^H\mathbf{C}\bar{\mathbf{v}}_1}{\bar{\mathbf{v}}_1{}^H\mathbf{M}\bar{\mathbf{v}}_1}&=\frac{\left[\begin{array}{cc} 1 & 1 \end{array}\right]\left[\begin{array}{cc} 1 & -1 \\ -1 & 1 \end{array}\right]\left[\begin{array}{c} 1 \\ 1 \end{array}\right]}{\left[\begin{array}{cc} 1 & 1 \end{array}\right]\left[\begin{array}{cc} 1 & 0 \\ 0 & 1 \end{array}\right]\left[\begin{array}{c} 1 \\ 1 \end{array}\right]}=0 \\ \omega_1{}^2=\frac{\bar{k}_1}{\bar{m}_1}=\frac{\bar{\mathbf{v}}_1{}^H\mathbf{K}\bar{\mathbf{v}}_1}{\bar{\mathbf{v}}_1{}^H\mathbf{M}\bar{\mathbf{v}}_1}&=\frac{\left[\begin{array}{cc} 1 & 1 \end{array}\right]\left[\begin{array}{cc} 1 & -1 \\ -1 & 1 \end{array}\right]\left[\begin{array}{c} 1 \\ 1 \end{array}\right]}{\left[\begin{array}{cc} 1 & 1 \end{array}\right]\left[\begin{array}{cc} 1 & 0 \\ 0 & 1 \end{array}\right]\left[\begin{array}{c} 1 \\ 1 \end{array}\right]}=0 \end{aligned} \quad , \tag{2.87}$$

which follows since $\bar{\lambda}_1=\bar{\lambda}_1^*=0$. For mode 2,

$$\begin{aligned} 2\omega_2\zeta_2=\frac{\bar{c}_2}{\bar{m}_2}=\frac{\bar{\mathbf{v}}_2{}^H\mathbf{C}\bar{\mathbf{v}}_2}{\bar{\mathbf{v}}_2{}^H\mathbf{M}\bar{\mathbf{v}}_2}&=\frac{\left[\begin{array}{cc} 1 & -1 \end{array}\right]\left[\begin{array}{cc} 1 & -1 \\ -1 & 1 \end{array}\right]\left[\begin{array}{c} 1 \\ -1 \end{array}\right]}{\left[\begin{array}{cc} 1 & -1 \end{array}\right]\left[\begin{array}{cc} 1 & 0 \\ 0 & 1 \end{array}\right]\left[\begin{array}{c} 1 \\ -1 \end{array}\right]}=\frac{4}{2}=2 \\ \omega_2{}^2=\frac{\bar{k}_2}{\bar{m}_2}=\frac{\bar{\mathbf{v}}_2{}^H\mathbf{K}\bar{\mathbf{v}}_2}{\bar{\mathbf{v}}_2{}^H\mathbf{M}\bar{\mathbf{v}}_2}&=\frac{\left[\begin{array}{cc} 1 & -1 \end{array}\right]\left[\begin{array}{cc} 1 & -1 \\ -1 & 1 \end{array}\right]\left[\begin{array}{c} 1 \\ -1 \end{array}\right]}{\left[\begin{array}{cc} 1 & -1 \end{array}\right]\left[\begin{array}{cc} 1 & 0 \\ 0 & 1 \end{array}\right]\left[\begin{array}{c} 1 \\ -1 \end{array}\right]}=2 \end{aligned} \quad . \tag{2.88}$$

Therefore, $\omega_2=\sqrt{2}$ and $\zeta_2=\sqrt{2}/2$. As a check, we may verify that these values reproduce the eigenvalues given by (2.84):

$$\bar{\lambda}_2 = \omega_2\left(-\zeta_2 + i\sqrt{1-\zeta_2^2}\right) = \sqrt{2}\left(-\frac{\sqrt{2}}{2} + i\sqrt{1-\left(\frac{\sqrt{2}}{2}\right)^2}\right) = -1+i \quad . \qquad (2.89)$$

$$\bar{\lambda}_2^* = -1-i$$

Now we wish to derive the uncoupled modal motion of the system. The state-space form of this system (from (2.51)) is

$$\begin{bmatrix} 1 & -1 & 1 & 0 \\ -1 & 1 & 0 & 1 \\ 1 & 0 & 0 & 0 \\ 0 & 1 & 0 & 0 \end{bmatrix}\dot{\mathbf{y}} + \begin{bmatrix} 1 & -1 & 0 & 0 \\ -1 & 1 & 0 & 0 \\ 0 & 0 & -1 & 0 \\ 0 & 0 & 0 & -1 \end{bmatrix}\mathbf{y} = \mathbf{0} \quad . \qquad (2.90)$$

Using the eigensolution form given in (2.53), the eigenvalues may be computed. The same eigenvalues as computed above should be obtained. The results are

$$\begin{aligned} \det\left[\bar{\lambda}_r\mathbf{A} + \mathbf{B}\right] &= \mathbf{0} \\ &= \det\left(\begin{bmatrix} \bar{\lambda}_r & -\bar{\lambda}_r & \bar{\lambda}_r & 0 \\ -\bar{\lambda}_r & \bar{\lambda}_r & 0 & \bar{\lambda}_r \\ \bar{\lambda}_r & 0 & 0 & 0 \\ 0 & \bar{\lambda}_r & 0 & 0 \end{bmatrix} + \begin{bmatrix} 1 & -1 & 0 & 0 \\ -1 & 1 & 0 & 0 \\ 0 & 0 & -1 & 0 \\ 0 & 0 & 0 & -1 \end{bmatrix}\right) \\ &= \det\begin{bmatrix} \bar{\lambda}_r + 1 & -\bar{\lambda}_r - 1 & \bar{\lambda}_r & 0 \\ -\bar{\lambda}_r - 1 & \bar{\lambda}_r + 1 & 0 & \bar{\lambda}_r \\ \bar{\lambda}_r & 0 & -1 & 0 \\ 0 & \bar{\lambda}_r & 0 & -1 \end{bmatrix} \\ &= \bar{\lambda}_r^{\,4} + 2\bar{\lambda}_r^{\,3} + 2\bar{\lambda}_r^{\,2} \\ &= \bar{\lambda}_r^{\,2}\left(\bar{\lambda}_r^{\,2} + 2\bar{\lambda}_r + 2\right) = 0 \end{aligned} \quad . \qquad (2.91)$$

Again, $\bar{\lambda}_1 = 0$ and $\bar{\lambda}_2 = -1 \pm i$. The eigenvectors, however, will be different because the system is now in the uncoupled state-space form. For $\bar{\lambda}_1 = 0$,

$$\left[\begin{array}{cccc|c} \bar{\lambda}_1+1 & -\bar{\lambda}_1-1 & \bar{\lambda}_1 & 0 & 0 \\ -\bar{\lambda}_1-1 & \bar{\lambda}_1+1 & 0 & \bar{\lambda}_1 & 0 \\ \bar{\lambda}_1 & 0 & -1 & 0 & 0 \\ 0 & \bar{\lambda}_1 & 0 & -1 & 0 \end{array}\right] = \left[\begin{array}{cccc|c} 1 & -1 & 0 & 0 & 0 \\ -1 & 1 & 0 & 0 & 0 \\ 0 & 0 & -1 & 0 & 0 \\ 0 & 0 & 0 & -1 & 0 \end{array}\right]$$

$$= \left[\begin{array}{cccc|c} 1 & -1 & 0 & 0 & 0 \\ 0 & 0 & 1 & 0 & 0 \\ 0 & 0 & 0 & 1 & 0 \\ 0 & 0 & 0 & 0 & 0 \end{array}\right] \quad . \qquad (2.92)$$

$$\varphi_1 = \begin{bmatrix} 1 \\ 1 \\ 0 \\ 0 \end{bmatrix} \pm i \begin{bmatrix} 0 \\ 0 \\ 0 \\ 0 \end{bmatrix}$$

For $\bar{\lambda}_2 = -1 \pm i$,

$$\left[\begin{array}{cccc|c} -1\pm i+1 & -(-1\pm i)-1 & -1\pm i & 0 & 0 \\ -(-1\pm i)-1 & -1\pm i+1 & 0 & -1\pm i & 0 \\ -1\pm i & 0 & -1 & 0 & 0 \\ 0 & -1\pm i & 0 & -1 & 0 \end{array}\right]$$

$$=\left[\begin{array}{cccc|c} \pm i & \mp i & -1\pm i & 0 & 0 \\ \mp i & \pm i & 0 & -1\pm i & 0 \\ -1\pm i & 0 & -1 & 0 & 0 \\ 0 & -1\pm i & 0 & -1 & 0 \end{array}\right]$$

$$=\left[\begin{array}{cccc|c} 1 & 0 & 0 & -\frac{1}{2}\mp\frac{1}{2}i & 0 \\ 0 & 1 & 0 & \frac{1}{2}\pm\frac{1}{2}i & 0 \\ 0 & 0 & 1 & 1 & 0 \\ 0 & 0 & 0 & 0 & \end{array}\right] \qquad . \qquad (2.93)$$

$$\varphi_2=\begin{bmatrix} 1/2 \\ -1/2 \\ -1 \\ 1 \end{bmatrix}\pm i\begin{bmatrix} 1/2 \\ -1/2 \\ 0 \\ 0 \end{bmatrix}$$

Recall that the eigenvectors occur in complex-conjugate pairs, which is the case obtained in (2.93). The full matrix ϑ is of the form $\left[\begin{array}{c|c|c|c} \varphi_1 & \varphi_2 & \varphi_1^* & \varphi_2^* \end{array}\right]$ and produces matrix $[a_r]\in\mathbb{C}^{2n\times 2n}$ of the form $\operatorname{diag}\left[\begin{array}{cccc} a_1 & a_2 & a_1^* & a_2^* \end{array}\right]$ and $[b_r]=\operatorname{diag}\left[\begin{array}{cccc} b_1 & b_2 & b_1^* & b_2^* \end{array}\right]$. From (2.54),

$$\left[a_r\right] = \vartheta^T \mathbf{A} \vartheta = \begin{bmatrix} 1 & 1 & 0 & 0 \\ \frac{1}{2} \pm \frac{1}{2}i & -\frac{1}{2} \mp \frac{1}{2}i & -1 & 1 \end{bmatrix} \begin{bmatrix} 1 & -1 & 1 & 0 \\ -1 & 1 & 0 & 1 \\ 1 & 0 & 0 & 0 \\ 0 & 1 & 0 & 0 \end{bmatrix} \begin{bmatrix} 1 & \frac{1}{2} \pm \frac{1}{2}i \\ 1 & -\frac{1}{2} \mp \frac{1}{2}i \\ 0 & -1 \\ 0 & 1 \end{bmatrix} \quad (2.94)$$

$$= \begin{bmatrix} 0 & 0 \\ 0 & -2 \end{bmatrix}$$

$$\left[b_r\right] = \vartheta^T \mathbf{B} \vartheta = \begin{bmatrix} 1 & 1 & 0 & 0 \\ \frac{1}{2} \pm \frac{1}{2}i & -\frac{1}{2} \mp \frac{1}{2}i & -1 & 1 \end{bmatrix} \begin{bmatrix} 1 & -1 & 0 & 0 \\ -1 & 1 & 0 & 0 \\ 0 & 0 & -1 & 0 \\ 0 & 0 & 0 & -1 \end{bmatrix} \begin{bmatrix} 1 & \frac{1}{2} \pm \frac{1}{2}i \\ 1 & -\frac{1}{2} \mp \frac{1}{2}i \\ 0 & -1 \\ 0 & 1 \end{bmatrix}. \quad (2.95)$$

$$= \begin{bmatrix} 0 & 0 \\ 0 & -2 \pm 2i \end{bmatrix}$$

By inspection, it is evident that $\overline{\lambda}_2 = -b_2 / a_2 = -1 \pm i$, satisfying the relationship defined in (2.55). The FRFs for the forced system follow (2.58) for mode 2. Note that there is a division by zero in this expression for the first mode because of the double root at zero (multiplicity is two), which (2.58) cannot accommodate.

It is evident that the computations for the general case of viscous damping are rather complicated. The computations become much simpler for a system exhibiting proportional damping. Because the example system studied here was specifically chosen to be proportionally damped, the eigenvectors are the same as for an undamped system, as shown previously. The damping matrix $\mathbf{C}$ can be transformed to the modal damping matrix of (2.64) if the following condition is true:

$$\left(\mathbf{M}^{-1}\mathbf{K}\right)\left(\mathbf{M}^{-1}\mathbf{C}\right) = \left(\mathbf{M}^{-1}\mathbf{C}\right)\left(\mathbf{M}^{-1}\mathbf{K}\right) . \quad (2.96)$$

Evaluating (2.96) gives

$$\left(\mathbf{M}^{-1}\mathbf{K}\right)\left(\mathbf{M}^{-1}\mathbf{C}\right)=\left(\begin{bmatrix}1&0\\0&1\end{bmatrix}^{-1}\begin{bmatrix}1&-1\\-1&1\end{bmatrix}\right)\left(\begin{bmatrix}1&0\\0&1\end{bmatrix}^{-1}\begin{bmatrix}1&-1\\-1&1\end{bmatrix}\right)=\begin{bmatrix}2&-2\\-2&2\end{bmatrix} \quad \text{.(2.97)}$$
$$\left(\mathbf{M}^{-1}\mathbf{C}\right)\left(\mathbf{M}^{-1}\mathbf{K}\right)=\left(\begin{bmatrix}1&0\\0&1\end{bmatrix}^{-1}\begin{bmatrix}1&-1\\-1&1\end{bmatrix}\right)\left(\begin{bmatrix}1&0\\0&1\end{bmatrix}^{-1}\begin{bmatrix}1&-1\\-1&1\end{bmatrix}\right)=\begin{bmatrix}2&-2\\-2&2\end{bmatrix}$$

Therefore, the modal damping matrix is

$$\overline{\mathbf{C}}=\begin{bmatrix}0&0\\0&\dfrac{c\left(m_1+m_2\right)^2}{m_1{}^2}\end{bmatrix}=\begin{bmatrix}0&0\\0&4\end{bmatrix}. \quad (2.98)$$

So, for the unforced system,

$$\begin{bmatrix}2&0\\0&2\end{bmatrix}\ddot{\mathbf{q}}+\begin{bmatrix}0&0\\0&4\end{bmatrix}\dot{\mathbf{q}}+\begin{bmatrix}0&0\\0&4\end{bmatrix}\mathbf{q}=\mathbf{0} \quad (2.99)$$

giving

$$\ddot{q}_1=0 \quad (2.100)$$

and

$$\ddot{q}_2+2\dot{q}_2+2q_2=0\ . \quad (2.101)$$

The eigenvalues are computed from the characteristic polynomial. For the first mode, by inspection $\omega_1=\zeta_1=\lambda_1=0$ (shown earlier). For the second mode,

$$\begin{aligned}\omega_2&=\sqrt{\frac{\overline{k}_2}{\overline{m}_2}}=\sqrt{\frac{2}{1}}=\sqrt{2}\\ \zeta_2&=\frac{\overline{c}_2}{2\sqrt{\overline{m}_2\overline{k}_2}}=\frac{2}{2\sqrt{(1)(2)}}=\frac{\sqrt{2}}{2}\\ \omega_2'&=\omega_2\sqrt{1-\zeta_2^2}=\sqrt{2}\sqrt{1-\left(\frac{\sqrt{2}}{2}\right)^2}=1\end{aligned} \quad . \quad (2.102)$$

These values match those from the general case computed earlier. However, (2.102) shows that $\omega_2'\ll\omega_2$ due to a high modal damping value relative to modal

stiffness. As discussed, the mode shape matrix $\mathbf{V}$ is the same as for the undamped system in (2.77).

For comparison, the FRF for the first mass due to the second force is constructed below.

$$\begin{aligned}\mathbf{H}_{12}(\omega) &= \frac{\mathbf{V}_{11}\mathbf{V}_{21}}{\overline{k}_1 + i\omega\overline{c}_1 - \omega^2\overline{m}_1} + \frac{\mathbf{V}_{12}\mathbf{V}_{22}}{\overline{k}_2 + i\omega\overline{c}_2 - \omega^2\overline{m}_2} \\ &= \frac{1}{-2\omega^2} - \frac{1}{4 + 4i\omega - 2\omega^2}\end{aligned} . \tag{2.103}$$

The impulse response to the first mode, by inspection, is linear towards infinity, so it provides no new insight. The presence of damping greatly changes the behavior of the second mode (compare Figure 7 with Figure 6(c)). The oscillations damp out quickly because the damping is large. Notice in Figure 7 how the damping roughly halves the peak amplitude of oscillation of the undamped system.

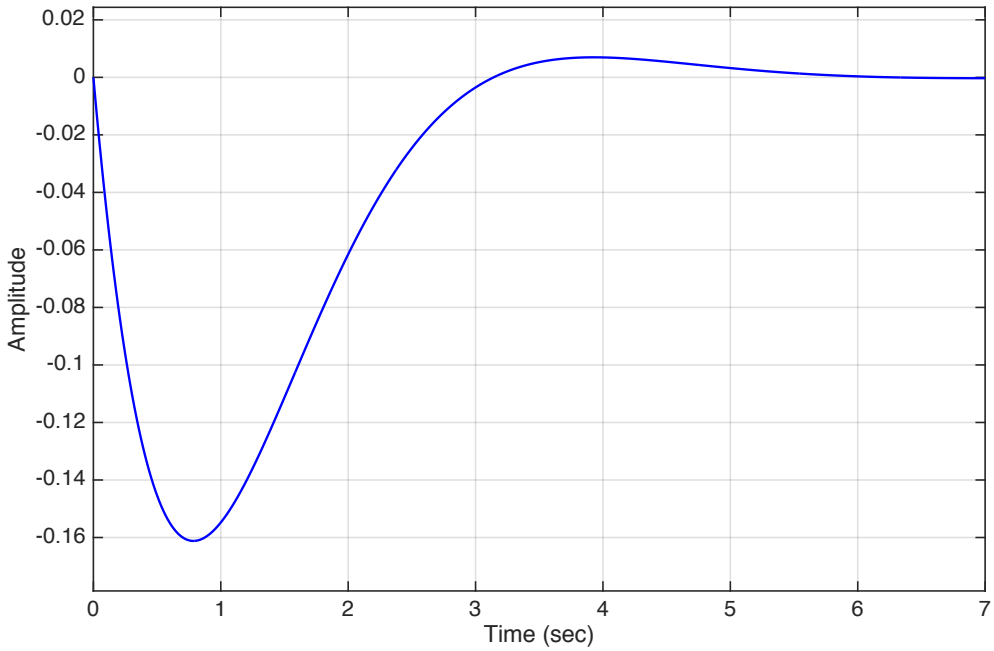

Figure 7. Proportionally damped impulse response of ${}_2\mathbf{H}_{12}$ for $c = 1$, $\overline{c}_2 = 4$.

As an illustration of the effect of the relationship between the damping and stiffness constants, Figure 8 shows the impulse response of the second mode when the value of damping is decreased by an order of magnitude to $c = 0.1$, while keeping $k = 1$. Less damping increases the settling time of the system while also increasing its peak amplitude.

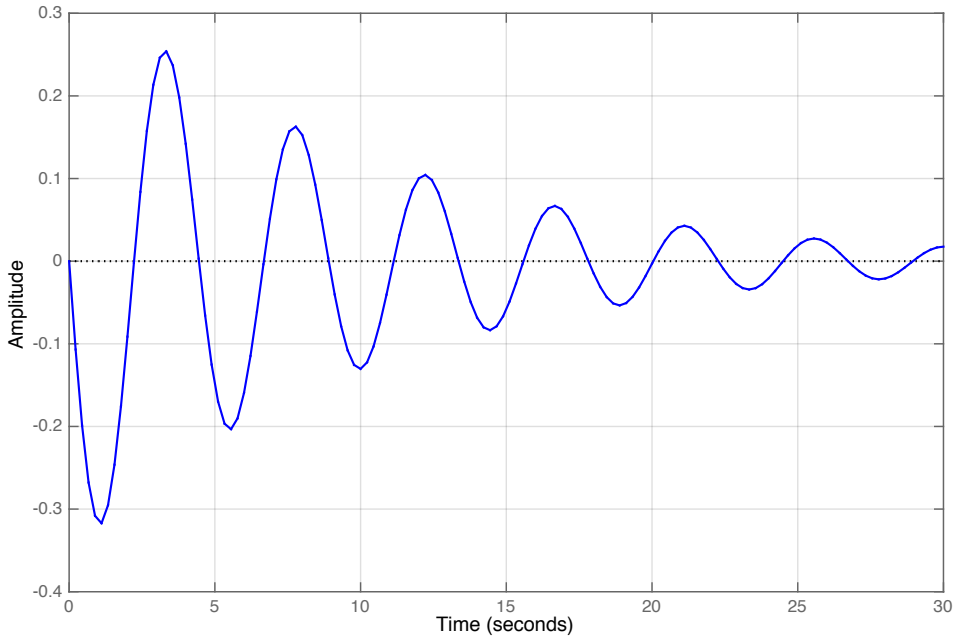

Figure 8. Proportionally damped impulse response of ${}_2\mathbf{H}_{12}$ for $c = 0.1$, $\overline{c}_2 = 0.4$.

G. FORCED VIBRATION WITH VISCOUS DAMPING IN THE LAPLACE DOMAIN

Modal analysis can also be completed in the Laplace domain, where manipulation of the equations is easier. Many conventional control techniques have deep roots in the Laplace domain. To work in the Laplace domain, simply substitute $\omega = s/i$ into the FRFs discussed previously.

Assuming zero initial conditions, Equation (2.1) describing the motion of the system in Figure 3 becomes $\mathbf{Z}(s)\mathbf{X}(s) = \mathbf{F}(s)$, where $\mathbf{Z}(s) = \mathbf{M}s^2 + \mathbf{C}s + \mathbf{K}$. Matrix $\mathbf{Z} \in \mathbb{R}^{nxn}$ is called the dynamic stiffness matrix [9]. The transfer function

$\mathbf{H} \in \mathbb{R}^{nxn}$ between the displacement $\mathbf{X} \in \mathbb{R}^{nx1}$ and applied force $\mathbf{F} \in \mathbb{R}^{nx1}$ is the inverse of the dynamic stiffness matrix and is given by

$$\mathbf{H}(s) = \left[\mathbf{M}s^2 + \mathbf{C}s + \mathbf{K}\right]^{-1} = \frac{\mathbf{N}(s)}{d(s)} = \frac{\text{adj}\left[\mathbf{M}s^2 + \mathbf{C}s + \mathbf{K}\right]}{\det\left[\mathbf{M}s^2 + \mathbf{C}s + \mathbf{K}\right]} \quad . \tag{2.104}$$

In (2.104), $d(s)$ is the characteristic polynomial, whose roots are the complex conjugate pole pairs, λ_r, of the system, and $\mathbf{N} \in \mathbb{R}^{nxn}$ is a matrix of numerator polynomials that relates to residues (discussed below). The roots of the characteristic polynomial are the same as the eigenvalues of the chain of single-DOF systems, discussed previously. Recall from (2.68) that λ_r contains both a real part and imaginary part, such that $\lambda_r = \omega_r \zeta_r \pm i\omega_r'$. The roots of the numerator polynomials are the zeros of the system [13].

The transfer function in (2.104) can be deconstructed into components separately describing motion of the system as a whole (termed “rigid-body”) and the oscillatory motion (“flexible-body”) using partial fraction expansion but only if the system, indeed, exhibits rigid-body motion. A more general case is discussed later. These components represent the modes from the previous section. For the 2-DOF system shown in Figure 3, we have (from (2.104))

$$\mathbf{H}(s) = \frac{\begin{bmatrix} m_2 s^2 + cs + k & cs + k \\ cs + k & m_1 s^2 + cs + k \end{bmatrix}}{s^2\left(m_1 m_2 s^2 + \left(m_1 + m_2\right)cs + \left(m_1 + m_2\right)k\right)} \quad . \tag{2.105}$$

Using partial fraction expansion on each element of $\mathbf{H}(s)$ allows the individual transfer functions between the bodies to be determined. Let $\mathbf{H}_{jk}(s)$ equal the transfer function for the displacement $\mathbf{X}_{jk}(s)$ and $\mathbf{F}_k(s)$, such that $\mathbf{X}_{jk}(s) = \mathbf{H}_{jk}(s)\mathbf{F}_k(s)$. In other words, $\mathbf{X}_{11}(s)$ is the displacement of x_1 due to f_1 and $\mathbf{X}_{12}(s)$ is the displacement of x_1 due to f_2. From (2.105),

$$\mathbf{H}_{11}(s)=\frac{a}{s^2}+\frac{b}{m_1m_2s^2+(m_1+m_2)cs+(m_1+m_2)k}\ . \tag{2.106}$$

The numerator of (2.106) is

$$a\left(m_1m_2s^2+(m_1+m_2)cs+(m_1+m_2)k\right)+bs^2=m_2s^2+cs+k\ . \tag{2.107}$$

Solving for a and b we obtain

$$\begin{aligned} a&=\frac{1}{m_1+m_2}\\ b&=m_2-\frac{m_1m_2}{m_1+m_2}\end{aligned}\ . \tag{2.108}$$

Substituting (2.108) back into (2.106) gives

$$\mathbf{H}_{11}(s)=\frac{1}{(m_1+m_2)s^2}+\frac{\dfrac{{m_2}^2}{m_1+m_2}}{m_1m_2s^2+(m_1+m_2)cs+(m_1+m_2)k}\ . \tag{2.109}$$

The first term in (2.109) represents the rigid-body motion of mass 1 (mode 1) while the second term represents the flexible-body motion (mode 2) due to its attachment to mass 2. Similarly, the remaining transfer functions are given by

$$\begin{aligned}\mathbf{H}_{12}(s)&=\frac{1}{(m_1+m_2)s^2}+\frac{-\dfrac{m_1m_2}{m_1+m_2}}{m_1m_2s^2+(m_1+m_2)cs+(m_1+m_2)k}\\ \mathbf{H}_{21}(s)&=\frac{1}{(m_1+m_2)s^2}+\frac{-\dfrac{m_1m_2}{m_1+m_2}}{m_1m_2s^2+(m_1+m_2)cs+(m_1+m_2)k}\\ \mathbf{H}_{22}(s)&=\frac{1}{(m_1+m_2)s^2}+\frac{\dfrac{{m_1}^2}{m_1+m_2}}{m_1m_2s^2+(m_1+m_2)cs+(m_1+m_2)k}\end{aligned}\ . \tag{2.110}$$

The symmetry is expected, as the motion of the two masses occurs only along the same axis, and they are only connected to each other. The first terms in each transfer function correspond to the rigid-body motion of the system. They

contribute to the first mode where $\omega_1 = 0$. The second terms model flexible-body motion and represent the second mode.

The residues of these functions are proportional to the modal vectors and can be used to construct the residue matrix $\mathbf{R}_r \in \mathbb{C}^{nxn}$ [11]. ("Residue" is analogous to "modal constant" shown previously.) In general, assuming all poles have multiplicity of one [9],

$$\mathbf{H}(s) = \sum_{r=1}^{n} \left(\frac{\mathbf{R}_r}{s - \lambda_r} + \frac{\mathbf{R}_r^*}{s - \lambda_r^*} \right) , \tag{2.111}$$

where λ_r and λ_r^* are the complex conjugate pole pairs and n is the number of modes (or degrees of freedom). Residues are computed using partial fraction expansion, as above. The mode shape of mode r is described by a matrix $\Psi \in \mathbb{C}^{nxn}$ whose columns are normalized modal vectors, ψ_r, proportional to the corresponding elements of $\mathbf{R}_r$. As was shown in the case of a proportionally damped system, the modal vector ψ_r equals $\mathbf{v}_r$ from the undamped case. The modal vectors are calculated by using the residues from one row or column of $\mathbf{H}$ (for both modes). Interestingly, since the system is proportionally damped, the residues will be purely imaginary [11].

The inverse Laplace transform of (2.111) gives the impulse response function $\mathbf{h}(t)$ studied earlier.

$$\mathbf{h}(t) = \sum_{r=1}^{n} \left(\mathbf{R}_r e^{\lambda_r t} + \mathbf{R}_r^* e^{\lambda_r^* t} \right) . \tag{2.112}$$

H. NUMERICAL EXAMPLE IN THE LAPLACE DOMAIN

Assume a nominal case where $m_1 = m_2 = c = k = 1$. For the undamped case, $\lambda_1 = 0$, $\lambda_2 = 2$, and $\mathbf{V} = \begin{bmatrix} 1 & -1 \\ 1 & 1 \end{bmatrix}$ (from (2.10) and (2.16)), and it follows that the natural frequencies are $\omega_1 = 0$ and $\omega_2 = \sqrt{2}$. Eigenvector $\mathbf{v}_2$ indicates

that the amplitudes of motion of both masses in mode 2 will be equal but in opposite directions.

The equations of motion in the Laplace domain become

$$\begin{aligned}
\mathbf{X}_{11}(s) &= \left(\frac{1}{s^2} + \frac{1}{s^2+2s+2}\right)\frac{1}{2}\mathbf{F}_1 \\
\mathbf{X}_{12}(s) &= \left(\frac{1}{s^2} - \frac{1}{s^2+2s+2}\right)\frac{1}{2}\mathbf{F}_2 \\
\mathbf{X}_{21}(s) &= \left(\frac{1}{s^2} - \frac{1}{s^2+2s+2}\right)\frac{1}{2}\mathbf{F}_1 \\
\mathbf{X}_{22}(s) &= \left(\frac{1}{s^2} + \frac{1}{s^2+2s+2}\right)\frac{1}{2}\mathbf{F}_2
\end{aligned} \quad . \tag{2.113}$$

It is readily apparent that the poles of the rigid-body component $(r=1)$ are at $s=0$. The rigid-body mode from the double-integrator terms in each equation implies that the system moves as a whole in the same direction due to the applied forces. The system's second mode comes from the oscillatory motion between the two masses, modeled in the second terms. Take the transfer function component of the second term of $\mathbf{X}_{12}(s)$. The poles and corresponding residues are

$$\begin{aligned}
\lambda_2 &= -1 \pm i \\
{}_2\mathbf{R}_{12} &= \pm\frac{1}{4}
\end{aligned} \quad . \tag{2.114}$$

Recall that the poles match the eigenvalues calculated earlier. The residues can be used to reconstruct the transfer function from (2.111).

$$\mathbf{H}_{12}(s) = \frac{\frac{1}{4}i}{s-(-1+i)} - \frac{\frac{1}{4}i}{s-(-1-i)} = \frac{\frac{1}{2}}{s^2+2s+2} \quad . \tag{2.115}$$

The residue matrix may be completed by following the same procedure.

$$\mathbf{R}_2 = \begin{bmatrix} \mp\frac{1}{4}i & \pm\frac{1}{4}i \\ \pm\frac{1}{4}i & \mp\frac{1}{4}i \end{bmatrix}. \tag{2.116}$$

The corresponding impulse response function is

$$_2\mathbf{h}_{12}(t) = \frac{1}{4}ie^{(-1+i)t} - \frac{1}{4}ie^{(-1-i)t} = -\frac{1}{2}e^{-t}\sin t \ . \tag{2.117}$$

The time history of (2.117) is precisely the same as the plot shown in Figure 7.

I. MASS-SPRING-DAMPER SYSTEM FIXED TO A STRUCTURE

Suppose now that the system from Figure 3 is connected on one side to a fixed structure, as in Figure 9. This connection represents a controller that may be implemented to stabilize the rigid motion of the flexible system.

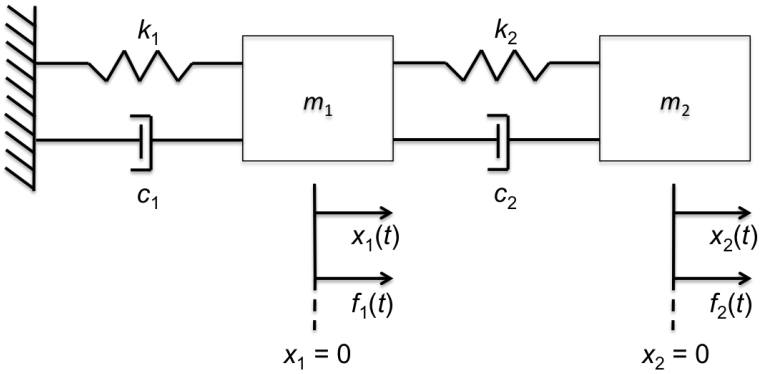

Figure 9. Two-DOF mass-spring-damper system.

The first mode of the system no longer exhibits rigid-body motion since the masses are fixed in place by the first spring-damper pair. The new equations of motion are

$$\begin{aligned} f_1 &= m_1\ddot{x}_1 + (c_1 + c_2)\dot{x}_1 + (k_1 + k_2)x_1 - c\dot{x}_2 - k_2x_2 \\ f_2 &= m_2\ddot{x}_2 - c_2\dot{x}_1 - k_2x_1 + c_2\dot{x}_2 + k_2x_2 \end{aligned} \tag{2.118}$$

which leads to

$$\mathbf{M}\ddot{\mathbf{x}}(t)+\mathbf{C}\dot{\mathbf{x}}(t)+\mathbf{K}\mathbf{x}(t)=\mathbf{f}(t)$$

$$\begin{bmatrix} m_1 & 0 \\ 0 & m_2 \end{bmatrix}\ddot{\mathbf{x}}(t)+\begin{bmatrix} c_1+c_2 & -c_2 \\ -c_2 & c_2 \end{bmatrix}\dot{\mathbf{x}}(t)+\begin{bmatrix} k_1+k_2 & -k_2 \\ -k_2 & k_2 \end{bmatrix}\mathbf{x}(t)=\mathbf{f}(t) \quad . \quad (2.119)$$

Assuming the same nominal values, $m_1=m_2=c_1=c_2=k_1=k_2=1$, the natural frequencies and mode shapes for the undamped, unforced system are given as

$$[\lambda_r]=[\omega_r{}^2]=\begin{bmatrix} 0.382 & 0 \\ 0 & 2.618 \end{bmatrix} \quad .$$
$$\mathbf{V}=\begin{bmatrix} 0.618 & -1.618 \\ 1 & 1 \end{bmatrix} \quad (2.120)$$

From (2.120), the modal matrices are obtained as

$$\overline{\mathbf{M}}=\begin{bmatrix} 0.618 & 1 \\ -1.618 & 1 \end{bmatrix}\begin{bmatrix} 1 & 0 \\ 0 & 1 \end{bmatrix}\begin{bmatrix} 0.618 & -1.618 \\ 1 & 1 \end{bmatrix}=\begin{bmatrix} 1.382 & 0 \\ 0 & 3.618 \end{bmatrix}$$
$$\overline{\mathbf{C}}=\begin{bmatrix} 0.618 & 1 \\ -1.618 & 1 \end{bmatrix}\begin{bmatrix} 2 & -1 \\ -1 & 1 \end{bmatrix}\begin{bmatrix} 0.618 & -1.618 \\ 1 & 1 \end{bmatrix}=\begin{bmatrix} 0.528 & 0 \\ 0 & 9.472 \end{bmatrix} \quad (2.121)$$
$$\overline{\mathbf{K}}=\begin{bmatrix} 0.618 & 1 \\ -1.618 & 1 \end{bmatrix}\begin{bmatrix} 2 & -1 \\ -1 & 1 \end{bmatrix}\begin{bmatrix} 0.618 & -1.618 \\ 1 & 1 \end{bmatrix}=\begin{bmatrix} 0.528 & 0 \\ 0 & 9.472 \end{bmatrix}$$

The equation of motion in modal coordinates is, therefore,

$$\begin{bmatrix} 1.382 & 0 \\ 0 & 3.618 \end{bmatrix}\ddot{\mathbf{q}}+\begin{bmatrix} 0.528 & 0 \\ 0 & 9.472 \end{bmatrix}\dot{\mathbf{q}}+\begin{bmatrix} 0.528 & 0 \\ 0 & 9.472 \end{bmatrix}\mathbf{q}=\begin{bmatrix} 0.618 & 1 \\ -1.618 & 1 \end{bmatrix}\mathbf{f} \quad .$$

The equations for each mode, after dividing through by $\overline{m}_r$, are thus

$$\ddot{q}_1+0.382\dot{q}_1+0.382q_1=0.447f_1+0.724f_2=\frac{f_1'}{1.382} \quad (2.122)$$

$$\ddot{q}_2+2.618\dot{q}_2+2.618q_2=-0.447f_1+0.276f_2=\frac{f_2'}{3.618} \quad . \quad (2.123)$$

These equations describe the motion of two single-DOF systems, where the motions of the modal masses are uncoupled and are of the form

$$\ddot{q}_r + 2\zeta_r \omega_r \dot{q}_r + \omega_r{}^2 q_r = \frac{f_r'}{\bar{m}_r} \quad . \tag{2.124}$$

For the forced system,

$$\begin{aligned} \omega_1 &= \sqrt{0.382} = 0.618 \\ \zeta_1 &= \frac{0.382}{(2)(0.618)} = 0.309 \\ \omega_1' &= 0.588 \end{aligned} \tag{2.125}$$

and

$$\begin{aligned} \omega_2 &= \sqrt{2.618} = 1.618 \\ \zeta_2 &= \frac{2.618}{(2)(1.618)} = 0.809 \\ \omega_2' &= 0.951 \end{aligned} \quad . \tag{2.126}$$

Equations (2.125) and (2.126) can be interpreted as follows: mode 1, with the smaller natural frequency, represents the main motion of the system, whereas mode 2, with the larger natural frequency, represents the flexible effect. This flexible effect perturbs the main motion of the system. In this context, it is desirable to minimize the magnitude of q_2 and its derivatives since the flexibility is parasitic to the performance of the control system. This result illustrates the primary reason why modal analysis is a valuable tool in control system design.

The controlled 2-DOF system shown in Figure 9 cannot be deconstructed into rigid-body and flexible-body components, as shown in the previous section, since motion of both masses is oscillatory. Assuming the same nominal values $m_1 = m_2 = c_1 = c_2 = k_1 = k_2 = 1$, in the Laplace domain the FRF is

$$\mathbf{H}(s) = \frac{\mathbf{N}(s)}{d(s)} = \frac{\text{adj}\left[\mathbf{M}s^2 + \mathbf{C}s + \mathbf{K}\right]}{\det\left[\mathbf{M}s^2 + \mathbf{C}s + \mathbf{K}\right]} = \frac{\begin{bmatrix} s^2 + s + 1 & s + 1 \\ s + 1 & s^2 + 2s + 2 \end{bmatrix}}{s^4 + 3s^3 + 4s^2 + 2s + 1} \quad , \tag{2.127}$$

where the poles are $\lambda_1 = -0.191 \pm 0.588i$ and $\lambda_2 = -1.311 \pm 0.951i$, which match the values computed previously. The residue matrices for each mode are

$$\mathbf{R}_1 = \begin{bmatrix} \mp 0.235i & \mp 0.380i \\ \mp 0.380i & \mp 0.615i \end{bmatrix}$$
$$\mathbf{R}_2 = \begin{bmatrix} \mp 0.380i & \pm 0.235i \\ \pm 0.235i & \mp 0.145i \end{bmatrix} . \quad (2.128)$$

Therefore, the mode shape matrix, using the first row of each residue matrix, is

$$\Psi = \begin{bmatrix} \frac{{}_1\mathbf{R}_{11}}{{}_1\mathbf{R}_{21}} & \frac{{}_2\mathbf{R}_{11}}{{}_2\mathbf{R}_{21}} \\ \frac{{}_1\mathbf{R}_{21}}{{}_1\mathbf{R}_{21}} & \frac{{}_2\mathbf{R}_{21}}{{}_2\mathbf{R}_{21}} \end{bmatrix} = \begin{bmatrix} \frac{-0.235}{-0.380} & \frac{-0.380}{0.235} \\ 1 & 1 \end{bmatrix} = \begin{bmatrix} 0.618 & -1.618 \\ 1 & 1 \end{bmatrix} . \quad (2.129)$$

While determining mode shapes and residues in the Laplace domain is straightforward, the transfer functions in $\mathbf{H}$ cannot be used to get the modal coordinates of the system. They do, however, provide meaningful representations of the behavior of the system in physical space.

J. SUMMARY

The motion of flexible multi-body systems is complicated due to the interaction between the various degrees of freedom. Modal analysis enables the description of the motion to be decomposed into a series of single-DOF systems, each with different modal properties (i.e., frequency and damping). Control applications are typically concerned with manipulating the behavior of the dominant (slow) modes while minimizing the excitation of the flexible (fast) modes. Thus, modal coordinates are a natural space for synthesis of rapid slew maneuvers, and this chapter has provided the necessary background for accomplishing this task.

III. CONVENTIONAL CONTROL OF A 3-DOF SYSTEM

This chapter increases the complexity of the mass-spring-damper system by adding a third DOF. The system is now analogous to a controlled spacecraft body with a flexible antenna mounted on a double-axis gimbal. The controller is used to maintain the spacecraft's position and move the links of the notional antenna. This chapter analyzes a model to understand the behavior of such a system from the perspective of conventional control techniques.

A. DEFINING THE MODEL

Consider the three-mass system shown in Figure 10. It is representative of a controlled spacecraft with a 2-DOF flexible appendage. In this case, the stiffness k_1 and damping c_1 can be attributed to the feedback control of the base body, whereas k_2, k_3, c_2, and c_3 are the stiffness and damping constants of the flexible appendage (locked in a specific orientation).

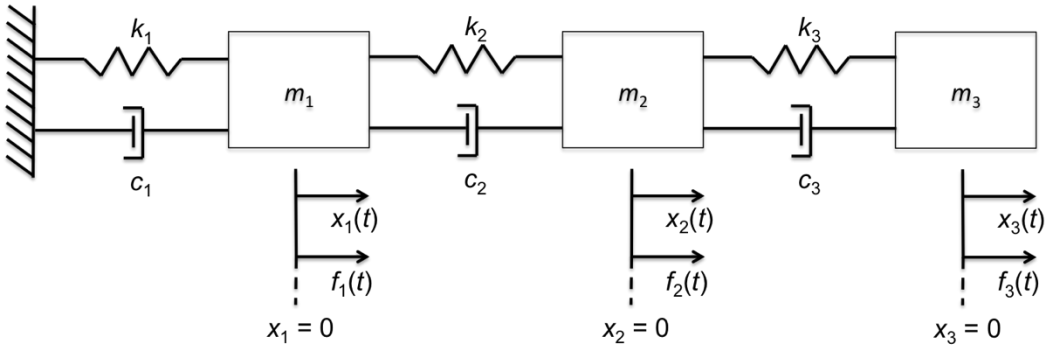

Figure 10. Mass-spring-damper system with three degrees of freedom.

The equations of motion governing this system are

$$\begin{aligned} f_1 &= m_1\ddot{x}_1 + (c_1 + c_2)\dot{x}_1 - c_2\dot{x}_2 + (k_1 + k_2)x_1 - k_2x_2 \\ f_2 &= m_2\ddot{x}_2 - c_2\dot{x}_1 + (c_2 + c_3)\dot{x}_2 - c_3\dot{x}_3 - k_2x_1 + (k_2 + k_3)x_2 - k_3x_3 \\ f_3 &= m_3\ddot{x}_3 - c_3\dot{x}_2 + c_3\dot{x}_3 - k_3x_2 + k_3x_3 \end{aligned} \quad . \tag{3.1}$$

Thus, $\mathbf{M} = \begin{bmatrix} m_1 & 0 & 0 \\ 0 & m_2 & 0 \\ 0 & 0 & m_3 \end{bmatrix}$, $\mathbf{C} = \begin{bmatrix} c_1 + c_2 & -c_2 & 0 \\ -c_2 & c_2 + c_3 & -c_3 \\ 0 & -c_3 & c_3 \end{bmatrix}$,

$\mathbf{K} = \begin{bmatrix} k_1 + k_2 & -k_2 & 0 \\ -k_2 & k_2 + k_3 & -k_3 \\ 0 & -k_3 & k_3 \end{bmatrix}$, $\mathbf{x}(t) = \begin{bmatrix} x_1(t) \\ x_2(t) \\ x_3(t) \end{bmatrix}$, and $\mathbf{f}(t) = \begin{bmatrix} f_1(t) \\ f_2(t) \\ f_3(t) \end{bmatrix}$. Unit values for each parameter in the system are assumed for convenience so that $m_1 = m_2 = m_3 = c_1 = c_2 = c_3 = k_1 = k_2 = k_3 = 1$.

B. ANALYSIS OF THE COUPLED SYSTEM

Using the method described in Chapter II, the transfer function matrix for the system in Figure 10 can be written as

$$\mathbf{H}(s) = \frac{\begin{bmatrix} s^4 + 3s^3 + 4s^2 + 2s + 1 & s^3 + 2s^2 + 2s + 1 & s^2 + 2s + 1 \\ s^3 + 2s^2 + 2s + 1 & s^4 + 3s^3 + 5s^2 + 4s + 2 & s^3 + 3s^2 + 4s + 2 \\ s^2 + 2s + 1 & s^3 + 3s^2 + 4s + 2 & s^4 + 4s^3 + 7s^2 + 6s + 3 \end{bmatrix}}{s^6 + 5s^5 + 11s^4 + 13s^3 + 9s^2 + 3s + 1}. \quad (3.2)$$

Recall that the poles of this transfer function matrix are the roots of the denominator polynomial (or "characteristic equation"), which are equal to the eigenvalues of the system

$$[\lambda_r] = \text{diag}\begin{bmatrix} -0.990 \pm 0.4339i & -0.7775 \pm 0.9749i & -1.6235 \pm 0.7818i \end{bmatrix}. \quad (3.3)$$

Using the procedure discussed in Chapter II, the undamped mode shape vectors, rounded to four decimal places, are

$$\mathbf{V} = \begin{bmatrix} 1 & 1 & 1 \\ 1.8019 & 0.4450 & -1.2470 \\ 2.2470 & -0.8019 & 0.5550 \end{bmatrix}. \quad (3.4)$$

The modal matrices, then, are

$$\begin{aligned}
\overline{\mathbf{M}} &= \mathbf{V}^T\mathbf{M}\mathbf{V} = \mathrm{diag}\begin{bmatrix} 9.2959 & 1.8412 & 2.8629 \end{bmatrix} \\
\overline{\mathbf{C}} &= \mathbf{V}^T\mathbf{C}\mathbf{V} = \mathrm{diag}\begin{bmatrix} 1.8412 & 2.8629 & 9.2959 \end{bmatrix} . \\
\overline{\mathbf{K}} &= \mathbf{V}^T\mathbf{K}\mathbf{V} = \mathrm{diag}\begin{bmatrix} 1.8412 & 2.8629 & 9.2959 \end{bmatrix}
\end{aligned} \tag{3.5}$$

From these equations, the natural and damped frequencies, ω_r and ω_r' (in radians per second), as well as the critical damping ratios, ζ_r, may be computed as

$$\begin{aligned}
[\omega_r] &= \mathrm{diag}\begin{bmatrix} 0.4450 & 1.2470 & 1.8019 \end{bmatrix} \\
[\zeta_r] &= \mathrm{diag}\begin{bmatrix} 0.2225 & 0.9749 & 0.7818 \end{bmatrix} . \\
[\omega_r'] &= \mathrm{diag}\begin{bmatrix} 0.4339 & 0.9749 & 0.7818 \end{bmatrix}
\end{aligned} \tag{3.6}$$

The relative values of the modal masses in (3.5) help to illustrate to an important property of this system. Modal mass $\overline{m}_1 = 9.2959$ is five times larger than $\overline{m}_2$ and over three times larger than $\overline{m}_3$. The damping ratios increase through the modes. One could hypothesize, then, that the motion of mass 1 dominates the total motion of the system, just as was observed in the system with rigid-body motion (see Chapter II). Analysis of the FRFs and IRFs will support this hypothesis. Figure 11 shows the Bode frequency response and Figure 12 shows the motion of mass 1 in response to impulse force 1 for all modes.

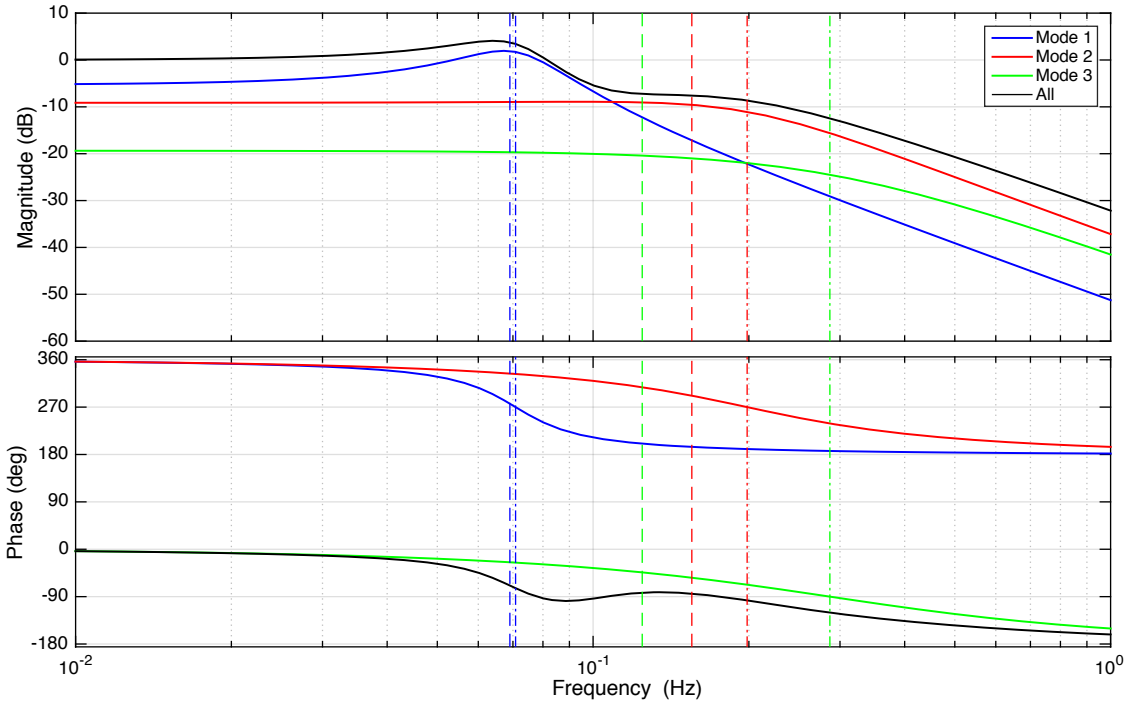

Figure 11. Bode magnitude and phase plot of $\mathbf{H}_{11}(\omega)$ for a 3-DOF system.

In Figure 11, the vertical dashed and dot-dashed lines represent the damped and natural frequencies for each mode, respectively. Clearly, the total motion of mass 1 due to force 1 is greatly impacted by mode 1, especially in the low frequency range. This is because the magnitudes of mode 2 and mode 3 are -10 dB and -20 dB, respectively, in the low frequency range. In the high frequency range, the responses of modes 2 and 3 dominate. This is why flexible systems oscillate; sudden changes in the applied force excite these high frequency effects. The impulse responses (Figure 12) confirm that mode 1 dominates the response and that modes 2 and 3 decay quickly due to the large damping. If this damping is reduced, the higher modes will be superposed onto mode 1 to a greater degree. This is the characteristic that degrades the performance of a control system and should be avoided via a combination of control and reference trajectory design. Figure 13 illustrates this point; it shows the IRF $\mathbf{h}_{11}(t)$ for reduced damping $(c_1 = c_2 = c_3 = 0.1)$.

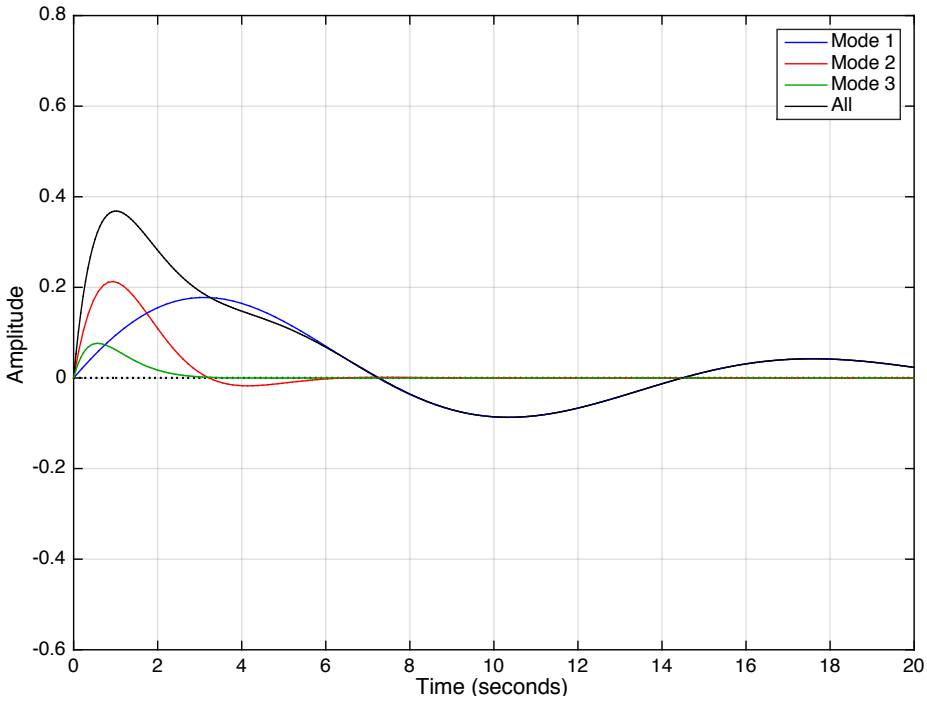

Figure 12. Impulse response function $\mathbf{h}_{11}(t)$ for a 3-DOF system with "heavy" damping $(c_1 = c_2 = c_3 = 1)$.

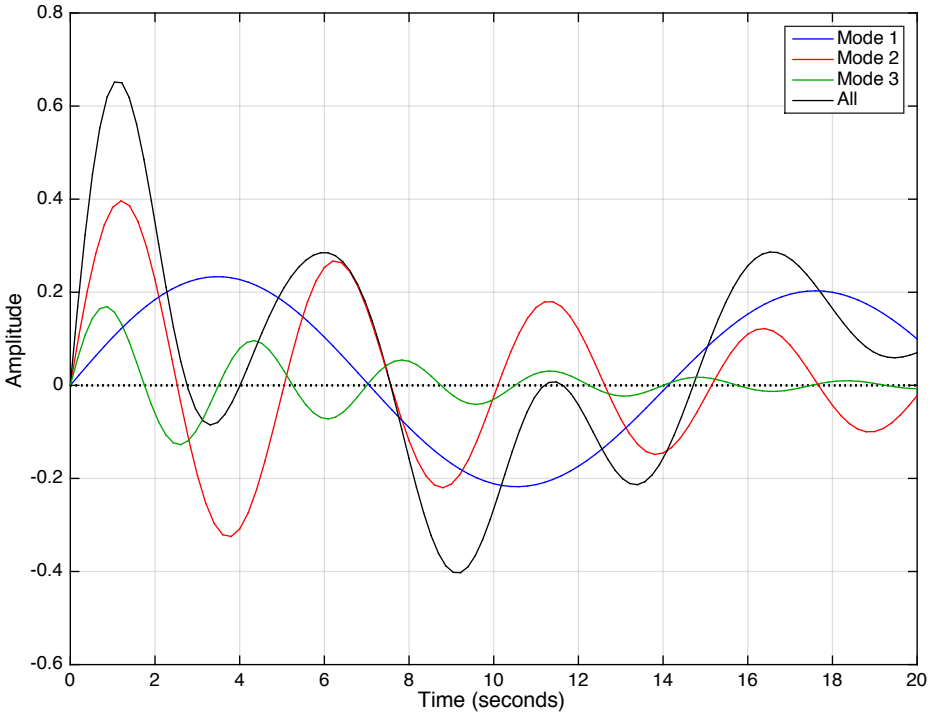

Figure 13. Impulse response function $\mathbf{h}_{11}(t)$ for a 3-DOF system with "light" damping $(c_1 = c_2 = c_3 = 0.1)$.

Figure 14 shows the impulse responses for the transfer function matrix in (3.2). The repeated impulse responses (as for $\mathbf{H}_{12}$ and $\mathbf{H}_{21}$, for example) result from the symmetry of the matrix $\mathbf{H}(s)$. It is apparent from the figure that m_2 and m_3 experience the greatest displacement about their equilibrium positions due to the forces acting on them. This follows due to the nature of the system; each mass is less constrained than its previous counterpart as one moves away from the fixed structure (base). In the control of a multi-body system, this is important because if forces 2 and 3 are not carefully controlled, they can cause large displacement of the base body (i.e., mass 1). See responses for $\mathbf{H}_{12}$ and $\mathbf{H}_{13}$ in Figure 14.

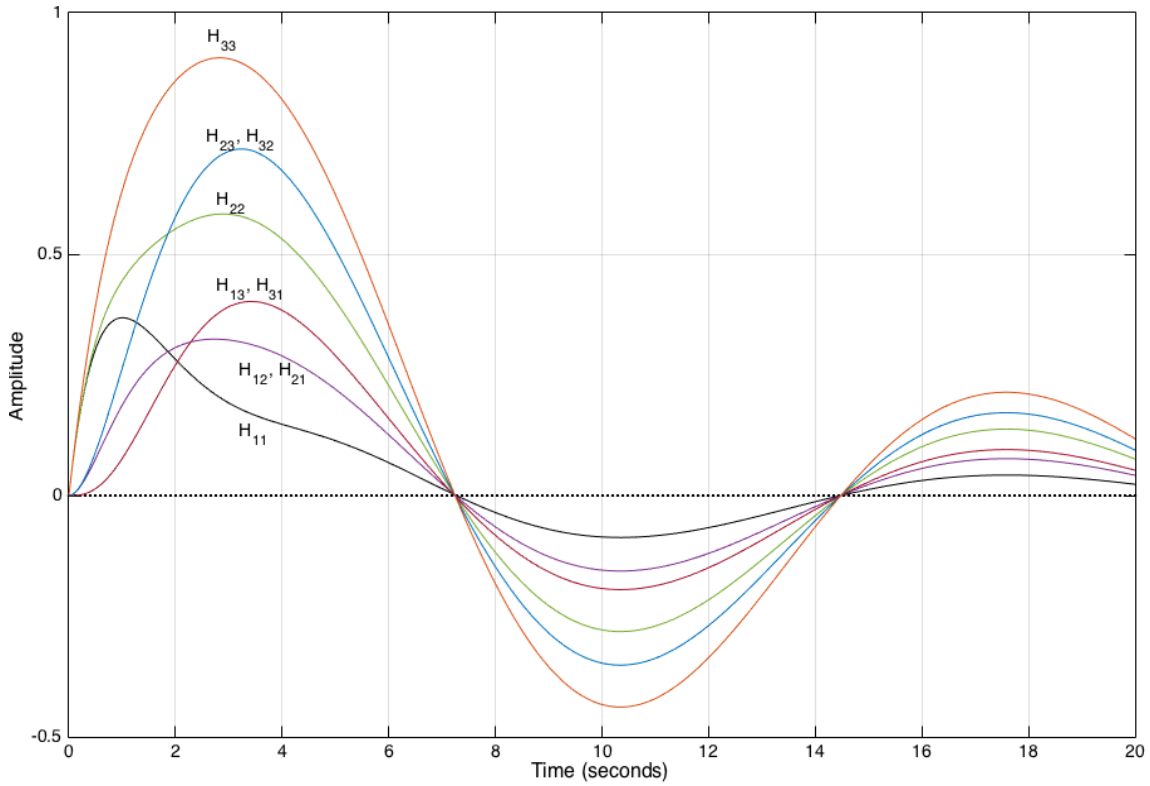

Figure 14. Impulse responses, $\mathbf{h}_{jk}(t)$, for system in Figure 10.

The residue matrices for each mode, using partial fraction expansion from Chapter II, are

$$\mathbf{R}_1 = \begin{bmatrix} \mp 0.1240i & \mp 0.2234i & \mp 0.2786i \\ \mp 0.2234i & \mp 0.4025i & \mp 0.5019i \\ \mp 0.2786i & \mp 0.5019i & \mp 0.6259i \end{bmatrix}$$

$$\mathbf{R}_2 = \begin{bmatrix} \mp 0.2786i & \mp 0.1240i & \pm 0.2234i \\ \mp 0.1240i & \mp 0.0552i & \pm 0.0994i \\ \pm 0.2234i & \pm 0.0994i & \mp 0.1791i \end{bmatrix}. \tag{3.7}$$

$$\mathbf{R}_3 = \begin{bmatrix} \mp 0.2234i & \pm 0.2786i & \mp 0.1240i \\ \pm 0.2786i & \mp 0.3473i & \pm 0.1546i \\ \mp 0.1240i & \pm 0.1546i & \mp 0.0688i \end{bmatrix}$$

These residues may be used to construct mode shape vectors

$$\Psi = \begin{bmatrix} \frac{{}_1\mathbf{R}_{11}}{{}_1\mathbf{R}_{11}} & \frac{{}_2\mathbf{R}_{11}}{{}_2\mathbf{R}_{11}} & \frac{{}_3\mathbf{R}_{11}}{{}_3\mathbf{R}_{11}} \\ \frac{{}_1\mathbf{R}_{21}}{{}_1\mathbf{R}_{11}} & \frac{{}_2\mathbf{R}_{21}}{{}_2\mathbf{R}_{11}} & \frac{{}_3\mathbf{R}_{21}}{{}_3\mathbf{R}_{11}} \\ \frac{{}_1\mathbf{R}_{31}}{{}_1\mathbf{R}_{11}} & \frac{{}_2\mathbf{R}_{31}}{{}_2\mathbf{R}_{11}} & \frac{{}_3\mathbf{R}_{31}}{{}_3\mathbf{R}_{11}} \end{bmatrix} = \begin{bmatrix} 1 & 1 & 1 \\ \frac{-0.2234i}{-0.1240i} & \frac{-0.1240i}{-0.2786i} & \frac{0.2786i}{-0.2234i} \\ \frac{-0.2786i}{-0.1240i} & \frac{0.2234i}{-0.2786i} & \frac{-0.1240i}{-0.2234i} \end{bmatrix}. \tag{3.8}$$

$$= \begin{bmatrix} 1 & 1 & 1 \\ 1.8019 & 0.4450 & -1.2470 \\ 2.2470 & -0.8019 & 0.5550 \end{bmatrix}$$

Figure 15 plots these mode shapes. Recall that a plot like Figure 15 is useful in understanding the relative motions of each degree of freedom of the system for each modal frequency. Each line in Figure 15 represents a single mode mapped to each DOF. For instance, motion of mode 1 (blue line) causes all three masses to move in the same direction (because each amplitude has the same sign) but with varying magnitudes. One should expect m_3 to oscillate at more than double the amplitude of m_1 (2.25:1 ratio) and only slightly more than m_2 (1.80:1 ratio). Mode 2 (red line) would see m_3 moving in a direction opposite the other two

masses because its amplitude has the opposite sign of the other two, and so on. (It can also be shown that these mode shapes can be formed from the peak amplitudes of the imaginary parts of their FRFs.)

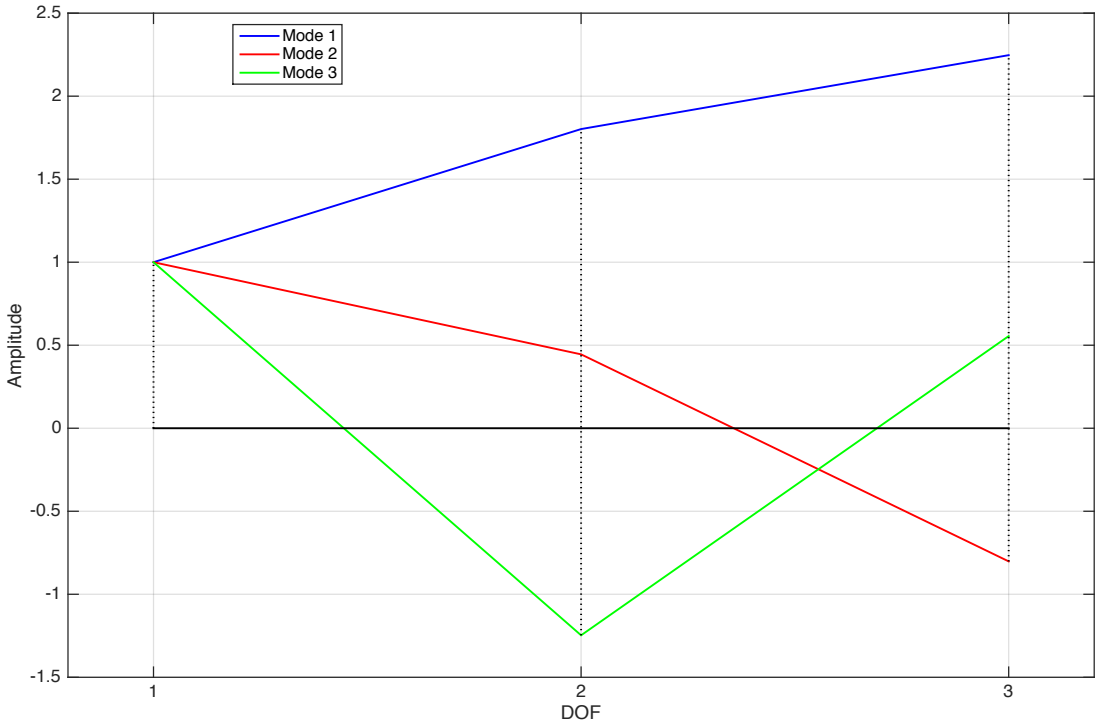

Figure 15. Mode shapes of 3-DOF system $\left(c_1 = c_2 = c_3 = 1\right)$.

C. MODELING A SPACECRAFT SLEW

With minor modifications, Figure 10 can be used as a representative model for a spacecraft antenna slew. Suppose a steerable antenna is attached to the body of a spacecraft (see Figure 16) by a two-axis gimbal. For simplicity, assume the center of rotation of the gimbal is aligned with its center of mass, and the antenna is mounted in such a way that there is no offset between it and the spacecraft body.

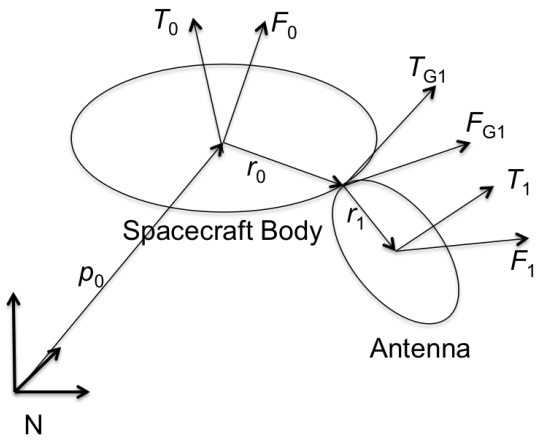

Figure 16. Notional schematic for a two-axis antenna mounted on a spacecraft body, after [5].

The system in Figure 10 in its current form can be used as a notional model for the flexible component of motion (vibrations) resulting from the forces applied to the azimuth and elevation bodies, where the spacecraft body is analogous to m_1, azimuth to m_2, and elevation to m_3. The spring and damper connecting mass 1 to the rigid structure represents the spacecraft controller that seeks to counteract the motion induced by the antenna and maintain the spacecraft in a certain position. The forces applied to the antenna to complete the slew are the forces that are input into the equations of motion in (3.1). The forces are also the inputs to simulations of the transfer function $\mathbf{H}(s)$ in (3.2).

In order to model the entire maneuver—not only the flexible motion in the notional antenna's locked position—Figure 10 must be modified to include the gross motion of the notional gimbals. A revised model is shown in Figure 17. The model shows that masses 2 and 3 have moved to new equilibrium positions defined by the desired final position at time t_f, while the flexible-body motion has been preserved and referenced to a non-stationary equilibrium point.

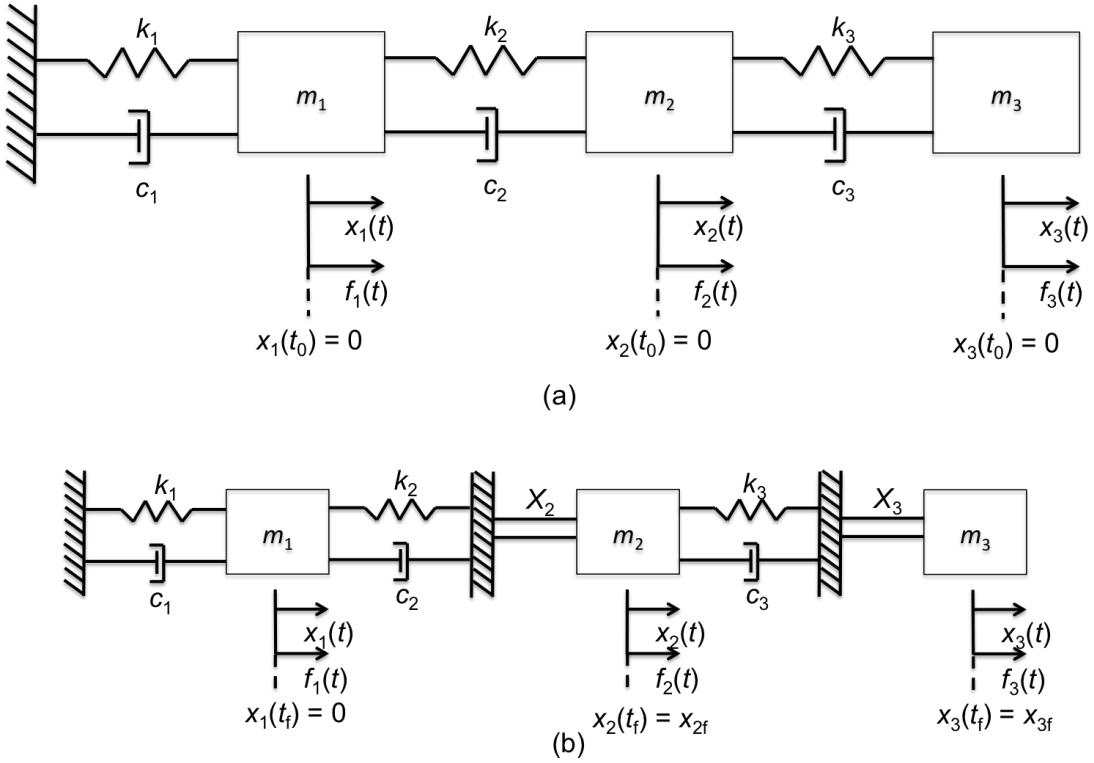

Figure 17. Three-DOF system modeling rigid translation with flexible effects: (a) initial position; (b) final position.

Let $X_2 = x_2(t) - x_2(t_0)$ and $X_3 = x_3(t) - x_3(t_0)$ be the translation of each mass as the prismatic joints are moved. The motion of the masses now also includes what can be equated to rigid-body motion. The total motion of the masses is the sum of this rigid-body motion and the flexible-body component for each mass. Thus, the equations for the total motion become

$$\begin{aligned} f_1 &= m_1\ddot{X}_1 + m_1\ddot{x}_1 + (c_1 + c_2)\dot{x}_1 - c_2\dot{x}_2 + (k_1 + k_2)x_1 - k_2x_2 \\ f_2 &= m_2\ddot{X}_2 + m_2\ddot{x}_2 - c_2\dot{x}_1 + (c_2 + c_3)\dot{x}_2 - c_3\dot{x}_3 - k_2x_1 + (k_2 + k_3)x_2 - k_3x_3 \\ f_3 &= m_3\ddot{X}_3 + m_3\ddot{x}_3 - c_3\dot{x}_2 + c_3\dot{x}_3 - k_3x_2 + k_3x_3 \end{aligned} \tag{3.9}$$

where $X_1 = \dot{X}_1 = \ddot{X}_1 = 0$ since the translation of the base is zero. The total motion of the system is the linear superposition of the rigid-body motion and the vibrational effects.

D. SLEWING WITH COMPUTED TORQUE CONTROL

Assume the following boundary conditions and constraints for a notional antenna slew are:

$$\begin{aligned}\left(X_1(t_0),X_2(t_0),X_3(t_0),\dot{X}_1(t_0),\dot{X}_2(t_0),\dot{X}_3(t_0)\right)&=(0,-10,5,0,0,0.1)\\ \left(X_1(t_f),X_2(t_f),X_3(t_f),\dot{X}_1(t_f),\dot{X}_2(t_f),\dot{X}_3(t_f)\right)&=(0,15,-15,0,0.1,0)\\ \left|\dot{X}_{\max}\right|&=0.75\\ \left|f_{\max}\right|&=1.5\\ \left(t_0,t_f\right)&=(0,38.1)\end{aligned} \quad , \quad (3.10)$$

where X_2 and $\dot{X}_2$ are the translation and velocity, respectively, in the notional azimuth plane, and X_3 and $\dot{X}_3$ are the translation and velocity, respectively, in the notional elevation plane. Both planes are fixed relative to the spacecraft body frame. The parameters in Figure 17 are, again, assigned unit values.

Common practice for implementing a slew maneuver to satisfy (3.10) is to use a so-called bang-bang or bang-off-bang trajectory where the maximum allowable force is applied over a short period of time to accelerate each movable joint, then the same magnitude of force is applied in the opposite direction to decelerate the links to their desired positions. This approach leads to the idea of computed torque control, in which required forces are generated from knowledge of the current state and its comparison to a desired profile. The control system uses feedback about the current state to determine the amount of control to apply [4]. By this method, the spacecraft can maneuver along the prescribed path. A control law for such a system takes the form given in (3.11), which is a simple PD controller.

$$f=K_p\left(x_d-x\right)+K_d\left(\dot{x}_d-\dot{x}\right) . \quad (3.11)$$

In (3.11), K_p and K_d are gains that can be programmed to achieve desired characteristics of the system. This method most likely produces a suboptimal solution but is easy to implement. Figure 18 shows the results of the maneuver

implementation using computed torque control for a rigid-body model; it also shows the behavior of the system after completion of the slew (indicated by the circles). Gains for the system are based on a one-second settling time with critical damping (ζ = 1) to minimize overshoot. The control law in (3.11) is applied to both axes (azimuth and elevation) independently to achieve the desired final conditions in (3.10) within the desired time of 38.1 seconds.

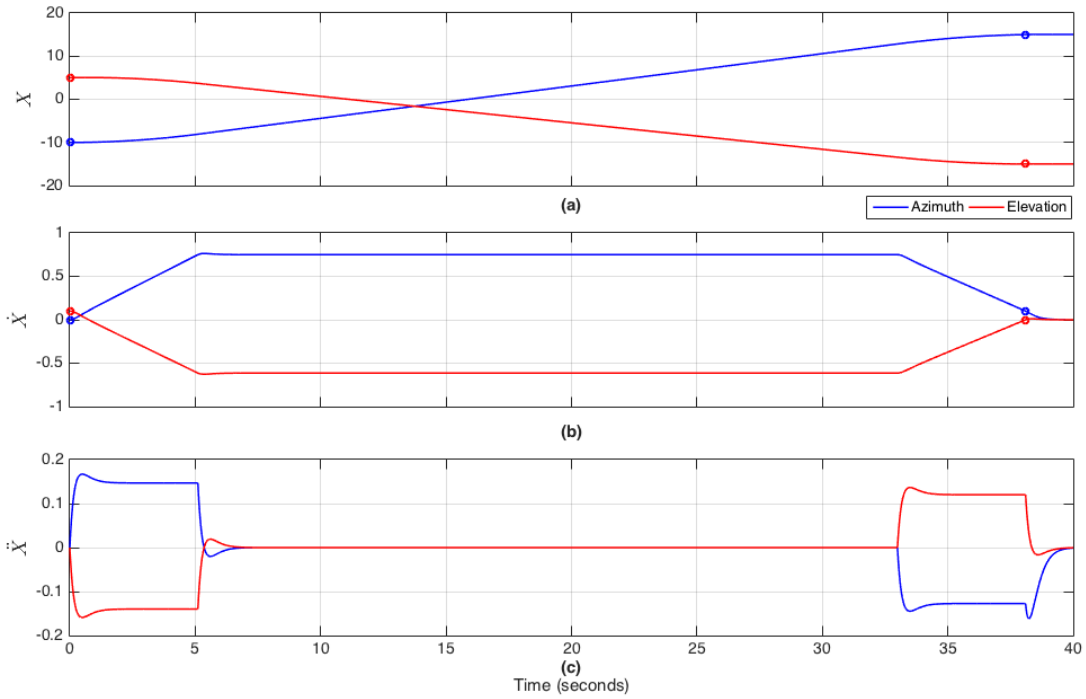

Figure 18. Rigid-body slew maneuver using computed torque control: (a) position; (b) rate; (c) acceleration.

To model the flexible-body motion of the system, the responses of the transfer function matrix in (3.2) can be simulated by applying the forces produced from the control law in (3.11).[2] Recall that $\mathbf{X}(s) = \mathbf{H}(s)\mathbf{F}(s)$, or $\mathbf{X}_j(s) = \mathbf{H}_{jk}(s)\mathbf{F}_k(s)$ for $j = 1,2,3$ and $k = 1,2,3$. Therefore,

[2] MATLAB's "lsim" command is very useful for this.

$$
\begin{aligned}
x_1(s) &= \mathbf{H}_{11}(s)\mathbf{F}_1(s) + \mathbf{H}_{12}(s)\mathbf{F}_2(s) + \mathbf{H}_{13}(s)\mathbf{F}_3(s) \\
x_2(s) &= \mathbf{H}_{21}(s)\mathbf{F}_1(s) + \mathbf{H}_{22}(s)\mathbf{F}_2(s) + \mathbf{H}_{23}(s)\mathbf{F}_3(s) \\
x_3(s) &= \mathbf{H}_{31}(s)\mathbf{F}_1(s) + \mathbf{H}_{32}(s)\mathbf{F}_2(s) + \mathbf{H}_{33}(s)\mathbf{F}_3(s)
\end{aligned}
\quad . \tag{3.12}
$$

We are only concerned at this point with x_2 and x_3 (the control law will be set to maintain $x_1 \approx 0$). Figure 19 shows the results.

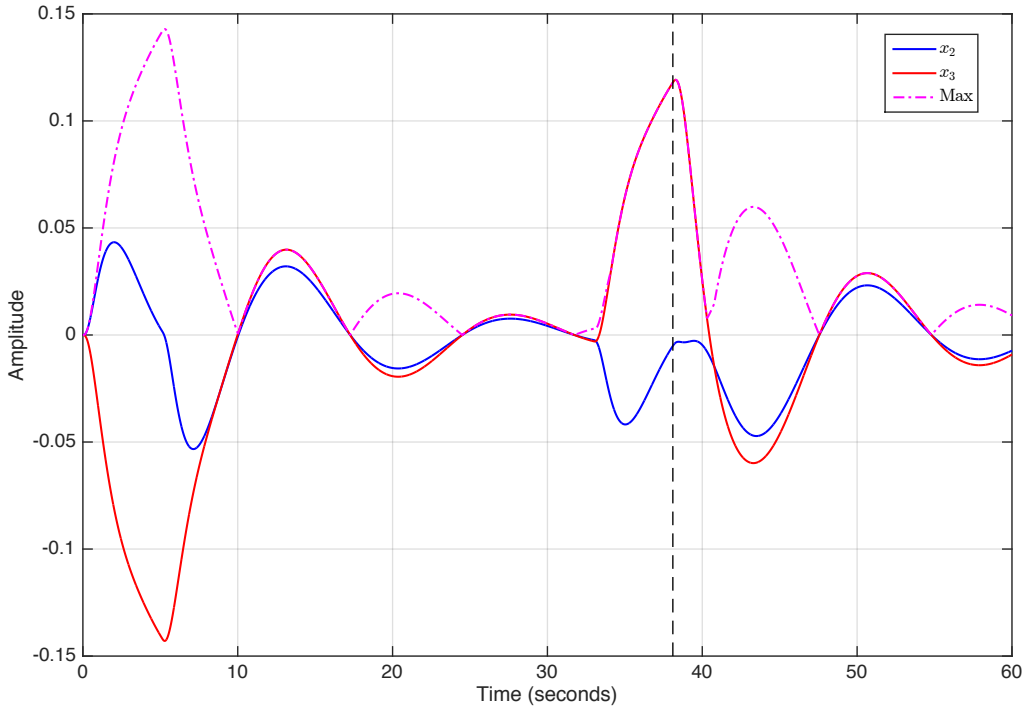

Figure 19. Flexible motion due to slew in Figure 18.

Note how the peak amplitudes of the vibrational components coincide with the changes in acceleration in Figure 18, though the vibrations occur on a much smaller scale than the gross motion of the system. In addition, there is some flexible spillover. In other words, even though the gross motion is fixed beyond $t_f = 38.1$, the system continues to oscillate in accordance with (3.12).

Suppose now that it is desired to constrain vibrations to within 0.1 position units for both links. A difficulty in using computed torque control arises because one must set the appropriate limits on force and velocity to ensure this constraint

can be met. Finding these limits requires “tweaking” the specifications of the system until the desired effect is achieved. However, the total slew time can increase, which may not be desirable. For example, an increase in slew time of three seconds to 41.1 seconds reduces vibrations to below the constraint (see Figure 20). Figure 21 compares the acceleration commands for each case; the controller applies less torque during the slower maneuver, and this is the mechanism used to reduce the magnitudes of the oscillations. Hence, using a conventional computed torque strategy, the only way to control flexible effects is by manipulating the acceleration of the joints. This is why a flexible antenna must be slewed slowly to avoid such disturbances.

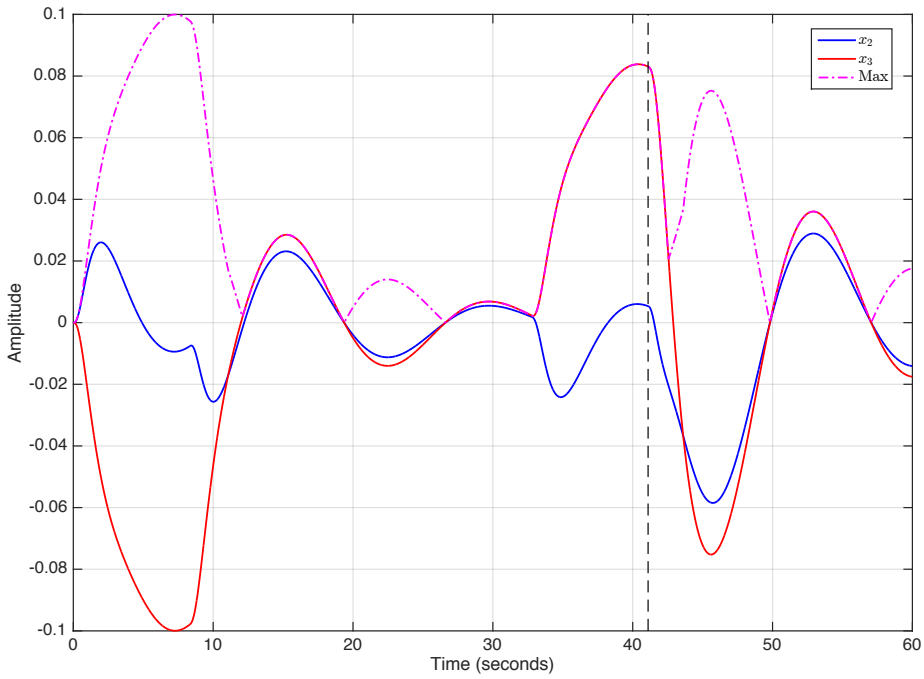

Figure 20. Reducing the flexible effects by increasing the slew time.

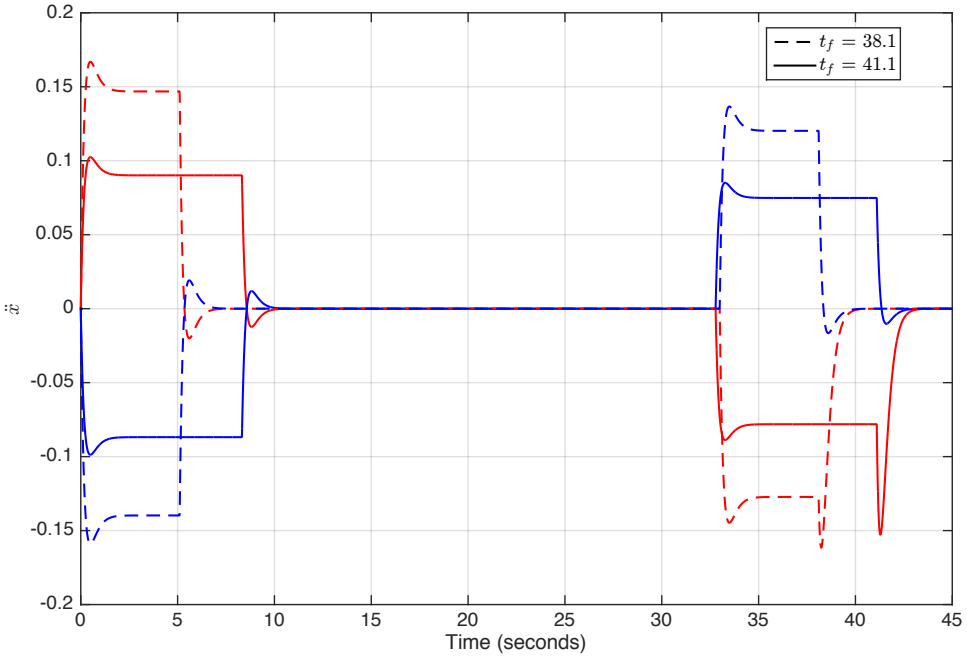

Figure 21. Comparison of acceleration for different slew maneuver times.

E. SUMMARY

In this chapter, the mass-spring-damper model was expanded to include a third degree of freedom. This system is analogous to a spacecraft body with an antenna mounted on a double-axis gimbal. Conventional control techniques were then used to perform a notional antenna slew to illustrate the resulting flexible effects. Finally, it was shown that when using conventional control flexible effects can only be reduced by increasing slew time. There is no analytical process for determining the time increase that would properly constrain vibrations, so the process can be tedious. This simple exercise illustrates the state of practice; meeting constraints on vibrations is handled by operating the system more conservatively. However, this limits system throughput since slew time is wasted time. In the next chapter, optimal control is used to develop slew maneuvers that alleviate these issues.

THIS PAGE INTENTIONALLY LEFT BLANK

IV. OPTIMAL CONTROL OF A 3-DOF SYSTEM

It is desired to minimize slew time in order to maximize throughput. In addition, vibrational effects due to force inputs should be limited to their existing specifications. That is, moving faster should not perturb the system any more than the preset solution. Rather than use conventional control to minimize flexible effects, and potentially increase slew time, it is possible to determine an alternate control to minimize both flexibility and slew time. This can be done by manipulating the system through application of force in such a way that the flexible properties of the system may be used to an advantage. Finding such a solution can be done by formulating and solving an optimal control problem.

Following [6], the problem must be redefined to satisfy the necessary conditions to achieve optimal control of the system. First, the dynamics of the system must be determined in state-space form. The correct definition of the state and control variables is crucial to a successful optimal control solution. Once the states and controls are properly defined, we can proceed to redefine our problem statement.

To construct an optimal control problem, a cost functional $J\left(\mathbf{x}(\bullet),\mathbf{u}(\bullet)\right)$ to be minimized should be identified. The cost, a function of the state vector $\mathbf{x}$ and control vector $\mathbf{u}$ in the system, consists of an endpoint cost (expressed in terms of the final state values) and/or a running cost (calculated for each time step). Thus, the cost functional can be expressed as

$$J\left(\mathbf{x}(\bullet),\mathbf{u}(\bullet)\right) = E\left(\mathbf{x}\left(t_f\right)\right) + \int_{t_0}^{t_f} F\left(\mathbf{x}(t),\mathbf{u}(t)\right)dt \ . \tag{4.1}$$

For minimum-time solutions, the cost functional is simply $J = t_f$, but variations of this simple objective function are described below.

The next step is to define any boundary conditions for the states, controls, and time. Any constraints on states or controls, (e.g., $|f_{\max}| = 1.5$), can also be applied. The redefined problem statement could be written as

$$\begin{aligned} \text{Minimize} \quad & J = t_f \\ \text{Subject to} \quad & \dot{\mathbf{x}} = \mathbf{f}\left(\mathbf{x}(t), \mathbf{u}(t)\right) \\ & \mathbf{x}(t_0) = \begin{bmatrix} x_1(0) & x_2(0) & \cdots & x_n(0) \end{bmatrix}^T \\ & t_0 = 0 \\ & \mathbf{e}\left(\mathbf{x}(t_f)\right) = 0 \\ & \mathbf{x}_L \le \mathbf{x}_i \le \mathbf{x}_U, \; i = 1,2,\ldots n \\ & \mathbf{u}_L \le \mathbf{u}_i \le \mathbf{u}_U, \; i = 1,2,\ldots m \end{aligned} \quad . \tag{4.2}$$

To solve (4.2), the Hamiltonian must be derived. The Hamiltonian is a function of the states, costates, and controls, where the vector of costates is related to the dynamics of the system [6]. The Hamiltonian is defined as

$$H(\mathbf{x}, \lambda, \mathbf{u}) = F(\mathbf{x}, \mathbf{u}) + \lambda^T \mathbf{f}(\mathbf{x}, \mathbf{u}) \tag{4.3}$$

where λ are the costates.

The necessary conditions to achieve an optimal control solution can now be determined [6]. The first necessary condition is the Hamiltonian minimization condition, written as

$$\frac{\partial H}{\partial \mathbf{u}} = \mathbf{0} \; . \tag{4.4}$$

The second necessary condition is the satisfaction of the adjoint equation(s)

$$\dot{\lambda}(t) = -\frac{\partial H}{\partial \mathbf{x}} \; . \tag{4.5}$$

The transversality condition relates the final values of the costates to the Endpoint Lagrangian and comprises the third necessary condition, written as

$$\lambda(t_f) = \frac{\partial \bar{E}}{\partial \mathbf{x}(t_f)} \tag{4.6}$$

where the Endpoint Lagrangian $\bar{E}\left(\nu,\mathbf{x}\left(t_f\right)\right)=E\left(\mathbf{x}\left(t_f\right)\right)+\nu^T\mathbf{e}\left(\mathbf{x}\left(t_f\right)\right)$ [6].

The MATLAB software package DIDO automatically determines an optimal control solution that satisfies the above conditions [6]. DIDO is used to solve the optimal control problems posed through the rest of this thesis.

A. STATE-SPACE FORM OF COUPLED SYSTEM

To construct the optimal control problem, the system in (3.9) must be transformed to state-space form. Assuming unit values for mass, stiffness, and damping, let $\mathbf{y}\in\mathbb{R}^{3x1}$ be the total displacement of each mass such that

$$\mathbf{y}=\begin{bmatrix} y_1 \\ y_2 \\ y_3 \end{bmatrix}=\begin{bmatrix} x_1+X_1 \\ x_2+X_2 \\ x_3+X_3 \end{bmatrix}. \tag{4.7}$$

Let $\mathbf{z}\in\mathbb{R}^{6x1}$ be a state vector such that

$$\mathbf{z}=\begin{bmatrix} \mathbf{y} \\ \dot{\mathbf{y}} \end{bmatrix}=\begin{bmatrix} x_1+X_1 \\ x_2+X_2 \\ x_3+X_3 \\ \dot{x}_1+\dot{X}_1 \\ \dot{x}_2+\dot{X}_2 \\ \dot{x}_3+\dot{X}_3 \end{bmatrix}. \tag{4.8}$$

Let $\mathbf{u}\in\mathbb{R}^{3x1}$ be the control vector $\mathbf{u}=\begin{bmatrix} f_1 & f_2 & f_3 \end{bmatrix}^T$, (i.e., the vector of forces acting on each mass). The states represent the total motion described by the sum of the rigid-body component and the flexible-body component, as described by (3.9). The generic state-space representation for a rigid-body slew is

$$\begin{bmatrix} \dot{X} \\ \ddot{X} \end{bmatrix}=\begin{bmatrix} 0 & 1 \\ 0 & 0 \end{bmatrix}\begin{bmatrix} X \\ \dot{X} \end{bmatrix}+\begin{bmatrix} 0 \\ \dfrac{1}{m} \end{bmatrix}\mathbf{f}\ , \tag{4.9}$$

where X is the displacement, $\dot{X} = v$ is the velocity, $\ddot{X} = a$ is the acceleration, m is the mass, and $\mathbf{f}$ is the control force. This state-space form, adapted for the 3-DOF system, is

$$\begin{bmatrix} \dot{X}_1 \\ \dot{X}_2 \\ \dot{X}_3 \\ \ddot{X}_1 \\ \ddot{X}_2 \\ \ddot{X}_3 \end{bmatrix} = \begin{bmatrix} 0 & 0 & 0 & 1 & 0 & 0 \\ 0 & 0 & 0 & 0 & 1 & 0 \\ 0 & 0 & 0 & 0 & 0 & 1 \\ 0 & 0 & 0 & 0 & 0 & 0 \\ 0 & 0 & 0 & 0 & 0 & 0 \\ 0 & 0 & 0 & 0 & 0 & 0 \end{bmatrix} \begin{bmatrix} X_1 \\ X_2 \\ X_3 \\ \dot{X}_1 \\ \dot{X}_2 \\ \dot{X}_3 \end{bmatrix} + \begin{bmatrix} 0 & 0 & 0 \\ 0 & 0 & 0 \\ 0 & 0 & 0 \\ \frac{1}{m_1} & 0 & 0 \\ 0 & \frac{1}{m_2} & 0 \\ 0 & 0 & \frac{1}{m_3} \end{bmatrix} \mathbf{u} , \qquad (4.10)$$

where $\mathbf{u} = \begin{bmatrix} 0 & f_2 & f_3 \end{bmatrix}^T$ since the restoring force is due to the control law on mass 1 comprising k_1 and c_1 (which will be accounted for as part of the flexible dynamics). The flexible-body component in state-space form becomes

$$\begin{bmatrix} \dot{x}_1 \\ \dot{x}_2 \\ \dot{x}_3 \\ \ddot{x}_1 \\ \ddot{x}_2 \\ \ddot{x}_3 \end{bmatrix} = \begin{bmatrix} 0 & 0 & 0 & 1 & 0 & 0 \\ 0 & 0 & 0 & 0 & 1 & 0 \\ 0 & 0 & 0 & 0 & 0 & 1 \\ -\frac{(k_1+k_2)}{m_1} & \frac{k_2}{m_1} & 0 & -\frac{(c_1+c_2)}{m_1} & \frac{c_2}{m_1} & 0 \\ \frac{k_2}{m_2} & -\frac{(k_2+k_3)}{m_2} & \frac{k_3}{m_2} & \frac{c_2}{m_2} & -\frac{(c_2+c_3)}{m_2} & \frac{c_3}{m_2} \\ 0 & \frac{k_3}{m_3} & -\frac{k_3}{m_3} & 0 & \frac{c_3}{m_3} & -\frac{c_3}{m_3} \end{bmatrix} \begin{bmatrix} x_1 \\ x_2 \\ x_3 \\ \dot{x}_1 \\ \dot{x}_2 \\ \dot{x}_3 \end{bmatrix} . \qquad (4.11)$$

$$+ \begin{bmatrix} 0 & 0 & 0 \\ 0 & 0 & 0 \\ 0 & 0 & 0 \\ \frac{1}{m_1} & 0 & 0 \\ 0 & \frac{1}{m_2} & 0 \\ 0 & 0 & \frac{1}{m_3} \end{bmatrix} \mathbf{u}$$

Developing the state-space representation using (4.8) as the state vector is grueling. One cannot simply add the rigid- and flexible-body state-space equations together to produce a form that is conducive to modal analysis. The difficulty lies in that the flexible motion equations contain no $\mathbf{X}$ terms or their time derivatives. For example, the equation for $\dot{z}_4$ is

$$\dot{z}_4 = \ddot{x}_1 + \ddot{X}_1 = 2f_1 - 2x_1 + x_2 - 2\dot{x}_1 + \dot{x}_2 \ . \tag{4.12}$$

Instead, separate the rigid-body and flexible-body components and define a new state vector. Let $\mathbf{y} \in \mathbb{R}^{12x1}$ be the state vector

$$\mathbf{y} = \begin{bmatrix} X_1 & X_2 & X_3 & \dot{X}_1 & \dot{X}_2 & \dot{X}_3 & x_1 & x_2 & x_3 & \dot{x}_1 & \dot{x}_2 & \dot{x}_3 \end{bmatrix}^T \tag{4.13}$$

and

$$\dot{\mathbf{y}} = \begin{bmatrix} \dot{X}_1 & \dot{X}_2 & \dot{X}_3 & \ddot{X}_1 & \ddot{X}_2 & \ddot{X}_3 & \dot{x}_1 & \dot{x}_2 & \dot{x}_3 & \ddot{x}_1 & \ddot{x}_2 & \ddot{x}_3 \end{bmatrix}^T \ . \tag{4.14}$$

The state-space representation, with unit values substituted, is therefore

$$\dot{\mathbf{y}} = \begin{bmatrix} 0 & 0 & 0 & 1 & 0 & 0 & 0 & 0 & 0 & 0 & 0 & 0 \\ 0 & 0 & 0 & 0 & 1 & 0 & 0 & 0 & 0 & 0 & 0 & 0 \\ 0 & 0 & 0 & 0 & 0 & 1 & 0 & 0 & 0 & 0 & 0 & 0 \\ 0 & 0 & 0 & 0 & 0 & 0 & 0 & 0 & 0 & 0 & 0 & 0 \\ 0 & 0 & 0 & 0 & 0 & 0 & 0 & 0 & 0 & 0 & 0 & 0 \\ 0 & 0 & 0 & 0 & 0 & 0 & 0 & 0 & 0 & 0 & 0 & 0 \\ 0 & 0 & 0 & 0 & 0 & 0 & 0 & 0 & 0 & 1 & 0 & 0 \\ 0 & 0 & 0 & 0 & 0 & 0 & 0 & 0 & 0 & 0 & 1 & 0 \\ 0 & 0 & 0 & 0 & 0 & 0 & 0 & 0 & 0 & 0 & 0 & 1 \\ 0 & 0 & 0 & 0 & 0 & 0 & -2 & 1 & 0 & -2 & 1 & 0 \\ 0 & 0 & 0 & 0 & 0 & 0 & 1 & -2 & 1 & 1 & -2 & 1 \\ 0 & 0 & 0 & 0 & 0 & 0 & 0 & 1 & -1 & 0 & 1 & -1 \end{bmatrix} \mathbf{y} + \begin{bmatrix} 0 & 0 & 0 \\ 0 & 0 & 0 \\ 0 & 0 & 0 \\ 1 & 0 & 0 \\ 0 & 1 & 0 \\ 0 & 0 & 1 \\ 0 & 0 & 0 \\ 0 & 0 & 0 \\ 0 & 0 & 0 \\ 1 & 0 & 0 \\ 0 & 1 & 0 \\ 0 & 0 & 1 \end{bmatrix} \mathbf{u} \ . \tag{4.15}$$

Equation (4.15) provides the dynamics required for the optimal control problem definition. Recall that (4.15) represents coupled motion in physical space. The time-optimal slew given the conditions in (3.10) and dynamics in (4.15) can be determined by solving the following problem:

$$
\begin{aligned}
\text{Minimize} \quad & J = t_f \\
\text{Subject to} \quad & \dot{y}_1 = y_4 \\
& \dot{y}_2 = y_5 \\
& \dot{y}_3 = y_6 \\
& \dot{y}_4 = u_1 \\
& \dot{y}_5 = u_2 \\
& \dot{y}_6 = u_3 \\
& \dot{y}_7 = y_{10} \\
& \dot{y}_8 = y_{11} \\
& \dot{y}_9 = y_{12} \\
& \dot{y}_{10} = -2y_7 + y_8 - 2y_{10} + y_{11} + u_1 \\
& \dot{y}_{11} = y_7 - 2y_8 + y_9 + y_{10} - 2y_{11} + y_{12} + u_2 \\
& \dot{y}_{12} = y_8 - y_9 + y_{11} - y_{12} + u_3 \\
& \left(y_2(t_0), y_3(t_0), y_5(t_0), y_6(t_0)\right) = (-10, 5, 0, 0.1) \\
& \left(y_2(t_f), y_3(t_f), y_5(t_f), y_6(t_f)\right) = (15, -15, 0.1, 0) \\
& t_0 = 0 \\
& |y_i| \le 0.75, i = 4,5,6 \\
& |u_i| \le 1.5, i = 1,2,3
\end{aligned}
\quad . \qquad (4.16)
$$

The dynamics in (4.16) are such that constraining the total motion of the system is simple. However, they do not readily provide modal characteristics. The dynamics are expressed in physical space, so the modes cannot be constrained directly. The dynamics must be uncoupled by transforming them to modal space, thereby enabling effective mode constraints.

B. UNCOUPLING THE 3-DOF SYSTEM

The system as constructed exhibits proportional damping. Therefore, the undamped mode shape vectors can be used to diagonalize the mass, damping, and stiffness matrices to produce the modal matrices, and thus the system can easily be uncoupled into three single-DOF systems of the form

$$
\bar{m}_r \ddot{q}_r + \bar{c}_r \dot{q}_r + \bar{k}_r q_r = f_r' \ , \qquad (4.17)
$$

where r is the mode number. Recall from Chapter II that $\mathbf{f}' = \mathbf{V}^T\mathbf{f}$. The transfer functions in the Laplace domain can then be found easily. Assuming $\mathbf{q}(0) = \dot{\mathbf{q}}(0) = \mathbf{0}$,

$$\mathbf{Q}_r s^2 + \frac{\overline{c}_r}{\overline{m}_r}\mathbf{Q}_r s + \frac{\overline{k}_r}{\overline{m}_r}\mathbf{Q}_r = \frac{\mathbf{F}_r'}{\overline{m}_r}$$

$$\mathbf{Q}_r(s) = \mathbf{H}_r(s)\mathbf{F}_r'(s) = \frac{\frac{1}{\overline{m}_r}}{s^2 + \frac{\overline{c}_r}{\overline{m}_r}s + \frac{\overline{k}_r}{\overline{m}_r}}\mathbf{F}_r'(s) \quad . \tag{4.18}$$

These transfer functions represent displacement in modal coordinates due to the transformed forces, and they are much easier to derive and manipulate than the transfer function matrix in (3.2). It is important to distinguish the difference between an uncoupled transfer function in modal (principal) coordinates versus a coupled transfer function in physical coordinates.

The uncoupled equations of motion from (4.17) are

$$\begin{aligned} \ddot{q}_1 + 0.1981\dot{q}_1 + 0.1981q_1 &= \frac{f_1'}{9.2959} \\ \ddot{q}_2 + 1.5550\dot{q}_2 + 1.5550q_2 &= \frac{f_2'}{1.8412} \\ \ddot{q}_3 + 1.5550\dot{q}_3 + 1.5550q_3 &= \frac{f_3'}{2.8629} \end{aligned} \quad . \tag{4.19}$$

These equations represent uncoupled modal masses as in Figure 22. The optimal control problem definition can now be redefined in terms of modal coordinates. Let the state vector be defined as

$$\mathbf{y} = \begin{bmatrix} X_1 & X_2 & X_3 & \dot{X}_1 & \dot{X}_2 & \dot{X}_3 & q_1 & q_2 & q_3 & q_4 & q_5 & q_6 \end{bmatrix}^T , \tag{4.20}$$

where $\begin{bmatrix} q_4 & q_5 & q_6 \end{bmatrix}^T = \begin{bmatrix} \dot{q}_1 & \dot{q}_2 & \dot{q}_3 \end{bmatrix}^T$, and

$$\dot{\mathbf{y}} = \begin{bmatrix} \dot{X}_1 & \dot{X}_2 & \dot{X}_3 & \ddot{X}_1 & \ddot{X}_2 & \ddot{X}_3 & \dot{q}_1 & \dot{q}_2 & \dot{q}_3 & \dot{q}_4 & \dot{q}_5 & \dot{q}_6 \end{bmatrix}^T . \tag{4.21}$$

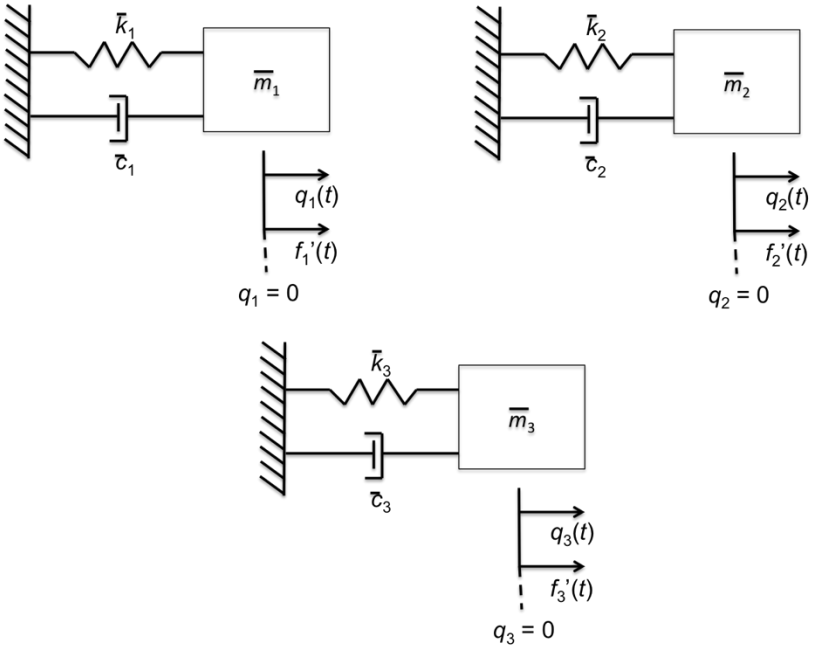

Figure 22. Uncoupled 3-DOF mass-spring-damper system.

The control vector remains $\mathbf{u} = \begin{bmatrix} 0 & f_2 & f_3 \end{bmatrix}^T$. However, the dynamics equations for the flexible component defined by $\begin{bmatrix} \dot{y}_7 & \cdots & \dot{y}_{12} \end{bmatrix}^T$ must account for the transformation from physical coordinates to modal coordinates. For example, from (4.19) we can see that

$$\ddot{q}_1 = \frac{f_1'}{9.2959} - 0.1981\dot{q}_1 - 0.1981 q_1 \ . \tag{4.22}$$

Because $f_1' = V_{11}f_1 + V_{21}f_2 + V_{31}f_3 = m_1\left(V_{11}a_1 + V_{21}a_2 + V_{31}a_3\right)$ and $\dot{q}_1 = q_4$, the general form is

$$\dot{q}_4 = \frac{m_1}{\bar{m}_1}\left(V_{11}a_1 + V_{21}a_2 + V_{31}a_3\right) - \frac{\bar{c}_1}{\bar{m}_1} q_4 - \frac{\bar{k}_1}{\bar{m}_1} q_1 \ . \tag{4.23}$$

Thus, the general form of the optimal control problem in modal coordinates can be defined as in (4.24). Note that there are no constraints or terminal boundary conditions placed on the flexible motion in the problem statement. The effects of constraining the flexibilities are discussed in a later section.

$$
\begin{aligned}
&\text{Minimize} && J = t_f \\
&\text{Subject to} && \dot{y}_1 = y_4 \\
& && \dot{y}_2 = y_5 \\
& && \dot{y}_3 = y_6 \\
& && \dot{y}_4 = \frac{u_1}{m_1} \\
& && \dot{y}_5 = \frac{u_2}{m_2} \\
& && \dot{y}_6 = \frac{u_3}{m_3} \\
& && \dot{y}_7 = y_{10} \\
& && \dot{y}_8 = y_{11} \\
& && \dot{y}_9 = y_{12} \\
& && \dot{y}_{10} = \frac{1}{\overline{m}_1}\left(V_{11}u_1 + V_{21}u_2 + V_{31}u_3\right) - \frac{\overline{c}_1}{\overline{m}_1} y_{10} - \frac{\overline{k}_1}{\overline{m}_1} y_7 \\
& && \dot{y}_{11} = \frac{1}{\overline{m}_2}\left(V_{12}u_1 + V_{22}u_2 + V_{32}u_3\right) - \frac{\overline{c}_2}{\overline{m}_2} y_{11} - \frac{\overline{k}_2}{\overline{m}_2} y_8 \\
& && \dot{y}_{12} = \frac{1}{\overline{m}_3}\left(V_{13}u_1 + V_{23}u_2 + V_{33}u_3\right) - \frac{\overline{c}_3}{\overline{m}_3} y_{12} - \frac{\overline{k}_3}{\overline{m}_3} y_9 \\
& \left(y_1(t_0), y_2(t_0), y_3(t_0), y_4(t_0), y_5(t_0), y_6(t_0)\right) = (0,-10,5,0,0,0.1) \\
& \left(y_1(t_f), y_2(t_f), y_3(t_f), y_4(t_f), y_5(t_f), y_6(t_f)\right) = (0,15,-15,0,0.1,0) \\
& \left(y_7(t_0), y_8(t_0), y_9(t_0), y_{10}(t_0), y_{11}(t_0), y_{12}(t_0)\right) = (0,0,0,0,0,0) \\
& |y_i| \le 0.75,\ i = 4,5,6 \\
& |u_i| \le 1.5,\ i = 1,2,3
\end{aligned}
\qquad .(4.24)
$$

C. SLEW OPTIMIZATION WITH NO CONSTRAINTS ON VIBRATIONS

The MATLAB package DIDO [6] was used for optimizing and validating the minimum-time maneuver. The minimum-time maneuver is presented in Figure 23. For both axes, the maximum acceleration (instead of some fraction of it) is supplied initially and at the end of the maneuver for a much shorter time than in the computed torque case. It is worth noting that y_3 does not follow the exact same trajectory as in the computed torque slew in Figure 18. The acceleration is not supplied in a "bang-off-bang" method but rather oscillates slightly. Because $y_2(t_f) - y_2(0) > y_3(t_f) - y_3(0)$, the azimuth axis becomes the limiting axis. As a result, the elevation axis has additional freedom in the path it

takes to the desired endpoint. This is why the acceleration applied to that axis is not uniform. As an analogy, picture two baseballs being thrown simultaneously from the same initial position with the same constraint on maximum velocity, but with the first baseball's target 10 feet further than the second's. The shortest travel time for the first baseball dictates the shortest travel time total for both baseballs together. The second baseball's velocity does not need to match the first baseball's velocity to reach its target at the same time. For the optimal control problem in (4.24), that time is 33.8 seconds, a savings of 4.3 seconds (12.7%) over the computed torque maneuver.

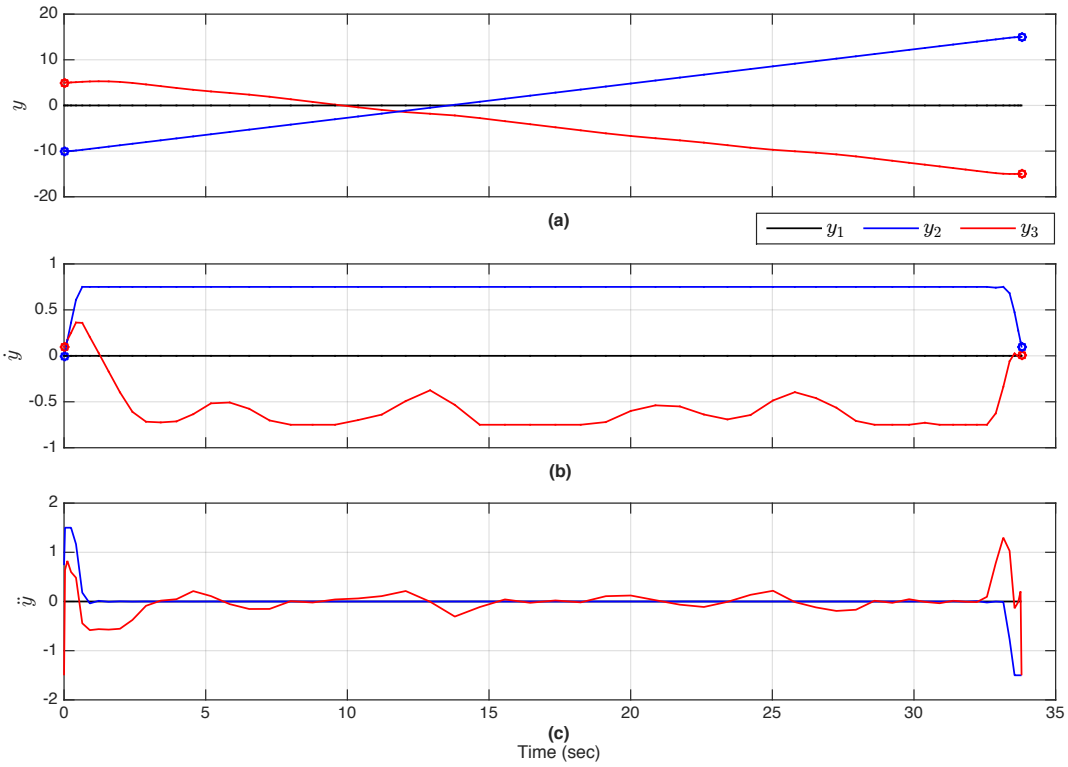

Figure 23. Rigid-body results of optimal control problem defined in (4.24) $\left(t_f = 33.8\right)$: (a) position; (b) rate; (c) acceleration.

Figure 24 shows the resulting flexible motion in both modal coordinates (in terms of $\mathbf{q}$) and physical coordinates (in terms of $\mathbf{x}$). Recall that $\mathbf{x} = \mathbf{V}\mathbf{q}$ and that $q_r \neq x_r$. Rather, q_1 represents the motion of all masses with respect to mode 1,

while x_1 is the physical displacement of mass 1 only, and so on. Figure 24 also illustrates the relationship $\mathbf{x} = \mathbf{V}\mathbf{q}$. For example, $\mathbf{q}(5) = \begin{bmatrix} -0.1165 & -0.0231 & 0.0051 \end{bmatrix}^T$, and the second row of the mode shape matrix is $\begin{bmatrix} 1.8019 & 0.4450 & -1.2470 \end{bmatrix}$. Thus, $x_2(5) = -0.2266$, as the plot shows. It is also evident that mode 1 dominates the total motion of the system.

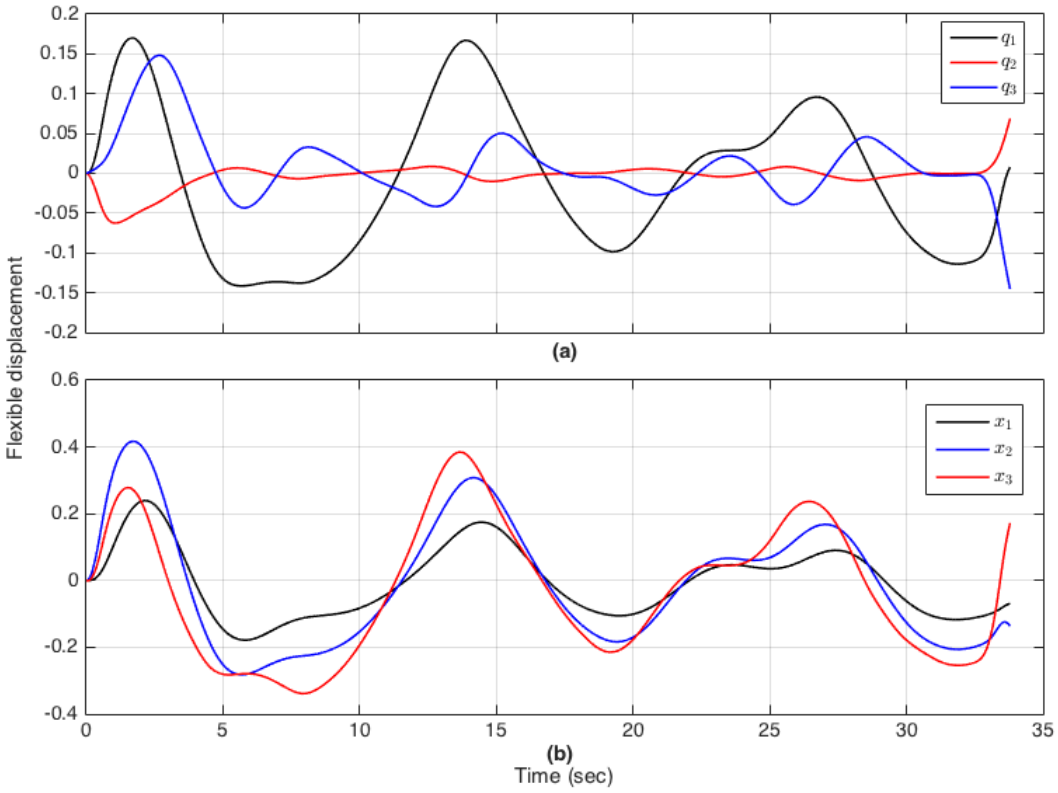

Figure 24. Flexible-body results of optimal control problem (4.24): (a) modal coordinates; (b) physical coordinates.

The added freedom in the path of y_3 (discussed previously) allows control designers to apply cost reduction measures to the system. For example, it is possible to find a minimum-time maneuver that also minimizes the energy expended to control the non-limiting axis. In this case, the problem definition in (4.24) can be altered to minimize the cost function

$$J = 200\int_0^{t_f} \mathbf{u}^2\, dt + t_f \tag{4.25}$$

subject to the same dynamics and boundary conditions/constraints. The integral term in the cost function represents a running cost, in that it is calculated and summed at each time step, and it is weighted 200 times against the endpoint cost of final time. By doing this, the control (energy) is reduced while also minimizing time. The new angular rates and accelerations for the revised optimal slew are shown in Figure 25. The displacement of y_3 now more closely matches the computed torque slew while completing the maneuver in the same time as Figure 23. Due to (4.25), the maneuver realizes additional savings in energy expended.

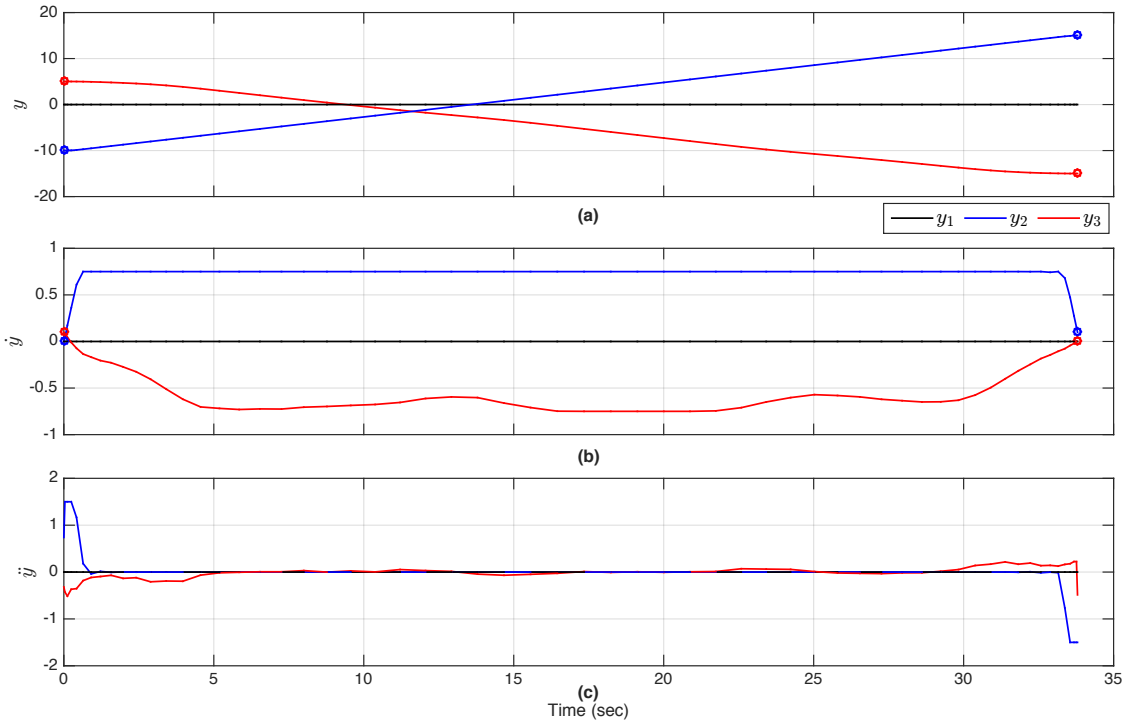

Figure 25. Rigid-body results of minimum-time slew with running cost to minimize control effort $\left(t_f = 33.8\right)$: (a) position; (b) rate; (c) acceleration.

The new acceleration profile ostensibly affects vibrations, shown in Figure 26 and Figure 27. In Figure 26, mode 1 again clearly dominates the total motion of the system but in a more pronounced way as the spacecraft minimizes its control input. Modes 2 and 3 show less oscillation than before (compare Figure 24 to Figure 26).

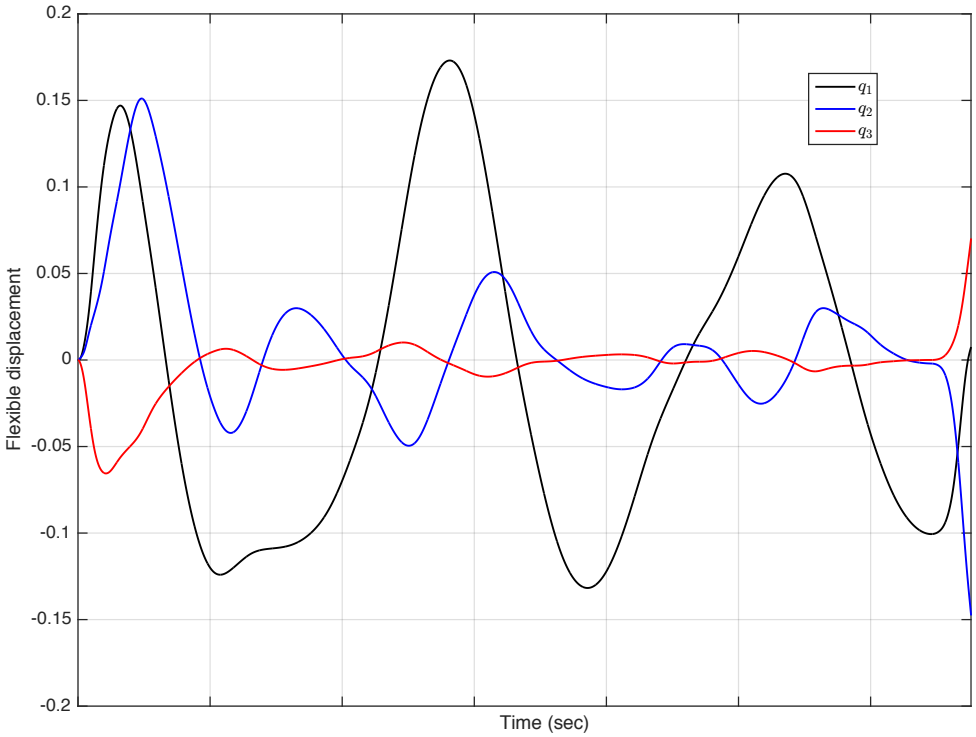

Figure 26. Flexible-body results of optimal control problem with running cost in modal coordinates.

Figure 27 shows a comparison of each mass's displacement (magnitudes only) for each optimal control solution (minimum-time and minimum-time plus minimum control effort). The addition of a running cost generally reduces the magnitude of displacement across all three masses, which follows as the applied control is minimized. Applying a running cost to minimize applied control can be a feasible method of reducing vibrations through a maneuver and is one of the tools available to designers using the optimal control approach. Note that this option is not possible using conventional control concepts.

The plots of the modal coordinate $\mathbf{q}$ illustrate an interesting phenomenon. Recall from (3.6) that the damped frequencies for each mode are $\begin{bmatrix} 0.4339 & 0.9749 & 0.7818 \end{bmatrix}$ rad/s, or $\begin{bmatrix} 0.0691 & 0.1552 & 0.1244 \end{bmatrix}$ Hz. The natural tendency for any system is to oscillate at its natural frequency [7]. The same is true for this system. In Figure 26, for example, the period of q_2 decreases over time before the last acceleration pulse is applied, eventually reaching about 6.5 seconds, or roughly 0.154 Hz.

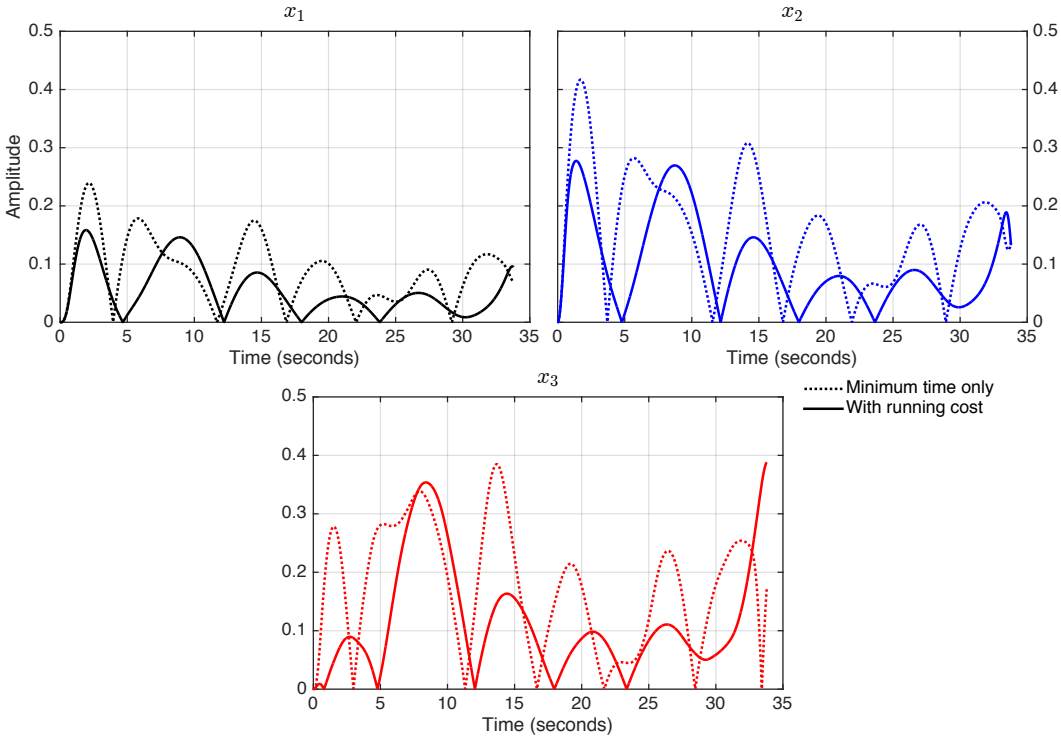

Figure 27. Comparison of flexible-body results in physical space for endpoint cost vs. endpoint plus running costs (magnitudes only).

The implementation of the spacecraft's control system also becomes apparent. The displacement of y_1 stays at or very near to zero (on a scale of 10^{-10}, see Figure 23) throughout the rigid-body simulation but its flexible-body counterpart does not. This vibrational motion is analogous to the control system counteracting the effects of the motion of the two axes to keep the spacecraft

stable in its position. As we constrain the control input, and thus reduce the applied force on y_2 and y_3, it follows that the relative magnitude of q_1 decreases since mode 1 is closely mapped to the rigid-body motion of the system (as previously discussed). By reducing the force used to slew masses 2 and 3, the spacecraft's control system does not need to work as hard to counteract the displacements of the other axes.

Due to the excitation of the flexible modes, the spacecraft and its appendages will continue to vibrate after the slew has completed (see Figure 25). Figure 25 shows the behavior of the vibrations after the final conditions are met, when $t > t_f$ and the payload (antenna) must be operated. In Figure 28, the physical properties of each mode take over as the slew control system deactivates. Modes 2 and 3 dampen quickly while mode 1 takes longer to settle.

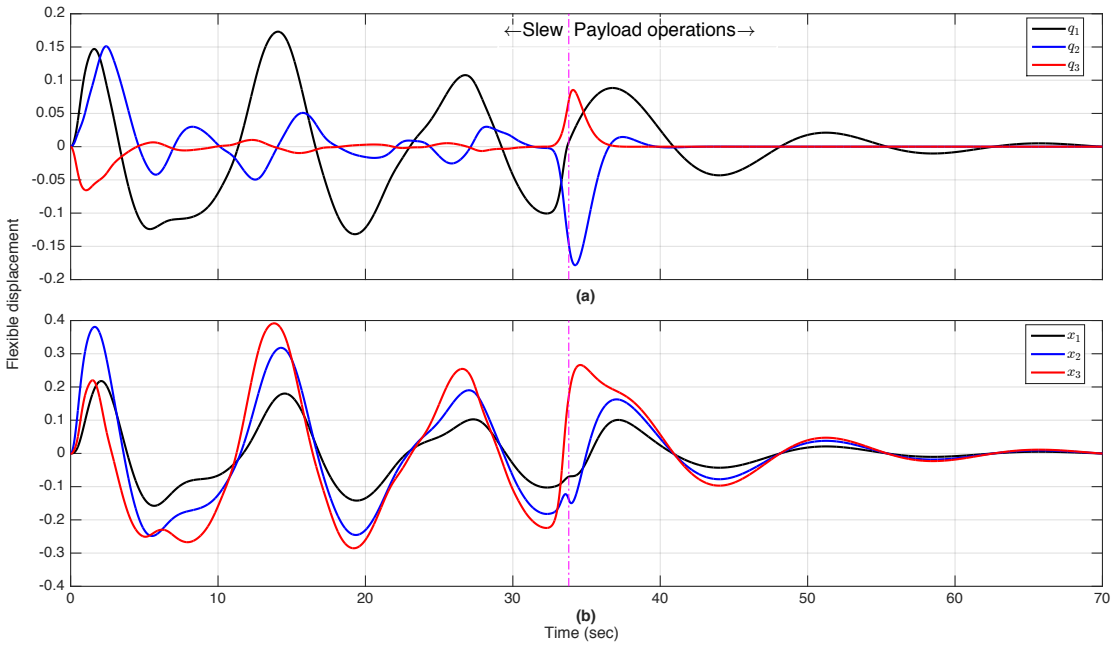

Figure 28. Flexible spillover for time-optimal slew maneuver: (a) modal coordinates; (b) physical coordinates.

Further, referring to Figure 28, as mode 1 settles, its frequency approaches its damped natural frequency. The bodies in each axis continue to physically

oscillate about equilibrium but at the same frequency (dominated by mode 1). From this result, it is apparent that performing the slew maneuver excites the base body in a way that perturbs the motion of the entire system. If the perturbation is large enough, it may be the case that the operation following the slew, (e.g., communicating over an antenna link), could be disrupted. Therefore, it is desirable to try to limit this flexible motion. This will be the subject of the sections that follow.

D. SETTING TERMINAL CONDITIONS ON THE FLEXIBLE MOTION

Suppose it is desired to extinguish all vibrations at the end of the maneuver. The appropriate terminal flex constraints added to the problem statement in (4.24) are

$$\left(q_1\left(t_f\right),q_2\left(t_f\right),q_3\left(t_f\right),q_4\left(t_f\right),q_5\left(t_f\right),q_6\left(t_f\right)\right)=(0,0,0,0,0,0)\ . \tag{4.26}$$

One would expect that more control or more time is required to cease flexible motion and meet the desired end conditions for the maneuver. The minimum-time solution is shown in Figure 29 and confirms this assertion. The maneuver now takes 35.14 seconds, an increase of 1.34 seconds (4%), as more time is required to null the vibrations. Similar behavior occurs in the elevation axis as discussed previously since the spacecraft must travel a greater distance in the azimuthal direction. Note that in Figure 29 that the trajectories are plotted at the solution nodes. They would be smoothed by the correct interpolation prior to implementation on a real system.

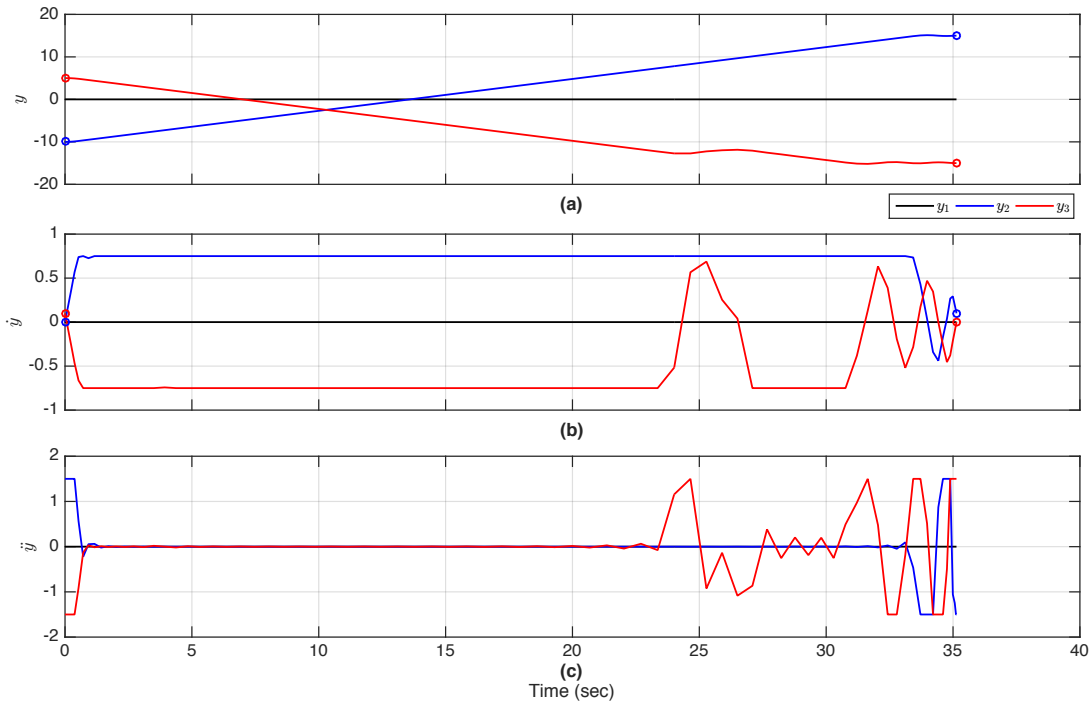

Figure 29. Optimized maneuver with zero-flex conditions at endstate $\left(t_f = 35.14\right)$: (a) position; (b) rate; (c) acceleration.

Figure 30 plots the maneuver in modal and physical coordinates. Note the impulse on all three axes at ~23 seconds; this coincides with the acceleration impulse along the elevation axis in Figure 29(c) and provides an illustrative example of how the three axes are coupled. Force is applied on only one mass, yet this induces motion on the other masses. In Figure 30(a), mode 1 again dominates the total motion.

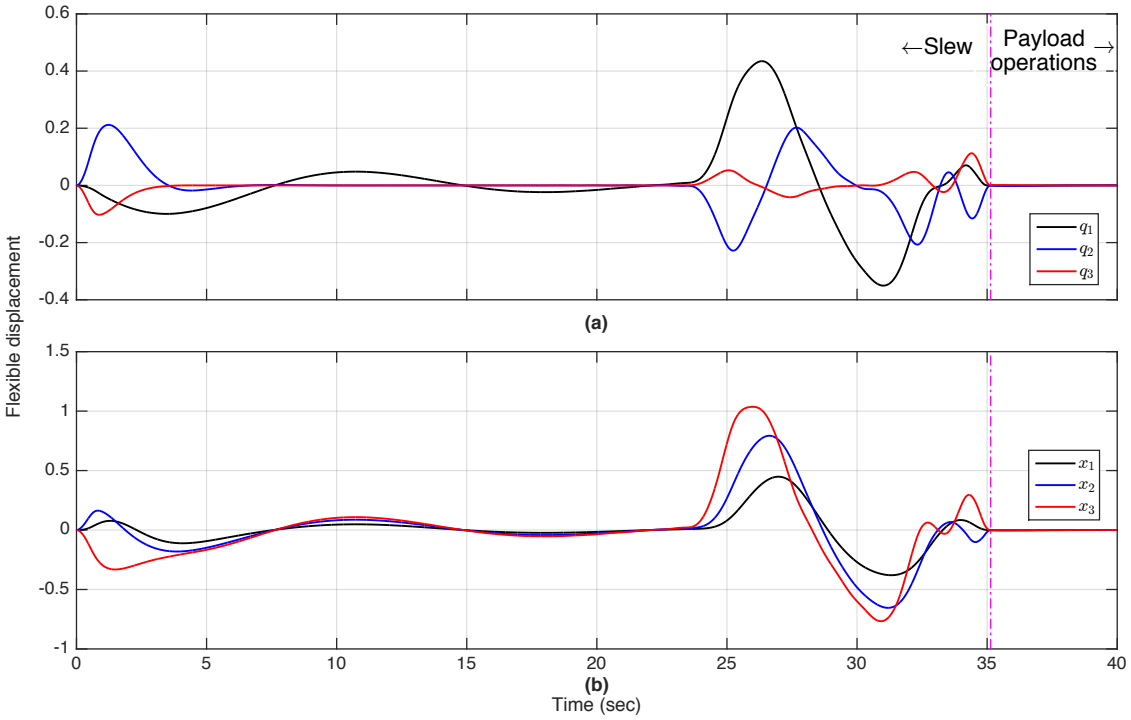

Figure 30. Flexible spillover with terminal flex constraint: (a) modal space; (b) physical space.

A running cost is now added to minimize control. Applying the cost function in (4.25), the optimized maneuver (Figure 31) takes 35.26 seconds, only marginally slower than in the previous case (0.12 seconds, 0.36%). This shows that it is possible to reshape the trajectory of the non-dominant slew axis in order to reduce the control effort. Note that the acceleration profile for the azimuth axis ($\ddot{y}_2$) is essentially the same as before. However, the reduction of the control effort on the elevation axis has an advantageous impact on the flexible effects.

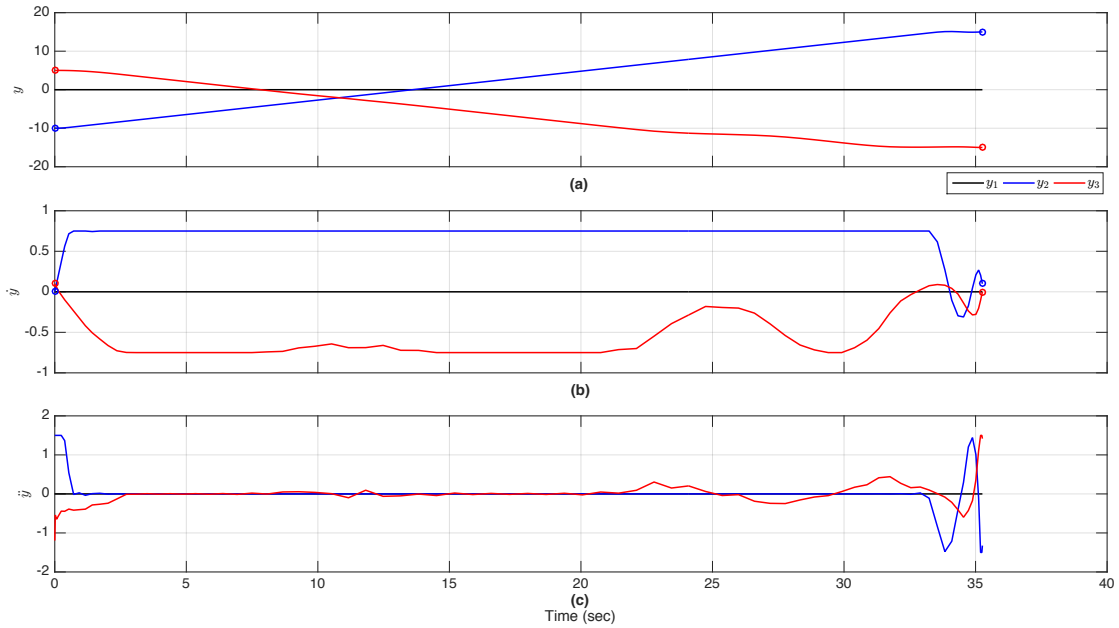

Figure 31. Maneuver optimized for time and control effort $\left(t_f = 35.26\right)$: (a) position; (b) rate; (c) acceleration.

Figure 32 illustrates the flexible components of the minimum time plus minimum effort slew. The total magnitude of flexible-body displacement has been significantly reduced. Variable x_3 alone experiences roughly a 50% decrease in peak displacement. With the negligible increase in maneuver time and decrease in control and vibrations, this maneuver proves to be more desirable from the point of view of system operation since the load on the base body controller is reduced.

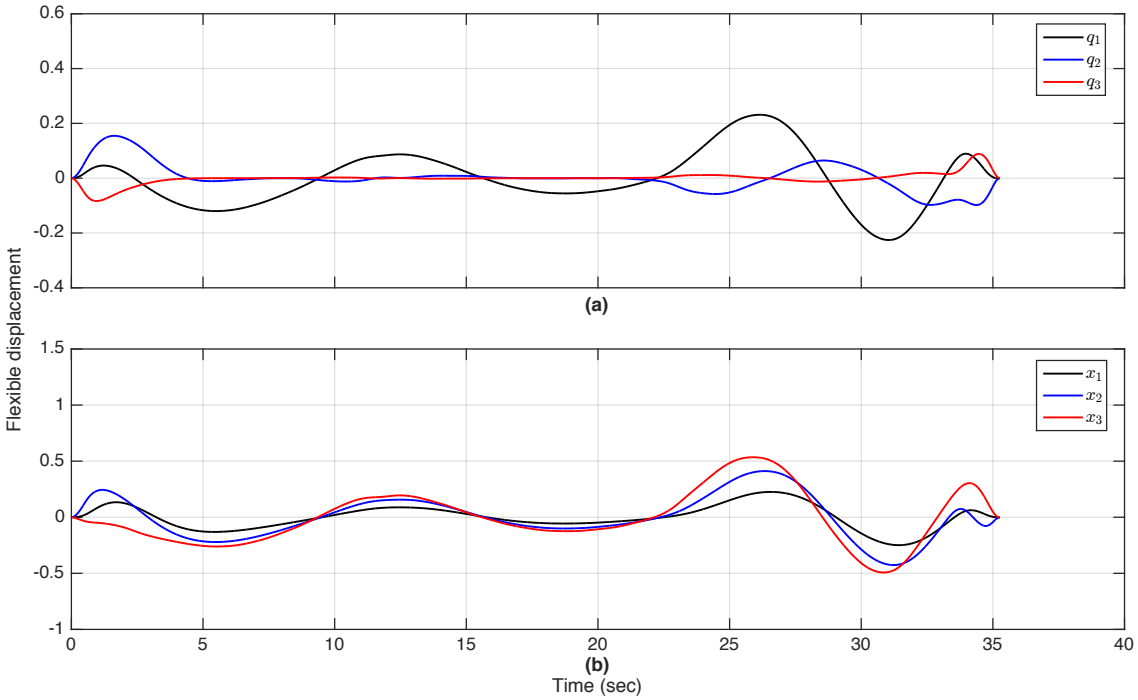

Figure 32. Flexible effects from the maneuver in Figure 31: (a) modal space; (b) physical space.

An interesting phenomenon occurs in these two maneuvers where the system uses the additional freedom in the motion of the elevation axis to meet the desired endstate while maintaining steady acceleration on the azimuth axis. The controller excites the modes of the system, by applying force only on m_3, in such a way that its modal properties work to reduce the effects of flexibility in the system. This non-intuitive aspect is only possible by using optimal control to design the maneuver trajectories.

To further illustrate the point, assume that the initial conditions are changed to

$$\left(y_1(t_0), y_2(t_0), y_3(t_0), y_4(t_0), y_5(t_0), y_6(t_0)\right) = (0, -10, 10, 0, 0, 0.1) \tag{4.27}$$

so that both axes now must move the same distance, such that $y_2(t_f) - y_2(0) = y_3(t_f) - y_3(0)$, thus removing freedom previously present in the elevation axis. The results are telling; the minimum-time maneuver (no running

cost) is 0.89 seconds (2.5%) slower (see Figure 33), and the controller must now torque both axes before the end of the maneuver in order to suppress the flexibilities. A similar effect is observed for the minimum time and effort problem (see Figure 35). The vibration profiles for each maneuver (see Figure 34 and Figure 36) are similar, further emphasizing the role a non-dominant axis can play in accommodating flexible effects.

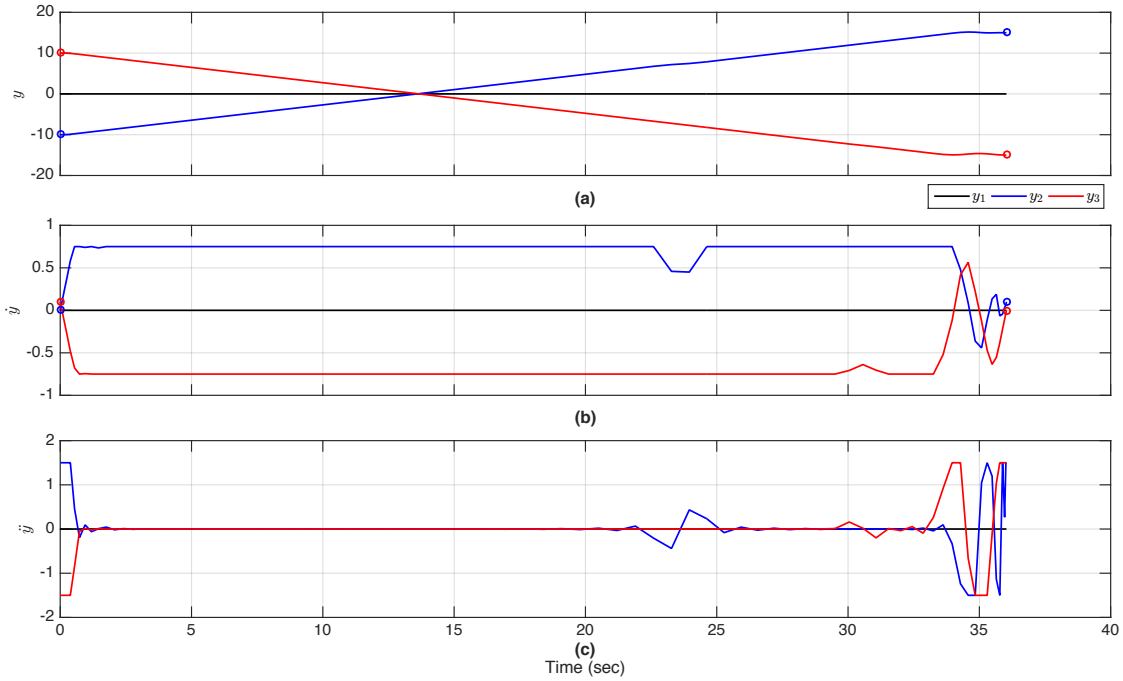

Figure 33. Minimum-time maneuver for $y_2(t_f) - y_2(0) = y_3(t_f) - y_3(0)$ $(t_f = 36.03)$: (a) position; (b) rate; (c) acceleration.

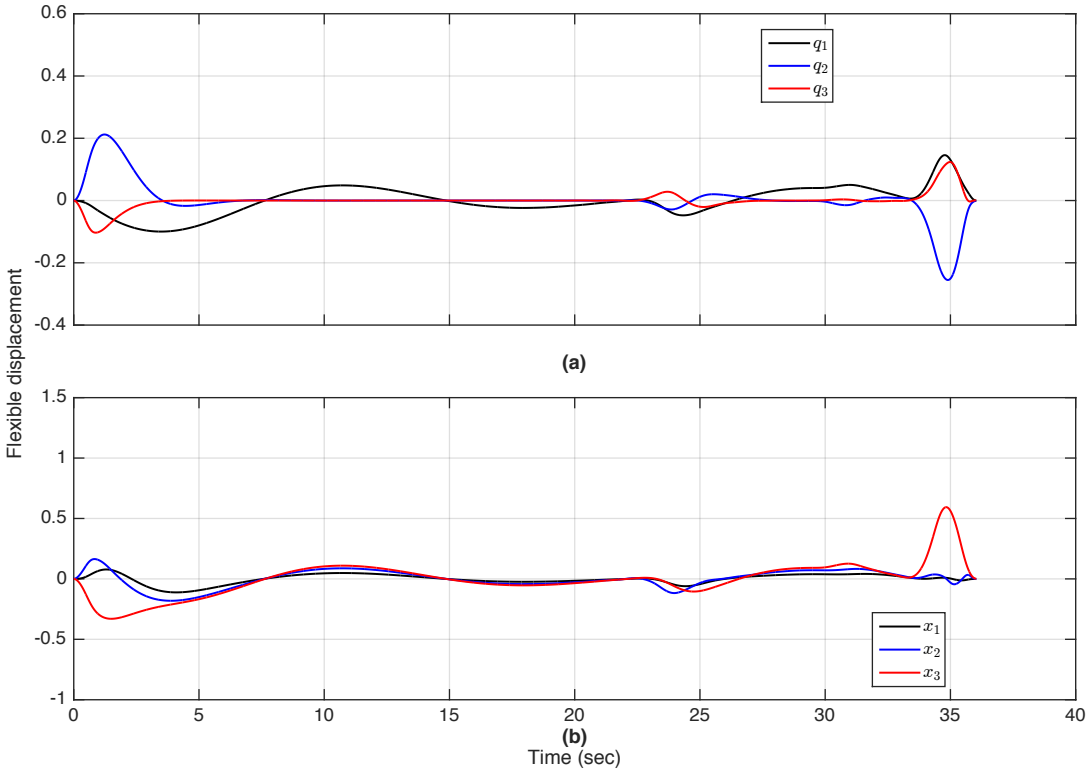

Figure 34. Flexible displacement from minimum-time maneuver of Figure 33: (a) modal space; (b) physical space.

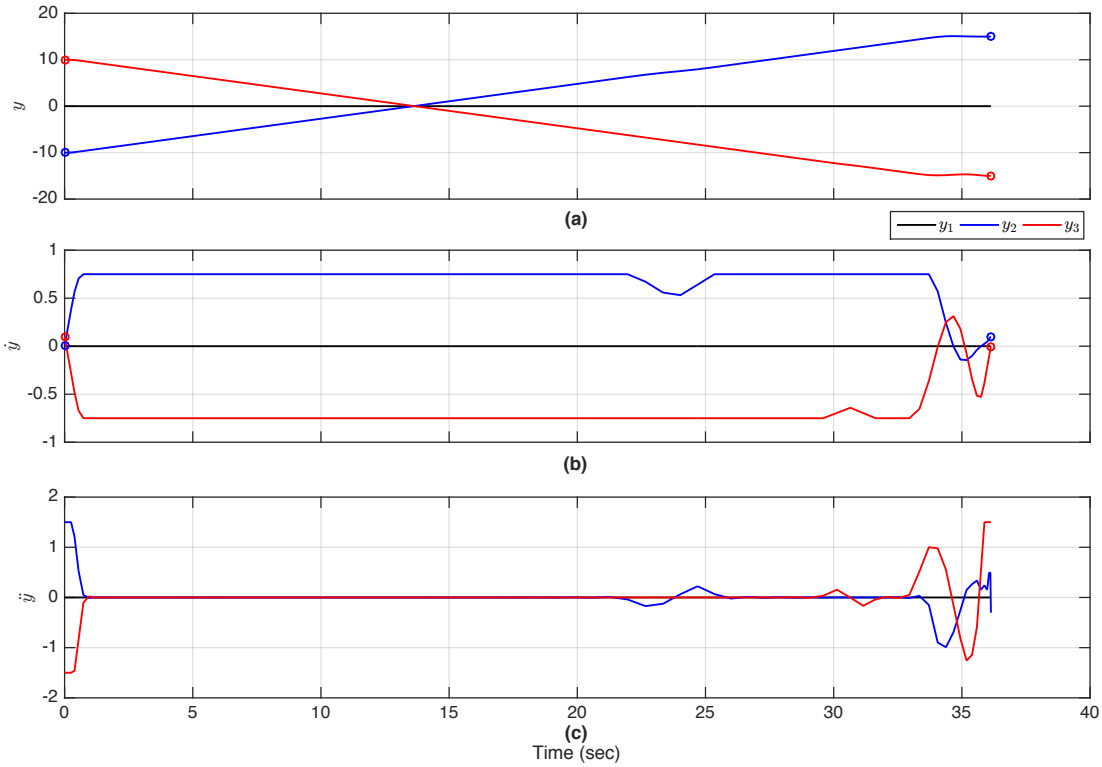

Figure 35. Maneuver optimized for time and control effort with $y_2(t_f) - y_2(0) = y_3(t_f) - y_3(0)$ $(t_f = 36.13)$: (a) position; (b) rate; (c) acceleration.

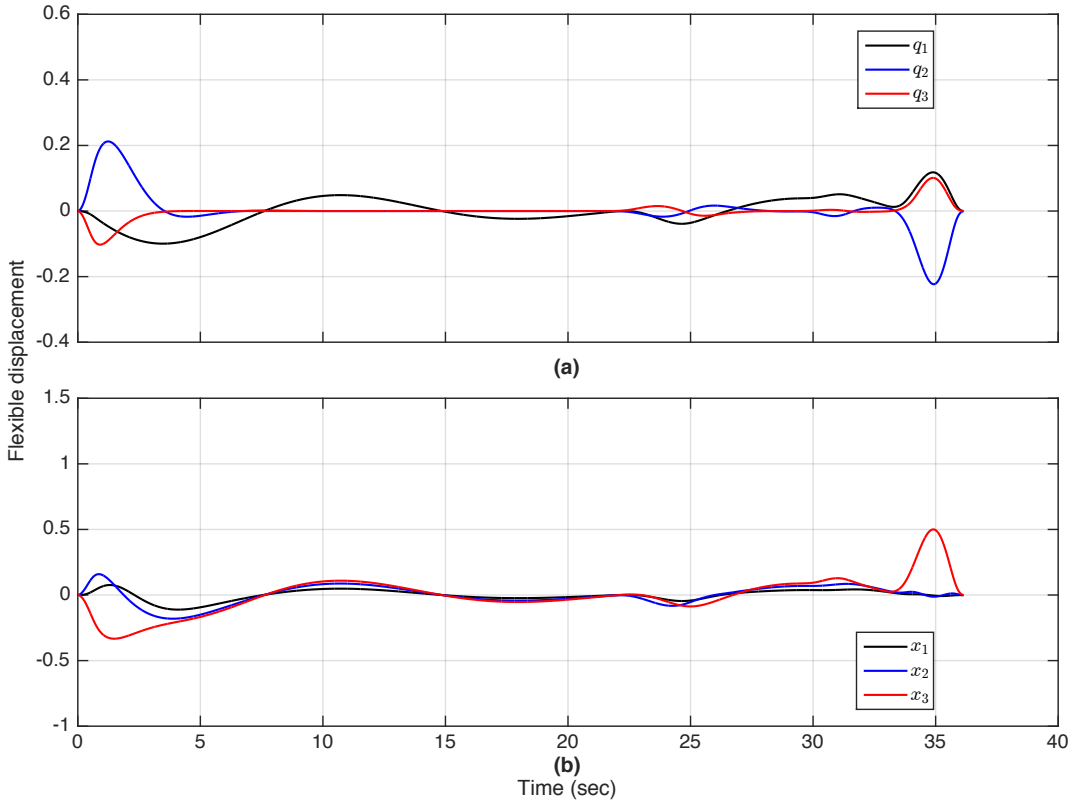

Figure 36. Flexible displacement from maneuver of Figure 35: (a) modal space; (b) physical space.

E. BOUNDS ON FLEXIBILITY DURING SLEW

A less stringent case than designing for zero spillover at the end of a maneuver is to set a bound on the flexible displacement during the maneuver. In other words, maintain flexible motion within a desired range. Perhaps a designer is willing to trade flexible effects for slew time or control effort. One cannot simply set nonzero bounds on $\mathbf{q}(t)$ and expect them to translate into the physical world. As discussed previously, the transformation $\mathbf{x} = \mathbf{V}\mathbf{q}$ must be applied. For example, suppose it is desired to bound vibrations in physical space for all axes to the interval [-0.3, 0.3] degrees with no constraint on $\dot{\mathbf{x}}$. The transformation for the upper and lower bounds yield, for the example problem of this chapter,

$$\mathbf{q}_{upper} = \begin{bmatrix} 0.1629 & 0.1048 & 0.0323 \end{bmatrix}^T \tag{4.28}$$

$$\mathbf{q}_{lower} = \begin{bmatrix} -0.1629 & -0.1048 & -0.0323 \end{bmatrix}^T . \tag{4.29}$$

However, the simple box bounds given in (4.28) and (4.29) do not properly constrain $\mathbf{q}$, resulting in potential violations of the constraint on $\mathbf{x}$ (see Figure 37).

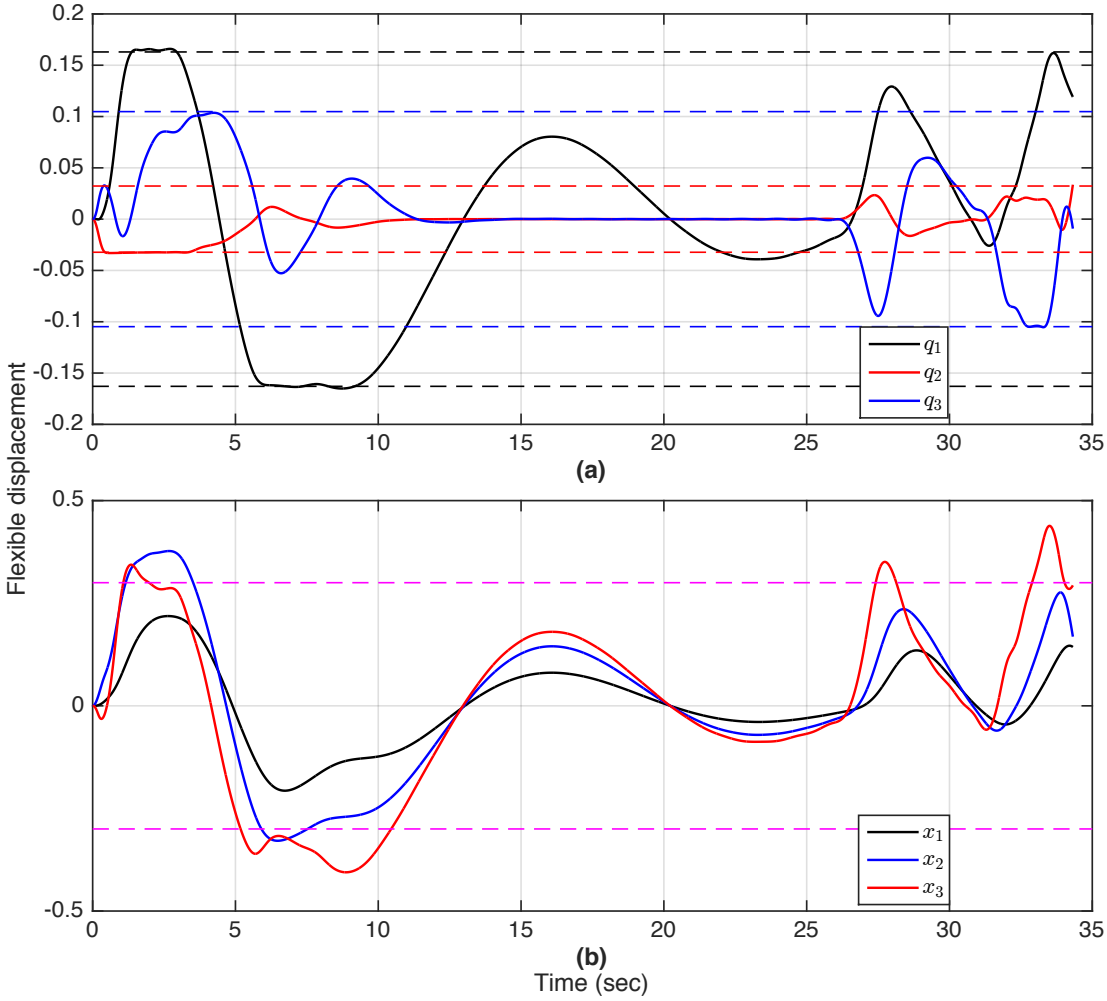

Figure 37. Flexible displacement for a slew with constraints on $\mathbf{x}$ applied via $\mathbf{x} = \mathbf{V}\mathbf{q}$: (a) modal constraints satisfied; (b) physical constraints violated.

The constraint violation in Figure 37 occurs because each modal coordinate depends on the values of all three physical coordinates (and vice-versa when transforming the other direction). For a simple explanation, consider a 2-DOF

system with eigenvector matrix $\mathbf{V} = \begin{bmatrix} a & b \\ c & d \end{bmatrix}$. A plot of the box bounds on $\mathbf{x}$ is shown in Figure 38 along with corresponding bounds on $\mathbf{q} = \mathbf{V}^{-1}\mathbf{x}$.

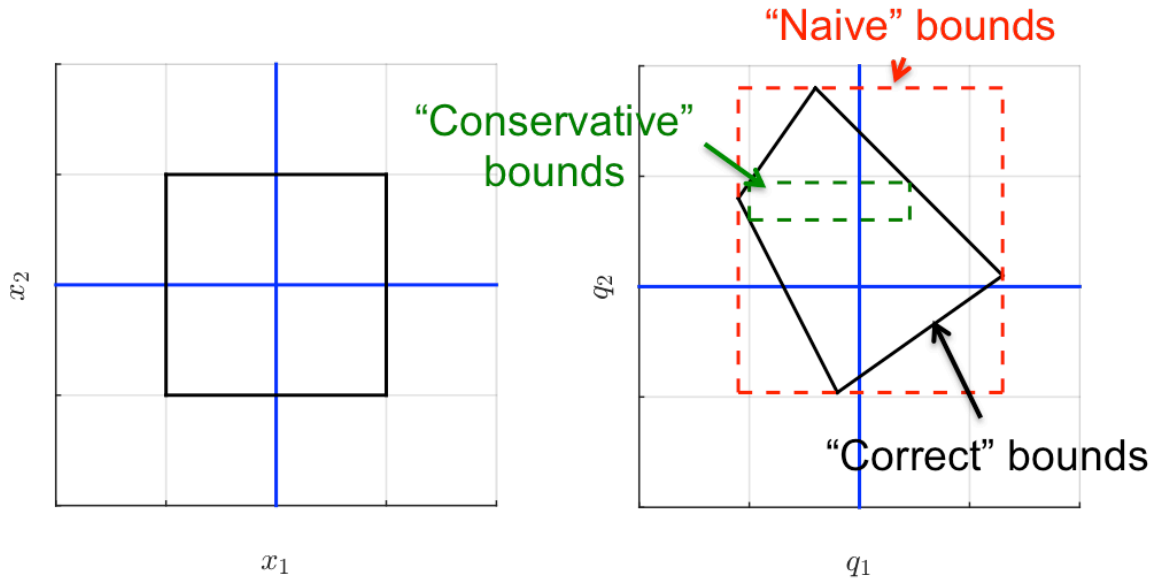

Figure 38. Example constraints on $\mathbf{x}$ transformed to $\mathbf{q}$ via $\mathbf{q} = \mathbf{V}^{-1}\mathbf{x}$.

The area in the figure outlined in solid black represents all of the values of q_1 and q_2 in modal space that satisfy the constraints in physical space. However, the transformation of the bounds on $\mathbf{x}$ directly into modal space produces the large rectangle in dashed red (naïve bounds). In this case, there are points in modal space that satisfy the constraints on $\mathbf{x}$ but not on $\mathbf{q}$. Plots of $\mathbf{q}$ transformed to $\mathbf{x}$ would show the same behavior. As seen in Figure 37, a transformation of bounds in physical space to modal space and back results in violation of the constraints.

One approach to overcome this is illustrated by the small rectangle in dashed red in Figure 38. Instead of constraining x_1 and x_2 simultaneously, perform a transformation on each individually and use the minimum absolute

values of $\mathbf{q}$ to form a conservative constraint boundary as in Figure 38. For the example 3-DOF system, the modal constraints $\left(q_{x_r}\right)$ for each axis are

$$\begin{aligned} q_{x_1} &= \mathbf{V}^{-1}\begin{bmatrix} 0.3 & 0 & 0 \end{bmatrix}^T = \begin{bmatrix} 0.0323 & 0.1629 & 0.1048 \end{bmatrix}^T \\ q_{x_2} &= \mathbf{V}^{-1}\begin{bmatrix} 0 & 0.3 & 0 \end{bmatrix}^T = \begin{bmatrix} 0.0582 & 0.0725 & -0.1307 \end{bmatrix}^T \\ q_{x_3} &= \mathbf{V}^{-1}\begin{bmatrix} 0 & 0 & 0.3 \end{bmatrix}^T = \begin{bmatrix} 0.0725 & -0.1307 & 0.0582 \end{bmatrix}^T \end{aligned} . \quad (4.30)$$

The resulting constraints on each modal coordinate are

$$\mathbf{q}_{\text{constraints}} = \pm\begin{bmatrix} 0.0323 & 0.0725 & 0.0582 \end{bmatrix}^T \quad (4.31)$$

This approach creates conservative bounds in modal space but ensures that the maneuver stays within desired bounds in the physical space. Interestingly, when optimizing the maneuver for both time and control effort, the maneuver looks similar to the ones generated using bang-off-bang control (see Figure 39). The maneuver time is 34.50 seconds. The induced vibrations (see Figure 40) are observed to ride the constraints indicating the conservatism inherent to the maneuver.

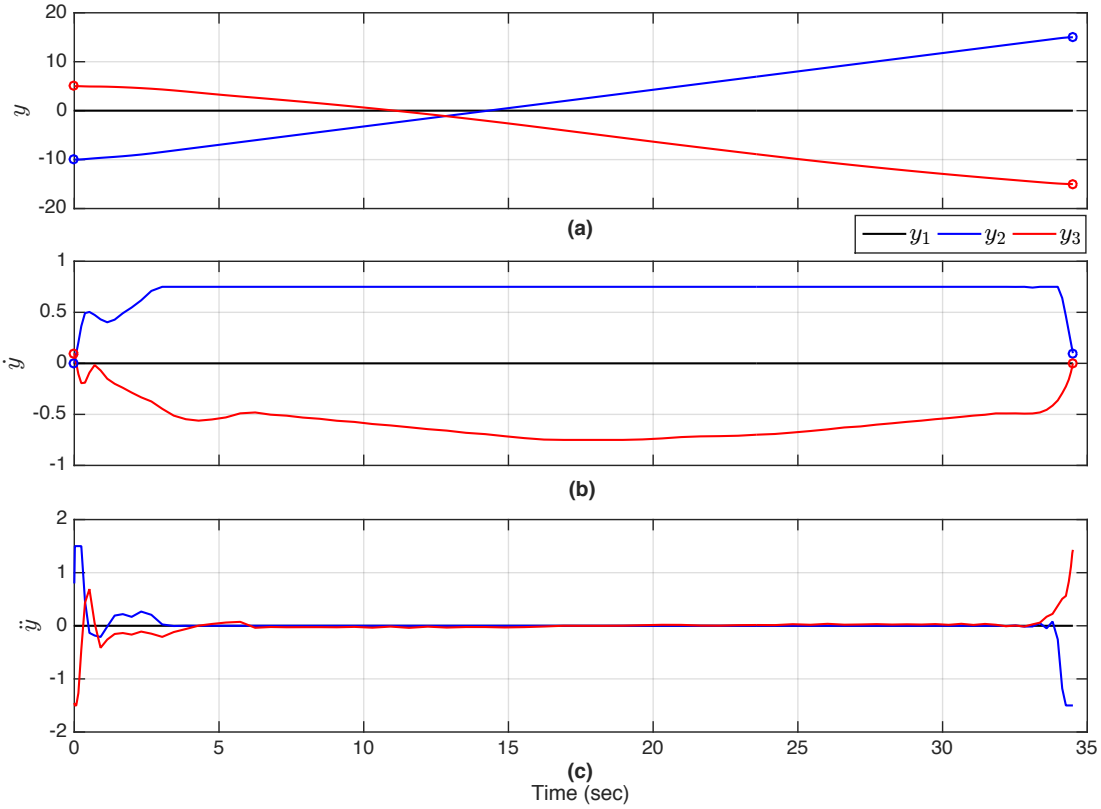

Figure 39. Maneuver optimized for time and control effort with conservative constraints on $\mathbf{q}\ \left(t_f = 34.50\right)$: (a) position; (b) rate; (c) acceleration.

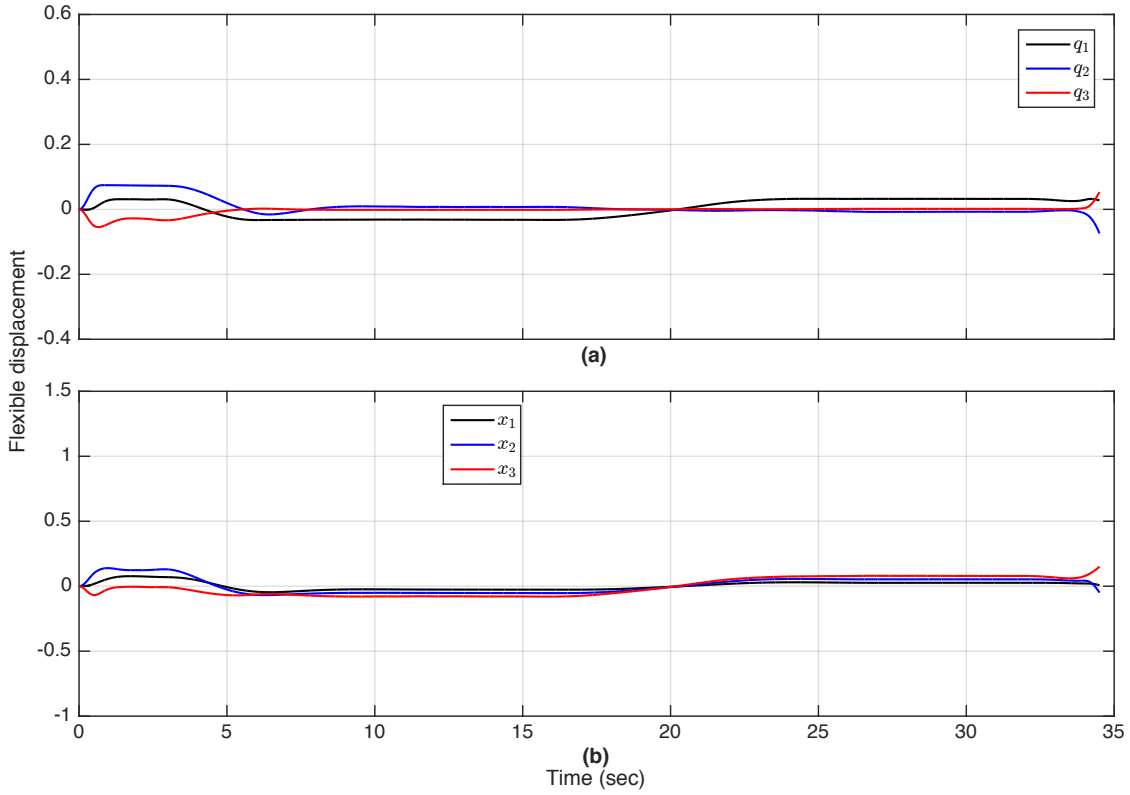

Figure 40. Flexible displacement for the maneuver of Figure 39: (a) modal space; (b) physical space.

As an alternative, a path constraint can be used to implement equations that describe the true modal constraints shown in Figure 38. In DIDO, the constraints are applied in physical space by transformation of the current modal state, as

$$\mathbf{p} = \mathbf{V}\begin{bmatrix} y_7 & y_8 & y_9 \end{bmatrix}^T . \tag{4.32}$$

Using (4.32), the constraints in physical space are applied to the transformation of the modal coordinates at each node. The optimal maneuver with the path constraints is shown in Figure 41 and Figure 42. Note that the execution time is close to that of the previous case, and additional torque must be applied to each axis at certain instants in time to avoid violating the constraint placed on the amplitude of the vibrations (compare Figure 39(c) with Figure 41(c)). Recall that

the bound in physical space vibrations is $-0.3 \le \mathbf{x} \le 0.3$; the path constraint properly enforced this bound as shown in Figure 42(b).

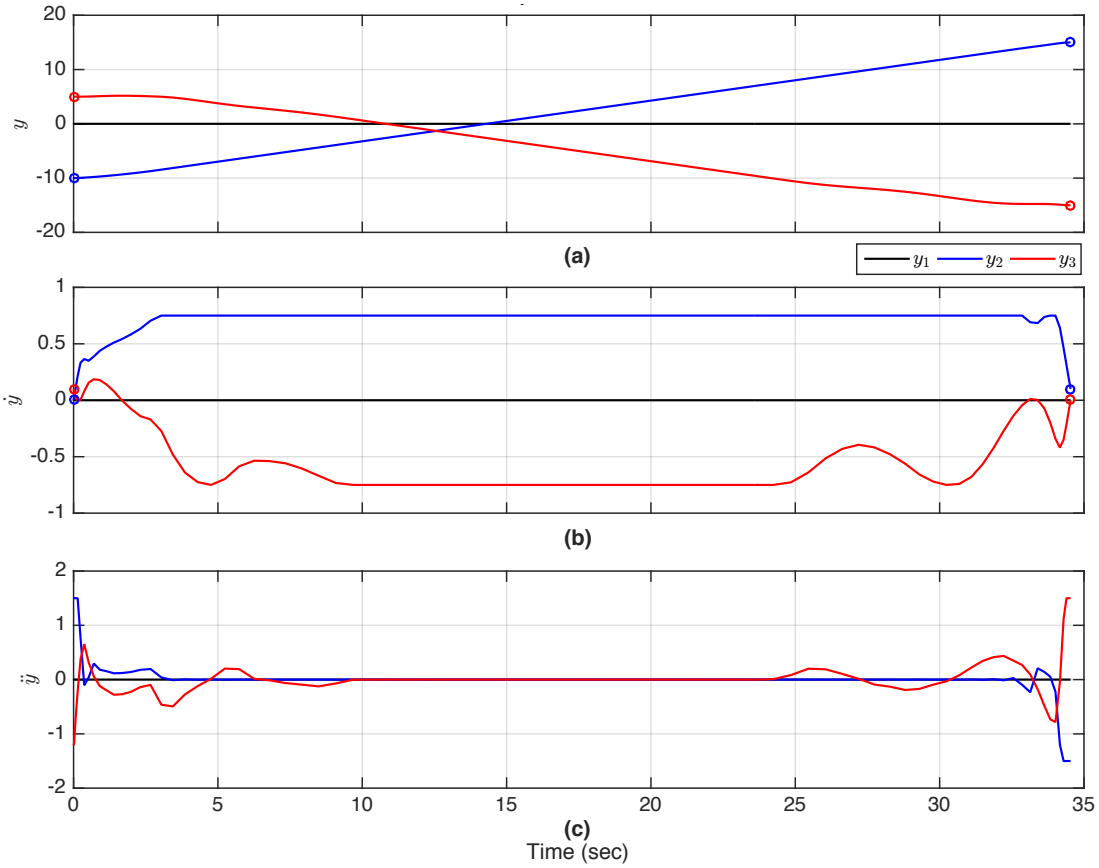

Figure 41. Maneuver optimized for time and control effort, using a path constraint to suppress vibrations $\left(t_f = 34.54\right)$: (a) position; (b) rate; (c) acceleration.

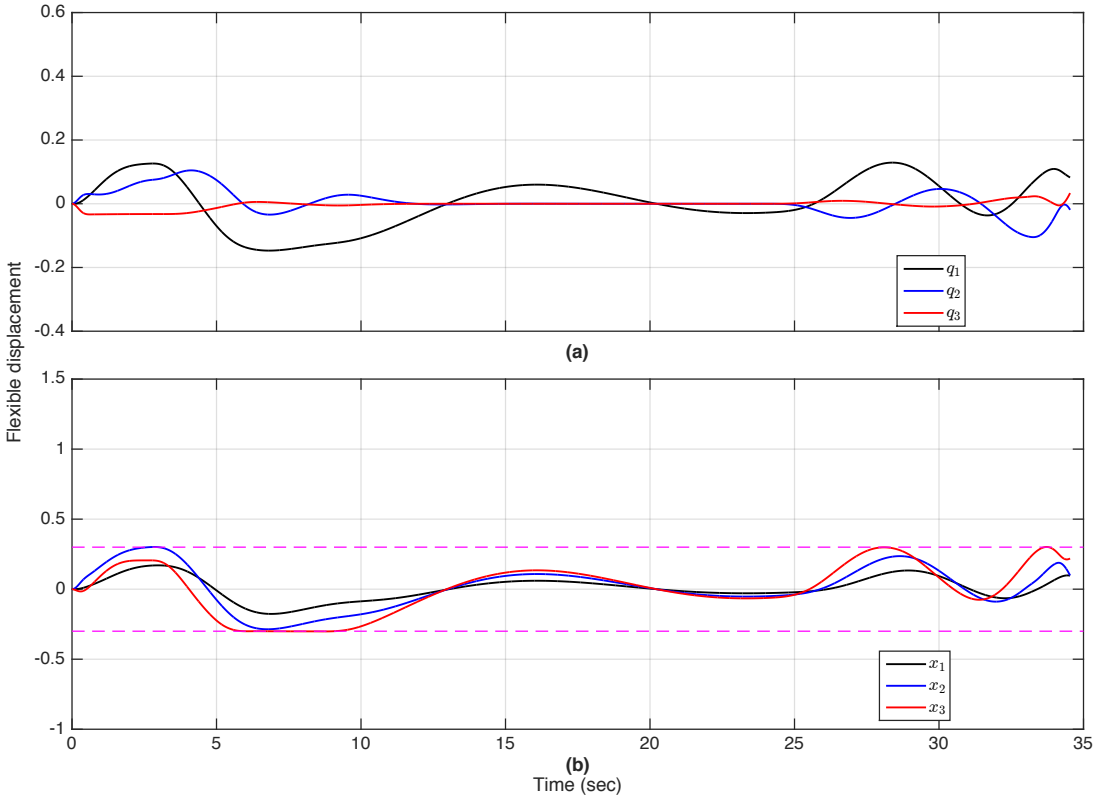

Figure 42. Flexible displacement for maneuver in Figure 41: (a) modal space; (b) physical space.

These slew maneuvers are compared to the ones from Chapter III in Table 1. Not only is it possible to constrain flexible motion, but slew times decrease when using optimal control rather than increase when using computed torque control. The table highlights the fact that optimal control provides the designer with multiple options, each reducing slew times compared to traditional control methods.

Table 1. Comparison of slew maneuvers using computed torque control and optimal control.

		Computed torque control			Optimal control			Time savings
		t_f (sec)	Max amplitude (deg)		t_f (sec)	Max amplitude (deg)		Relative to computed torque
			During slew	Spillover		During slew	Spillover	
Unconstrained flexibility		38.1	0.143	0.118	33.8	0.392	0.266	11.3%
Zero terminal flex		Cannot execute			35.14	1.04	0	7.7%
Zero terminal flex	Conservative bounds	Cannot execute			34.50	0.15	0	9.5%
	Path constraint	Cannot execute			34.54	0.30	0	9.3%

F. SUMMARY

In this chapter, the antenna slew problem was reformulated in order to apply optimal control theory to determine the control effort required to minimize slew time while simultaneously managing structural flexibility. It was shown that it is possible to apply torque in such a manner that the flexible properties of the system could be used advantageously to control vibrational effects. It was also shown that optimal control could be utilized to minimize the control effort without significantly increasing slew time or flexible motion. This effect is particularly useful in instances where one link has a greater distance to travel than the other.

This chapter additionally illustrated the value of working in modal space versus physical space. Modal space readily produces the natural properties of the system by mode and allows control system designers to understand the responses of a flexible system to force inputs. The equations of motion in modal space represent single-DOF systems that uncouple the physical space equations, making analysis and control of the system dynamics much easier.

The challenges of defining the constraints on vibrations in physical and modal spaces were discussed. The key difficulty is preserving the relationship $\mathbf{x} = \mathbf{V}\mathbf{q}$. Conservative bounds in modal space ensure that physical constraints are met, but the system must exert more effort than is required to stay within

those bounds. Naïve bounds on system behavior in modal space may cause violation of the bounds in physical space. Therefore, a path constraint that uses the relationship $\mathbf{x} = \mathbf{Vq}$ must be used to ensure the correct physical constraints are met.

The optimal control solutions presented in this chapter greatly reduced flexible effects while simultaneously decreasing slew time. While computed torque control from Chapter III required constant tweaking of the system to achieve desired results, the optimal control method allows for easy constraint definition as long as the problem is posed correctly. The optimal control approach will be applied to a more realistic antenna system in the next chapter.

THIS PAGE INTENTIONALLY LEFT BLANK

V. OPTIMAL CONTROL OF A DOUBLE-GIMBAL ANTENNA WITH FLEXIBLE JOINTS

This chapter introduces a double-gimbal mechanism (DGM) to add to the system from Chapter IV to provide a more realistic model of an actual gimbaled spacecraft antenna. The equations of motion of this system are significantly more complex than those of the simple models in previous chapters. The rotational dynamics introduce additional nonlinear terms that are dependent on the current state of the system. Building on the developments of the previous chapter, this chapter compares the results from computed torque control and optimal control of the nonlinear system. The goal of this chapter is to show that modal analysis and optimal control can be applied effectively to nonlinear systems.

A. UPDATING THE MODEL

Figure 43 shows a DGM that is now applied to the model. The antenna is attached to the spacecraft body through this two-axis gimbal.

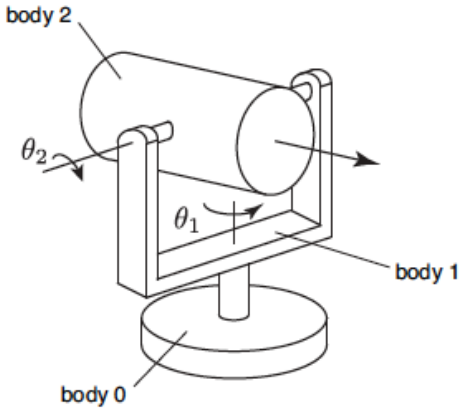

Figure 43. Diagram of two-axis gimbal (body 1 represents azimuth, body 2 represents elevation), from [5].

The equations of motion for this rigid-body system are derived in [5] as

$$\begin{bmatrix} I_{1zz} + I_{2xx}\sin^2\theta_2 + I_{2zz}\cos^2\theta_2 & 0 \\ 0 & I_{2yy} \end{bmatrix} \begin{bmatrix} \ddot{\theta}_1 \\ \ddot{\theta}_2 \end{bmatrix} = \begin{bmatrix} \tau_1 \\ \tau_2 \end{bmatrix} - \begin{bmatrix} 2\left(I_{2xx} - I_{2zz}\right)\dot{\theta}_1\dot{\theta}_2 \sin\theta_2 \cos\theta_2 \\ \left(I_{2zz} - I_{2xx}\right)\dot{\theta}_1^2 \sin\theta_2 \cos\theta_2 \end{bmatrix} . \tag{5.1}$$

In (5.1), θ_1 and θ_2 represent the angular displacement of the azimuth and elevation, respectively. This model does not account for the motion of the spacecraft body and ignores flexibility. For example, the motion of the azimuth joint coincides exactly with the appendage connected to that joint.

The model of (5.1) is now extended to include flexible effects. Figure 44 shows a schematic of a flexible joint. The spring with stiffness constant k_i represents joint flexibility and allows elastic displacement between the rotor (mounted on the spacecraft) and the rotary link. The dashpot with damping constant c_i represents the torsional damping due to rotational friction, structural properties, and external mechanisms (in other words, anything that dissipates energy during motion instead of storing it).

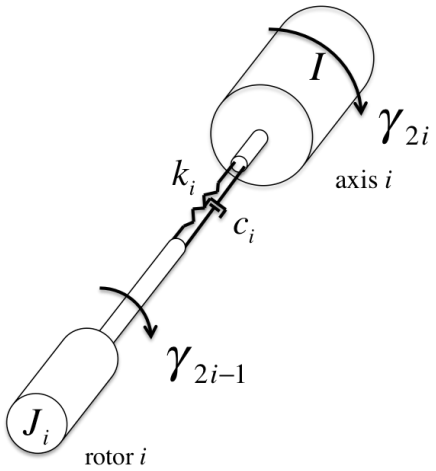

Figure 44. Representation of an elastic joint, after [14].

In Figure 44, γ_{2i} is the angular displacement of axis i, and γ_{2i-1} is the angular displacement of the actuator. These displacements are related to the link and rotor angles as

$$\begin{aligned} \gamma_{2i} &= \theta_i, i = 1,...,n \\ \gamma_{2i-1} &= -\frac{1}{G_i}\phi_i, i = 1,...,n \end{aligned} \tag{5.2}$$

where n is the number of axes in the system (in this case, $n = 2$) and G_i is the gear ratio of the actuator. For the purposes of this model, it is assumed that the system consists of a direct drive between the actuator and shaft, so there are no gears between the actuator and rotor. As a result, from (5.2), $\gamma_{2i-1} = \phi_i$. The elastic displacement in the joint, therefore, is $\gamma_{2i} - \gamma_{2i-1}$.

Let $k_i = k$, $c_i = c$, $\mathbf{y}_1 = \begin{bmatrix} \gamma_2 & \gamma_4 \end{bmatrix}^T = \begin{bmatrix} \theta_1 & \theta_2 \end{bmatrix}^T$, and $\mathbf{y}_2 = \begin{bmatrix} \gamma_1 & \gamma_3 \end{bmatrix}^T = \begin{bmatrix} \phi_1 & \phi_2 \end{bmatrix}^T$. The inertia tensor of the rotor is given as $\left(\mathbf{I}_{rotor}\right)_i = \mathrm{diag}\begin{bmatrix} I_{ixx} & I_{iyy} & I_{izz} \end{bmatrix}$, and $D(\mathbf{y}_1)$ gives the configuration-dependent inertia of the rigid-body. Using these definitions, the kinetic energy for the system may be computed as

$$KE = \frac{1}{2}\dot{\mathbf{y}}_1^T D(\mathbf{y}_1)\dot{\mathbf{y}}_1 + \frac{1}{2}\dot{\mathbf{y}}_2^T \mathbf{J}_{rotor}\dot{\mathbf{y}}_2 \tag{5.3}$$

where moment of inertia $\mathbf{J}_{rotor} = \mathrm{diag}\begin{bmatrix} G_1^2\left(I_{rotor}\right)_{1zz} & \cdots & G_n^2\left(I_{rotor}\right)_{nzz} \end{bmatrix}$ [14]. The potential energy, a function of the angular displacements of the axes and the elastic displacement, is

$$PE = P_1(\mathbf{y}_1) + P_2(\mathbf{y}_1 - \mathbf{y}_2) \tag{5.4}$$

where function P_1 is the potential energy of the rigid-body system. Function P_2 depends on the elastic displacement and is defined by

$$P_2 = \frac{1}{2} k \left(\mathbf{y}_1 - \mathbf{y}_2 \right)^T \left(\mathbf{y}_1 - \mathbf{y}_2 \right) \ . \tag{5.5}$$

The Lagrangian may be constructed as

$$L = KE - PE = \frac{1}{2} \left(\dot{\mathbf{y}}_1^T D\left(\mathbf{y}_1 \right) \dot{\mathbf{y}}_1 + \dot{\mathbf{y}}_2^T \mathbf{J}_{rotor} \dot{\mathbf{y}}_2 - 2P_1\left(\mathbf{y}_1 \right) - k \left(\mathbf{y}_1 - \mathbf{y}_2 \right)^T \left(\mathbf{y}_1 - \mathbf{y}_2 \right) \right) \tag{5.6}$$

Damping results in energy dissipation rather than energy storage. A typical model of this is Rayleigh dissipation given as [15]

$$E_{dis} = \frac{1}{2} c \left(\dot{\mathbf{y}}_1 - \dot{\mathbf{y}}_2 \right)^2 \tag{5.7}$$

In the Lagrangian of (5.6), dissipation may be added to the total energy, and thus the Euler-Lagrange equation becomes

$$\frac{d}{dt} \left(\frac{\partial L}{\partial \dot{\mathbf{y}}_i} \right) - \frac{\partial L}{\partial \mathbf{y}_i} + \frac{\partial E_{dis}}{\partial \dot{\mathbf{y}}_i} = 0 \ . \tag{5.8}$$

The generic equations of motion may now be derived from (5.8) as

$$D \ddot{\mathbf{y}}_1 + \left(\dot{D} \dot{\mathbf{y}}_1 - \frac{1}{2} \dot{\mathbf{y}}_1^T \frac{\partial D}{\partial \mathbf{y}_1} \dot{\mathbf{y}}_1 + \frac{\partial P_1}{\partial \mathbf{y}_1} \right) + c \left(\dot{\mathbf{y}}_1 - \dot{\mathbf{y}}_2 \right) + k \left(\mathbf{y}_1 - \mathbf{y}_2 \right) = \mathbf{0} \tag{5.9}$$

$$\mathbf{J}_{rotor} \ddot{\mathbf{y}}_2 - c \left(\dot{\mathbf{y}}_1 - \dot{\mathbf{y}}_2 \right) - k \left(\mathbf{y}_1 - \mathbf{y}_2 \right) = \mathbf{u} \ . \tag{5.10}$$

Equation (5.9) governs the motion of the rigid links, while (5.10) governs the motion of the rotors. The second term of (5.9) in parentheses represents the Coriolis, gravitational, and centripetal forces acting on the system. The new control vector $\mathbf{u} = \begin{bmatrix} \tau_1 & \tau_2 \end{bmatrix}^T$ now acts on (5.10); its effects are felt in (5.9) via transmission through the flexible joint.

The new equations for the flexible DGM are thus

$$\begin{bmatrix} I_{1zz} + I_{2xx}\sin^2\theta_2 + I_{2zz}\cos^2\theta_2 & 0 \\ 0 & I_{2yy} \end{bmatrix}\begin{bmatrix} \ddot{\theta}_1 \\ \ddot{\theta}_2 \end{bmatrix} + \begin{bmatrix} 2\left(I_{2xx} - I_{2zz}\right)\dot{\theta}_1\dot{\theta}_2\sin\theta_2\cos\theta_2 \\ \left(I_{2zz} - I_{2xx}\right)\dot{\theta}_1^2\sin\theta_2\cos\theta_2 \end{bmatrix} + c\begin{bmatrix} \dot{\theta}_1 - \dot{\phi}_1 \\ \dot{\theta}_2 - \dot{\phi}_2 \end{bmatrix} + k\begin{bmatrix} \theta_1 - \phi_1 \\ \theta_2 - \phi_2 \end{bmatrix} = \begin{bmatrix} 0 \\ 0 \end{bmatrix} \tag{5.11}$$

$$\begin{bmatrix} \left(I_{rotor}\right)_{1zz} & 0 \\ 0 & \left(I_{rotor}\right)_{2zz} \end{bmatrix}\begin{bmatrix} \ddot{\phi}_1 \\ \ddot{\phi}_2 \end{bmatrix} - c\begin{bmatrix} \dot{\theta}_1 - \dot{\phi}_1 \\ \dot{\theta}_2 - \dot{\phi}_2 \end{bmatrix} - k\begin{bmatrix} \theta_1 - \phi_1 \\ \theta_2 - \phi_2 \end{bmatrix} = \begin{bmatrix} \tau_1 \\ \tau_2 \end{bmatrix}, \tag{5.12}$$

where the link torques in (5.1) are replaced by the torque transmitted via terms $-c\left(\dot{\theta}_1 - \dot{\phi}_1\right) - k\left(\theta_1 - \phi_1\right)$ and $-c\left(\dot{\theta}_2 - \dot{\phi}_2\right) - k\left(\theta_2 - \phi_2\right)$.

B. SIMULATION OF THE COUPLED MOTION

Following from the example from [5], let $I_1 = \text{diag}\begin{bmatrix} 4 & 4 & 6 \end{bmatrix}$, $I_2 = \text{diag}\begin{bmatrix} 2 & 2 & 4 \end{bmatrix}$, $\left(I_{rotor}\right)_i = \text{diag}\begin{bmatrix} 1 & 1 & 1 \end{bmatrix}$, and $c = k = 1$ with appropriate units. The equations of motion may thus be rewritten as

$$\begin{bmatrix} 6 + 2\sin^2\theta_2 + 4\cos^2\theta_2 & 0 \\ 0 & 2 \end{bmatrix}\begin{bmatrix} \ddot{\theta}_1 \\ \ddot{\theta}_2 \end{bmatrix} + \begin{bmatrix} -4\dot{\theta}_1\dot{\theta}_2\sin\theta_2\cos\theta_2 \\ 2\dot{\theta}_1^2\sin\theta_2\cos\theta_2 \end{bmatrix} + \begin{bmatrix} \dot{\theta}_1 - \dot{\phi}_1 \\ \dot{\theta}_2 - \dot{\phi}_2 \end{bmatrix} + \begin{bmatrix} \theta_1 - \phi_1 \\ \theta_2 - \phi_2 \end{bmatrix} = \begin{bmatrix} 0 \\ 0 \end{bmatrix} \tag{5.13}$$

$$\begin{bmatrix} 1 & 0 \\ 0 & 1 \end{bmatrix}\begin{bmatrix} \ddot{\phi}_1 \\ \ddot{\phi}_2 \end{bmatrix} - \begin{bmatrix} \dot{\theta}_1 - \dot{\phi}_1 \\ \dot{\theta}_2 - \dot{\phi}_2 \end{bmatrix} - \begin{bmatrix} \theta_1 - \phi_1 \\ \theta_2 - \phi_2 \end{bmatrix} = \begin{bmatrix} \tau_1 \\ \tau_2 \end{bmatrix}. \tag{5.14}$$

A simple PD controller with closed loop feedback was used to simulate a conventional slew of the flexible system. The following control law was used.

$$\tau = K_p\left(\theta_d - \theta\right) + K_d\left(\omega_d - \omega\right) \tag{5.15}$$

where θ_d and ω_d are the desired angular displacements and angular rates for each axis. Given a natural frequency $\omega_n = 0.6$ rad/s and damping ratio $\zeta = 1$ to prevent overshoot, the gains may be computed in real-time as the inertia changes for the system (this is a version of computed torque control).

$$\begin{aligned} K_p &= \omega_n^2 \begin{bmatrix} I_{1zz} + I_{2xx}\sin^2\theta_2 + I_{2zz}\cos^2\theta_2 \\ I_{2yy} \end{bmatrix} \\ K_d &= 2\zeta\omega_n \begin{bmatrix} I_{1zz} + I_{2xx}\sin^2\theta_2 + I_{2zz}\cos^2\theta_2 \\ I_{2yy} \end{bmatrix} \end{aligned} . \tag{5.16}$$

The slew was implemented with the following boundary conditions and constraints:

$$\begin{aligned} \left(\theta_1(t_0), \theta_2(t_0), \omega_1(t_0), \omega_2(t_0)\right) &= (40°, 20°, 0, 0) \\ \left(\theta_1(t_f), \theta_2(t_f), \omega_1(t_f), \omega_2(t_f)\right) &= (0, 40°, 0, 0) \\ (t_0, t_f) &= (0, 20)\text{s} \end{aligned} . \tag{5.17}$$

The damping and stiffness values affect how much (or little) actuation (control torque) is needed to slew each axis to the correct position. If the stiffness value $k \to \infty$, then the elastic displacement $\theta_i - \phi_i \to 0$. The joint now behaves as a rigid body. A slew for the rigid-body system is shown in Figure 45. Note the similarities in the torque profiles for the azimuth axis for this system and the rigid-body systems studied earlier in Chapter III. More effort is required to control the azimuth axis versus the elevation axis because of the time-dependent nonlinear inertia terms.

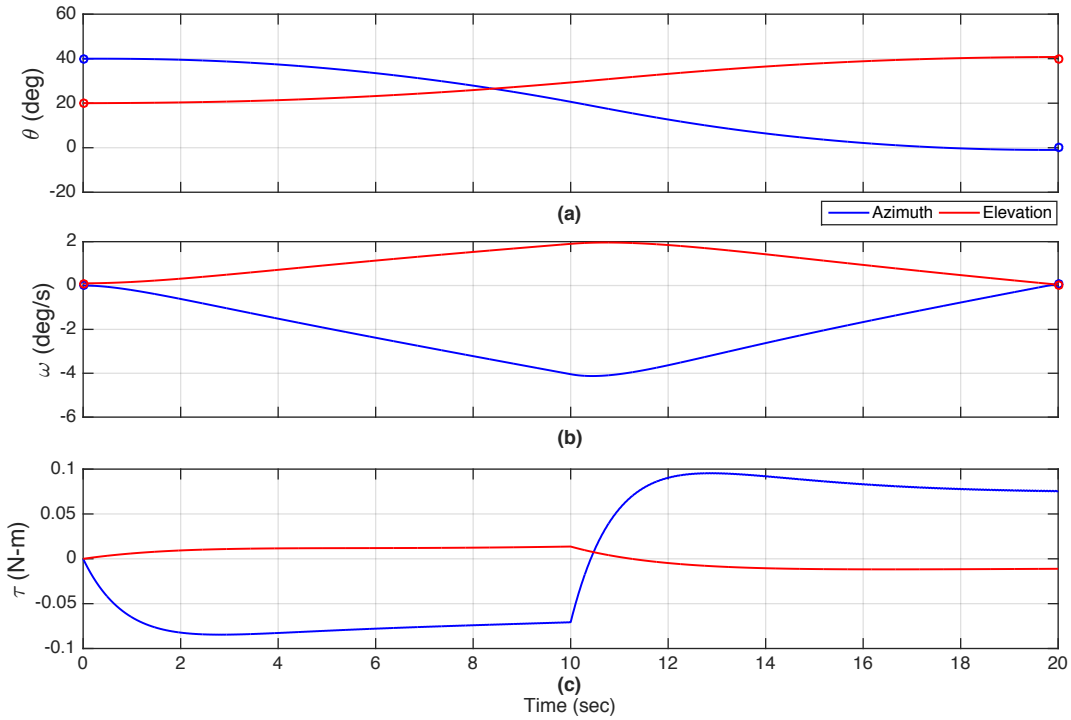

Figure 45. Computed torque control of flexible DGM with $k \gg 0$: (a) angular displacement; (b) angular rates; (c) control torques.

Figure 46 shows the angular displacements and rates of each axis and the torques applied to the rotors for $k = 1$, a much more flexible system. The inertia term for the azimuth axis changes as the elevation angle changes, affecting the gains and torques needed to control the system. Note how the controller responds to the changing inertia in the azimuth axis (see Figure 46(c)). As noted previously, it takes much more effort to control the azimuth axis than the elevation axis, but the torque profiles follow the same basic shapes as in Figure 45. Due to the elasticity in the system, the controller must continue to work even after t_f in order to damp out the vibrational effects. The large flexible displacements after the slew (post-maneuver spillover) could present a problem for antenna operations.

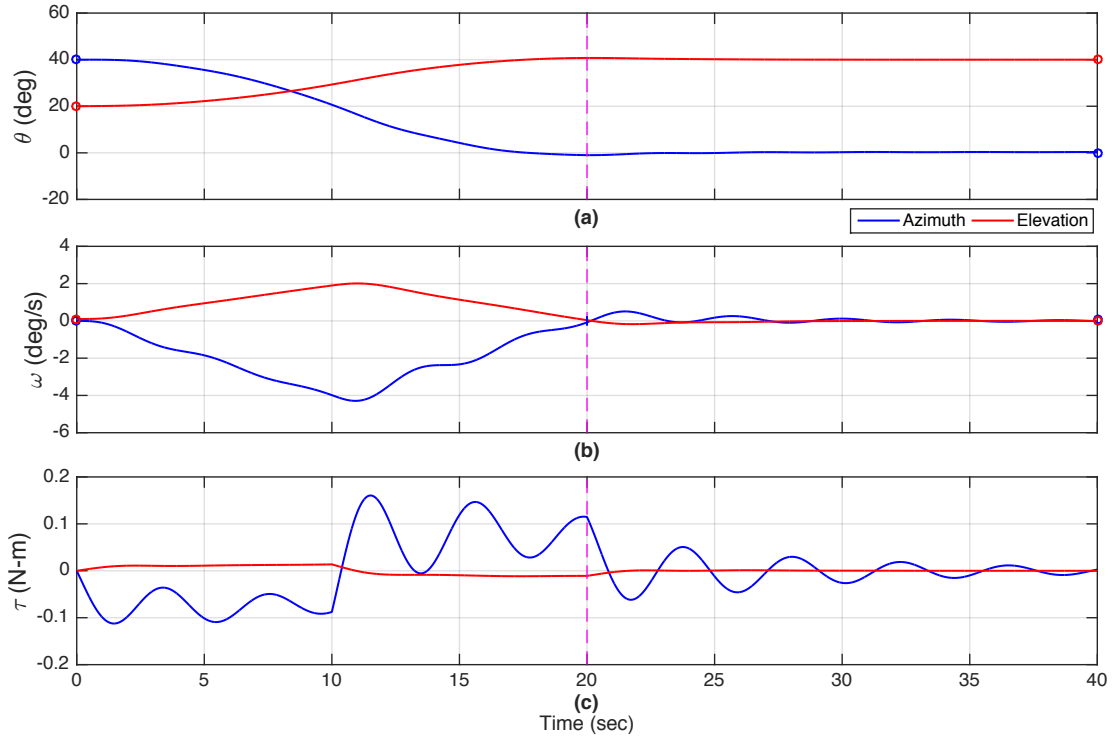

Figure 46. Computed torque control of flexible DGM with $k = 1$: (a) angular displacement; (b) angular rates; (c) control torques.

Figure 47 illustrates the relationship between the axis angle θ and the rotor angle ϕ. The elasticity in the joint causes the axis to lag the rotor as the actuator torques the rotor. The rotor must displace a certain amount before the axis follows suit. As stiffness increases, the time histories of each angle approach the same values as the lag decreases.

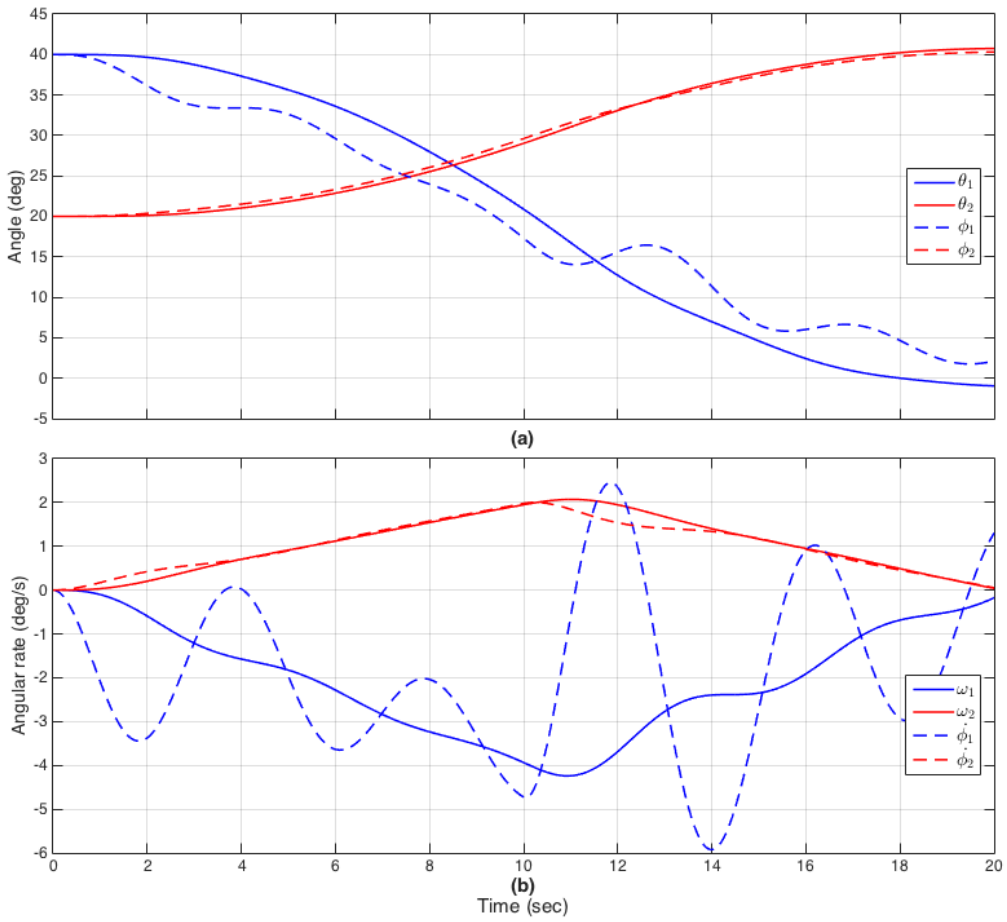

Figure 47. Time history of rotor, ϕ, and link, θ, motion for a conventional slew with $k=1$: (a) angular displacements; (b) angular rates.

Note that in using (5.15) it is assumed that the actual position of the gimbal links can be measured. An alternate control law could be implemented if the positions must be inferred at the rotor. In this case, the torque law would be

$$\tau = K_p\left(\theta_d - \phi\right) + K_d\left(\omega_d - \dot{\phi}\right) \ . \tag{5.18}$$

Due to the elasticity and coupling in the system, the slew maneuver using (5.18) takes significantly more time to reach end state (see Figure 48). Figure 48 highlights one of the challenges of feedback control of flexible systems: it makes a difference where measurements are taken.

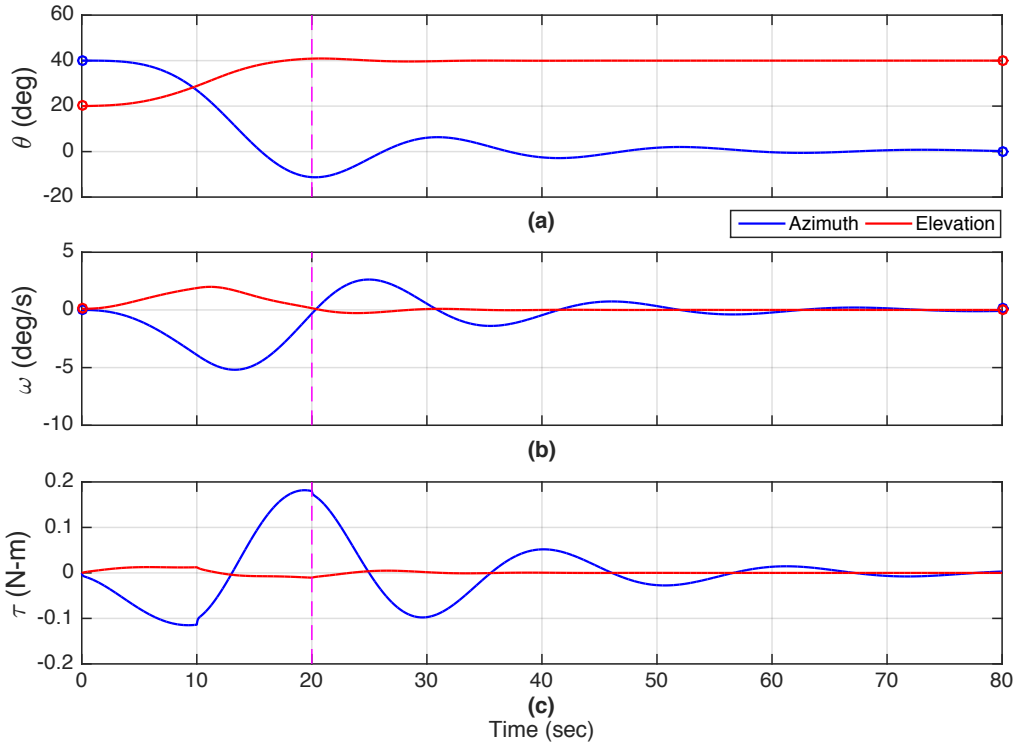

Figure 48. Computed torque control of a flexible DGM using control law (5.18): (a) angular displacement; (b) angular rates; (c) control torques.

C. OPTIMIZING THE MANEUVER

Because the flexible DGM system contains nonlinear terms, the state-space representation of the equations of motion takes on a different form. Nonetheless, these new dynamics can be used to build an optimal control problem to reduce the slew time. From (5.13) and (5.14), the state vector can be assembled as $\mathbf{y} = \begin{bmatrix} \theta_1 & \theta_2 & \omega_1 & \omega_2 & \phi_1 & \phi_2 & \dot{\phi}_1 & \dot{\phi}_2 \end{bmatrix}^T$, with rotor control vector $\mathbf{u} = \begin{bmatrix} \tau_1 & \tau_2 \end{bmatrix}^T$. For a minimum-time slew, the resulting optimal control problem is

$$
\begin{aligned}
&\text{Minimize} && J = t_f \\
&\text{Subject to} && \dot{y}_1 = y_3 \\
& && \dot{y}_2 = y_4 \\
& && \dot{y}_3 = \frac{4y_3y_4 \sin y_2 \cos y_2 - y_3 + y_7 - y_1 + y_5}{6 + 2\sin^2 y_2 + 4\cos^2 y_2} \\
& && \dot{y}_4 = \frac{-2y_3^2 \sin y_2 \cos y_2 - y_4 + y_8 - y_2 + y_6}{2} \\
& && \dot{y}_5 = y_7 \\
& && \dot{y}_6 = y_8 \\
& && \dot{y}_7 = \tau_1 + y_3 - y_7 + y_1 - y_5 \\
& && \dot{y}_8 = \tau_2 + y_4 - y_8 + y_2 - y_6 \\
& && \left(y_1(t_0), y_2(t_0), y_3(t_0), y_4(t_0)\right) = (40°, 20°, 0, 0) \\
& && \left(y_5(t_0), y_6(t_0), y_7(t_0), y_8(t_0)\right) = (40°, 20°, 0, 0) \\
& && \left(y_1(t_f), y_2(t_f), y_3(t_f), y_4(t_f)\right) = (0, 40°, 0, 0) \\
& && \left(y_5(t_f), y_6(t_f), y_7(t_f), y_8(t_f)\right) = (0, 40°, 0, 0) \\
& && |y_i| \le 1 \,\text{rad/s}, \; i = 3,4 \\
& && |u_i| \le 1.5 \text{ N-m}, \; i = 1,2
\end{aligned}
\qquad . \qquad (5.19)
$$

The challenge in working with these dynamics, given in physical space, is that the motion is highly coupled, so it is difficult to constrain the flexible effects. To do this correctly, the dynamics should be given in modal space. However, we cannot develop the modal model of this system in its current form due to the presence of the nonlinear terms. Through arithmetic manipulation, it is possible, however, to treat the nonlinear terms as a fictitious torque input,

$$
\tilde{\tau} = \begin{bmatrix} \tilde{\tau}_1 \\ \tilde{\tau}_2 \end{bmatrix} = \begin{bmatrix} 4y_3y_4 \sin y_2 \cos y_2 - 2z_5 \sin^2 y_2 - 4z_5 \cos^2 y_2 \\ -2y_3^2 \sin y_2 \cos y_2 \end{bmatrix} \qquad (5.20)
$$

This step uncouples the motion of θ_1 and θ_2 and provides a linear system of the familiar form

$$
\begin{aligned}
\mathbf{M}_1\ddot{\theta} + \mathbf{C}\left(\dot{\theta} - \dot{\phi}\right) + \mathbf{K}(\theta - \phi) &= \tilde{\tau} \\
\mathbf{M}_2\ddot{\phi} - \mathbf{C}\left(\dot{\theta} - \dot{\phi}\right) - \mathbf{K}(\theta - \phi) &= \tau
\end{aligned}
\qquad (5.21)
$$

Using (5.21), modal analysis can now be easily performed.

Modal analysis of the unforced system produces the following symmetric FRF matrix:

$$\mathbf{H}(s)=\begin{bmatrix} \frac{s^2+s+1}{6s^4+7s^3+7s^2} & 0 & \frac{s+1}{6s^4+7s^3+7s^2} & 0 \\ 0 & \frac{s^2+s+1}{2s^4+3s^3+3s^2} & 0 & \frac{s+1}{2s^4+3s^3+3s^2} \\ \frac{s+1}{6s^4+7s^3+7s^2} & 0 & \frac{6s^2+s+1}{6s^4+7s^3+7s^2} & 0 \\ 0 & \frac{s+1}{2s^4+3s^3+3s^2} & 0 & \frac{2s^2+s+1}{2s^4+3s^3+3s^2} \end{bmatrix}. \quad (5.22)$$

Referring to (5.22), the system has four degrees of freedom, yet each column of the FRF matrix includes only two poles. The FRF matrix shows that torque applied to one axis has no effect on the other (recall that $X_2 = H_{21}F_1 + H_{22}F_2 + H_{23}F_3 + H_{24}F_4$). This makes sense since in the modal model, the motion of each axis depends only on the torques applied to that axis. Indeed, the coupling between the two axes results from the nonlinear terms, which have been relabeled as fictitious torques.

By removing the nonlinear terms it is possible to analyze the motion of two independent systems assuming the simple case where $\tilde{\tau}_1 = \tilde{\tau}_2 = 0$ (the next section discusses how to recover the full nonlinear model). The first system is characterized by the azimuth terms:

$$\begin{bmatrix} 6 & 0 \\ 0 & 1 \end{bmatrix}\begin{bmatrix} \ddot{\theta}_1 \\ \ddot{\phi}_1 \end{bmatrix}+\begin{bmatrix} \dot{\theta}_1-\dot{\phi}_1 \\ \dot{\phi}_1-\dot{\theta}_1 \end{bmatrix}+\begin{bmatrix} \theta_1-\phi_1 \\ \phi_1-\theta_1 \end{bmatrix}=\begin{bmatrix} 0 \\ \tau_1 \end{bmatrix}. \quad (5.23)$$

The second system is characterized by the elevation terms:

$$\begin{bmatrix} 2 & 0 \\ 0 & 1 \end{bmatrix}\begin{bmatrix} \ddot{\theta}_2 \\ \ddot{\phi}_2 \end{bmatrix}+\begin{bmatrix} \dot{\theta}_2-\dot{\phi}_2 \\ \dot{\phi}_2-\dot{\theta}_2 \end{bmatrix}+\begin{bmatrix} \theta_2-\phi_2 \\ \phi_2-\theta_2 \end{bmatrix}=\begin{bmatrix} 0 \\ \tau_2 \end{bmatrix} \quad (5.24)$$

In this context, an optimal control problem definition in physical space may thus be defined as follows:

$$
\begin{aligned}
&\text{Minimize} && J = t_f \\
&\text{Subject to} && \dot{y}_1 = y_3 \\
& && \dot{y}_2 = y_4 \\
& && \dot{y}_3 = \frac{-y_3 + y_7 - y_1 + y_5}{6} \\
& && \dot{y}_4 = \frac{-y_4 + y_8 - y_2 + y_6}{2} \\
& && \dot{y}_5 = y_7 \\
& && \dot{y}_6 = y_8 \\
& && \dot{y}_7 = \tau_1 + y_3 - y_7 + y_1 - y_5 \quad . \qquad (5.25) \\
& && \dot{y}_8 = \tau_2 + y_4 - y_8 + y_2 - y_6 \\
& \left(y_1(t_0), y_2(t_0), y_3(t_0), y_4(t_0)\right) = (40°, 20°, 0, 0) \\
& \left(y_5(t_0), y_6(t_0), y_7(t_0), y_8(t_0)\right) = (40°, 20°, 0, 0) \\
& \left(y_1(t_f), y_2(t_f), y_3(t_f), y_4(t_f)\right) = (0, 40°, 0, 0) \\
& \left(y_5(t_f), y_6(t_f), y_7(t_f), y_8(t_f)\right) = (0, 40°, 0, 0) \\
& && |y_i| \le 1 \,\text{rad/s}, \; i = 3,4 \\
& && |u_i| \le 1.5 \text{ N-m}, \; i = 1,2
\end{aligned}
$$

Figure 49 shows the results of the maneuver optimization. However, because the nonlinear terms are negated, this result is not valid for the nonlinear system. Figure 50 illustrates the maneuver that results from implementing the control history from (5.25) to control the nonlinear dynamics of the original problem definition given by (5.19). Clearly, the nonlinear system does not reach its desired endpoint.

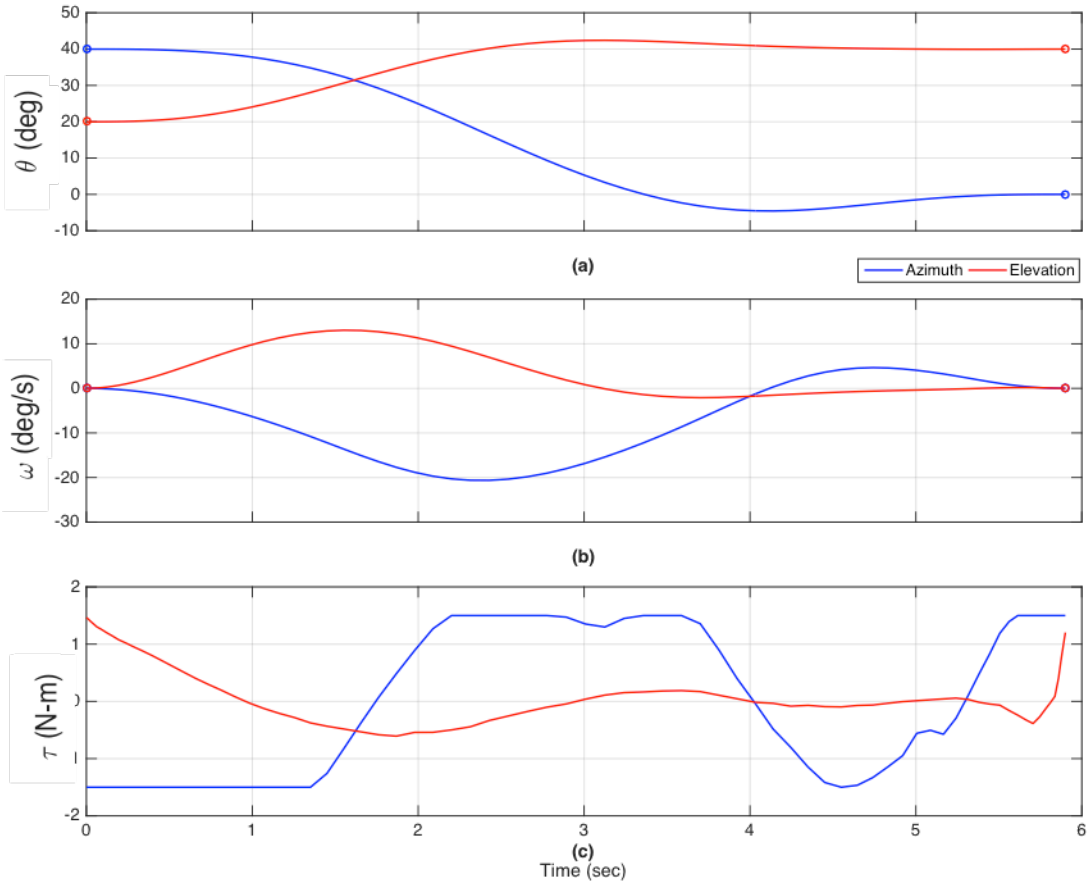

Figure 49. Optimized maneuver for flexible, double-axis gimbal with nonlinear terms removed ($c = k = 1$): (a) link displacement; (b) link angular rates; (c) control torque.

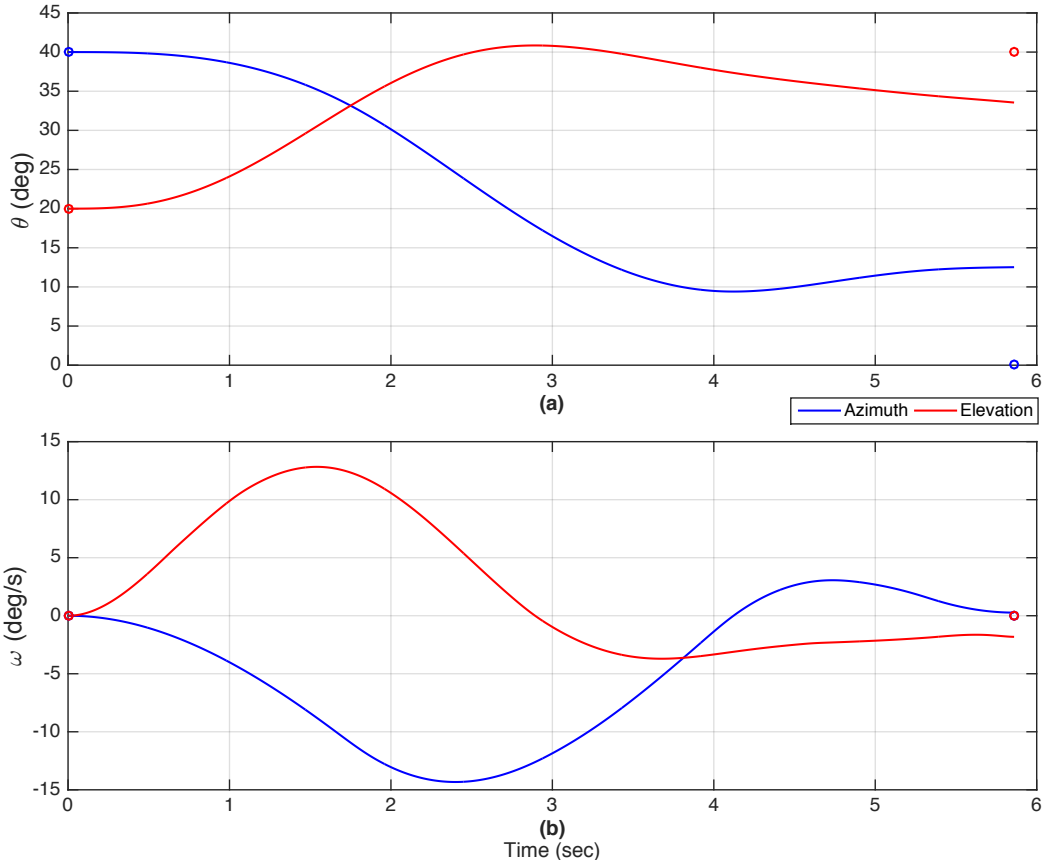

Figure 50. Optimal control solution from Figure 49(c) applied to control the nonlinear dynamics of (5.19): (a) link displacement; (b) link angular rates.

It is now illustrated how to recover the original nonlinear dynamics while operating in the linear modal space. As was shown previously, the nonlinear terms of the DGM may be considered as a fictitious torque input by moving them to the right side of the dynamics equations. Modal analysis for this revised system may be carried out in much the same manner as in previous examples. By treating the nonlinear terms as torque inputs, the modal parameters are effectively held constant throughout the maneuver even as the antenna's configuration modifies the inertia of the system over time. Instead of having to update the modal model at each computational node, the dynamics for optimal control are based on a single nominal modal model. The mass matrix $\mathbf{M} = \text{diag}\begin{bmatrix} 6 & 2 & 1 & 1 \end{bmatrix}$, which produces a constant eigenvector matrix

$$\mathbf{V} = \begin{bmatrix} 1 & 0 & 1 & 0 \\ 0 & 1 & 0 & 1 \\ 1 & 0 & -6 & 0 \\ 0 & 1 & 0 & -2 \end{bmatrix}. \tag{5.26}$$

Matrix (5.26) is used to transform physical to modal coordinates (and vice-versa). The associated modal matrices are

$$\begin{aligned} \overline{\mathbf{M}} &= \mathrm{diag}\begin{bmatrix} 7 & 3 & 42 & 6 \end{bmatrix} \\ \overline{\mathbf{C}} = \overline{\mathbf{K}} &= \mathrm{diag}\begin{bmatrix} 0 & 0 & 49 & 9 \end{bmatrix} \end{aligned}. \tag{5.27}$$

Recall that for proportionally-damped systems the eigenvectors are the same as those of the equivalent undamped system; the modal matrices are scaled the same as the eigenvectors. These matrices yield the following natural frequencies and critical damping ratios:

$$\begin{aligned} \omega_1 &= \omega_2 = 0 \\ \omega_3 &= \frac{\sqrt{42}}{6} \approx 1.0801 \\ \omega_4 &= \frac{\sqrt{6}}{2} \approx 1.2247 \\ \zeta_1 &= \zeta_2 = 0 \\ \zeta_3 &= \frac{\sqrt{42}}{12} \approx 0.5401 \\ \zeta_4 &= \frac{\sqrt{6}}{4} \approx 0.6124 \end{aligned}. \tag{5.28}$$

Note that (5.28) provides two rigid modes (the motion of the DGM links) and two flexible modes representing the joint flex. The equations of motion in modal space are

$$\begin{aligned} 7\ddot{q}_1 &= u_1' \\ 3\ddot{q}_2 &= u_2' \\ 42\ddot{q}_3 + 49\dot{q}_3 + 49q_3 &= u_3' \\ 6\ddot{q}_4 + 9\dot{q}_4 + 9q_4 &= u_4' \end{aligned}, \tag{5.29}$$

where $\mathbf{u}' = \mathbf{V}^T\mathbf{u}$. The first and second equations (for their respective modes) result from purely rigid-body motion.

A new state vector $\mathbf{y} = \begin{bmatrix} q_1 & q_2 & q_3 & q_4 & \dot{q}_1 & \dot{q}_2 & \dot{q}_3 & \dot{q}_4 \end{bmatrix}^T$ is now defined with control $\mathbf{u} = \begin{bmatrix} \tilde{\tau} & \tau \end{bmatrix}^T$ where $\tilde{\tau} = \begin{bmatrix} \tilde{\tau}_1 & \tilde{\tau}_2 \end{bmatrix}^T$ and $\tau = \begin{bmatrix} \tau_1 & \tau_2 \end{bmatrix}^T$. The optimal control problem for the nonlinear system expressed in terms of the fixed modal model with fictitious torque inputs is given as

$$
\begin{aligned}
&\text{Minimize} && J = t_f \\
&\text{Subject to} && \dot{y}_1 = y_5 \\
& && \dot{y}_2 = y_6 \\
& && \dot{y}_3 = y_7 \\
& && \dot{y}_4 = y_8 \\
& && \dot{y}_5 = \frac{1}{7}(u_1 + u_3) \\
& && \dot{y}_6 = \frac{1}{3}(u_2 + u_4) \\
& && \dot{y}_7 = \frac{1}{42}u_1 - \frac{1}{7}u_3 - \frac{7}{6}y_7 - \frac{7}{6}y_3 \\
& && \dot{y}_8 = \frac{1}{6}u_2 - \frac{1}{3}u_4 - \frac{3}{2}y_8 - \frac{3}{2}y_4 \\
& \left(y_1(t_0), y_2(t_0), y_3(t_0), y_4(t_0)\right) && = \mathbf{V}^{-1}\begin{bmatrix} 40^\circ & 20^\circ & 40^\circ & 20^\circ \end{bmatrix}^T \\
& \left(y_5(t_0), y_6(t_0), y_7(t_0), y_8(t_0)\right) && = \mathbf{V}^{-1}\begin{bmatrix} 0 & 0 & 0 & 0 \end{bmatrix}^T \\
& \left(y_1(t_f), y_2(t_f), y_3(t_f), y_4(t_f)\right) && = \mathbf{V}^{-1}\begin{bmatrix} 0 & 40^\circ & \pm 180^\circ & \pm 180^\circ \end{bmatrix}^T \\
& \left(y_5(t_f), y_6(t_f), y_7(t_f), y_8(t_f)\right) && = \mathbf{V}^{-1}\begin{bmatrix} 0 & 0 & \pm 180\,{}^\circ\!/_{\text{sec}} & \pm 180\,{}^\circ\!/_{\text{sec}} \end{bmatrix}^T \\
& && |y_i| \le \mathbf{V}^{-1}\begin{bmatrix} 1 & 1 & 1 & 1 \end{bmatrix}^T \text{rad}/\text{s},\ i = 5,6,7,8 \\
& && \begin{bmatrix} |u_1(t) - \tilde{\tau}_1(t)| \\ |u_2(t) - \tilde{\tau}_2(t)| \\ |u_3(t)| \\ |u_4(t)| \end{bmatrix} \le \begin{bmatrix} 0 \\ 0 \\ 1.5 \text{ N-m} \\ 1.5 \text{ N-m} \end{bmatrix}
\end{aligned}
\qquad . \quad (5.30)
$$

In solving (5.30), the torque limits are applied in modal coordinates through the transformation in the dynamics and the angular rate limit at each node as path constraints. Path constraints are also used to ensure that fictitious torques $\tilde{\tau}$ admit the correct nonlinear effect. It is the presence of these two path constraints that allows the full nonlinear dynamics to be incorporated with the fixed modal model. This aspect represents a new innovation of this thesis.

As in Chapter IV, we first study the behavior of the system without any constraints on flexibility. Figure 51 shows the optimized maneuver resulting from this approach after transformation back into physical coordinates. The azimuth axis rotates the greater angular distance, requiring the greater control torque, but the controller is able to take advantage of the added freedom in the elevation axis. The torque profiles of Figure 51(c) are quite different than those corresponding to computed torque control. This allows the maneuver time to be reduced.

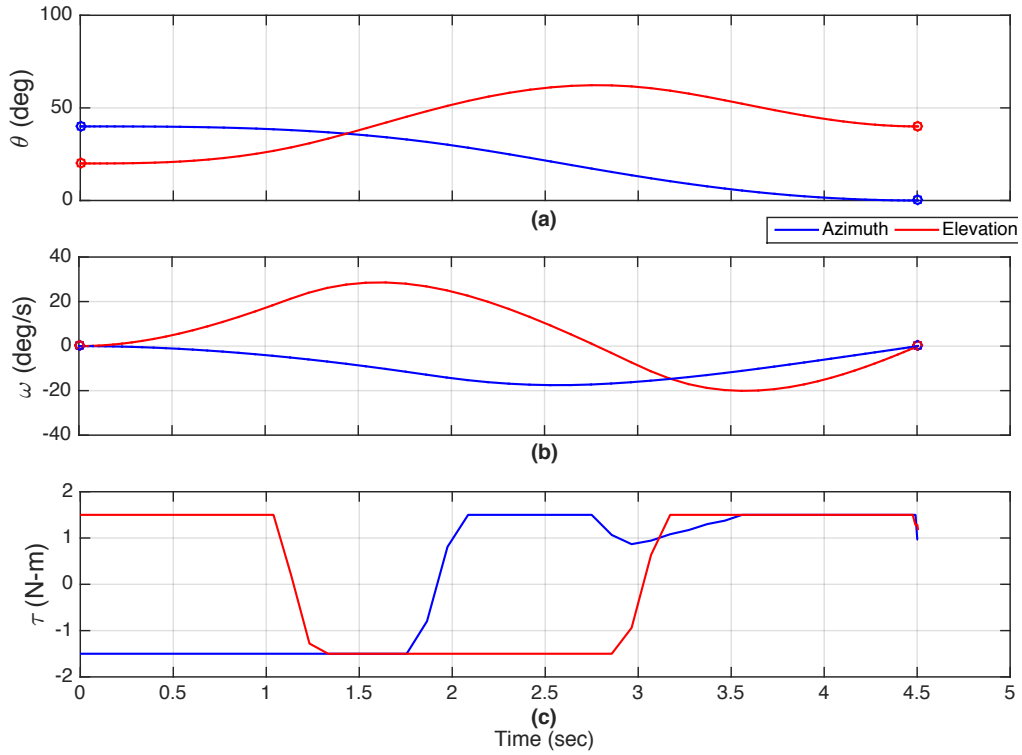

Figure 51. Optimal slew for modal system with fictitious torques: (a) axes displacement; (b) axes angular rates; (c) input torques.

Since we are only concerned with the torques supplied by the spacecraft actuators, only τ_1 and τ_2 are needed to implement the maneuver. The values of the fictitious controls are, however, included for reference (see Figure 52). Applying τ_1 and τ_2 to control the full nonlinear dynamic model produces the correct maneuver, as shown in the first part of Figure 53 (to the left of the vertical dashed line). Thus, the new optimal control problem formulation allows the nonlinear effects to be properly recovered.

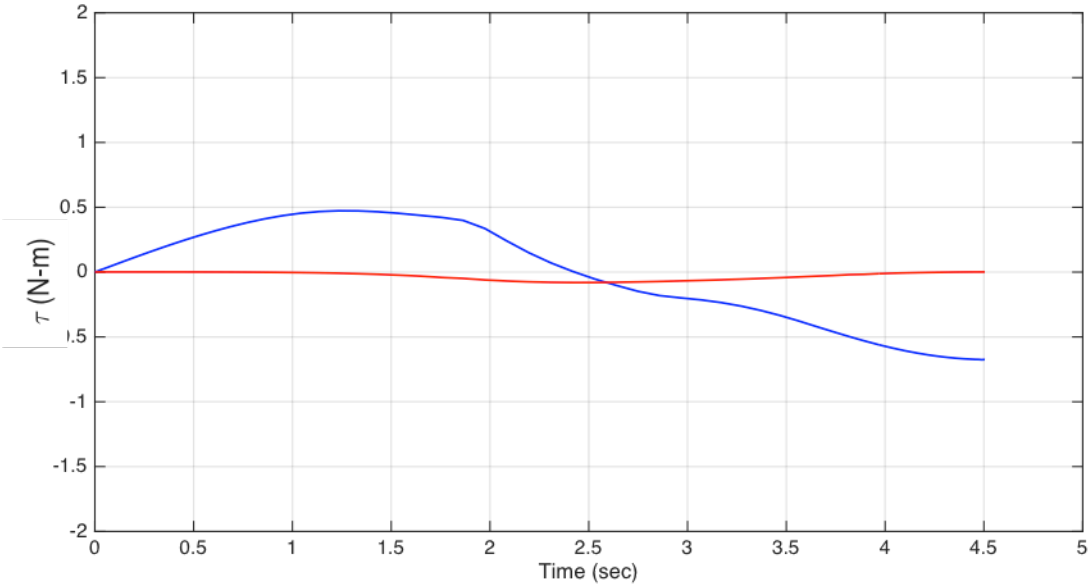

Figure 52. Fictitious control, $\tilde{\tau}$.

In solving the optimal control problem, the vibrations have not been constrained in any way. Figure 53 also shows the behavior of the system after the end of the minimum-time slew (to the right of the vertical dashed line). Because of the energy stored by the “spring” in the joint, each rotor and axis continue to spin. This maneuver is not feasible for operations since it is required for the antenna to remain pointed at its target.

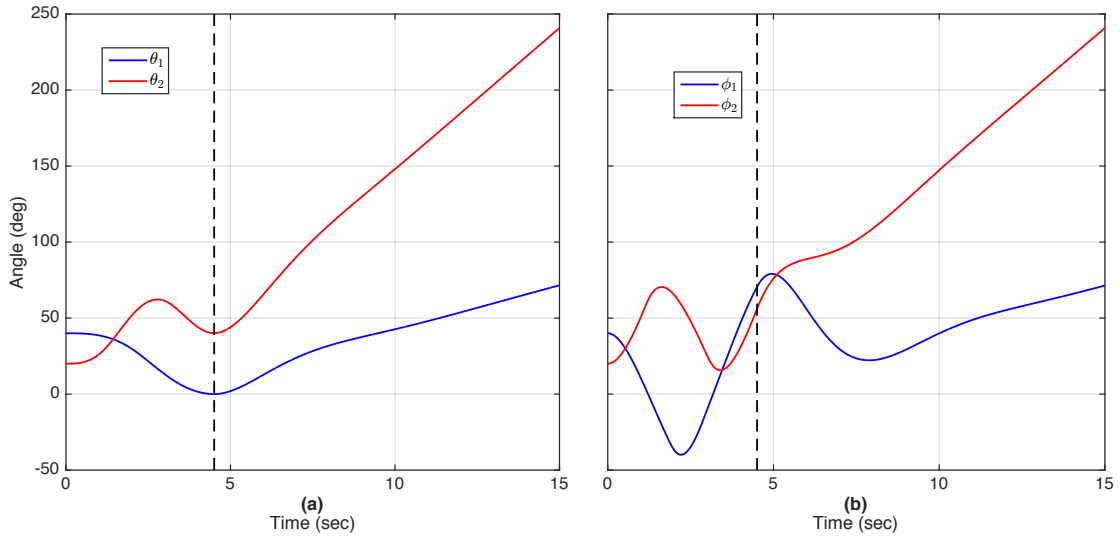

Figure 53. Flexible spillover for minimum-time slew of flexible double gimbal: (a) axis; (b) rotor.

To complete the maneuver with zero flexible motion, the endpoint constraints in (5.30) can be modified to

$$\begin{aligned}\left(y_1\left(t_f\right),y_2\left(t_f\right),y_3\left(t_f\right),y_4\left(t_f\right)\right)&=\mathbf{V}^T\left[\begin{array}{cccc}0 & 40^{\circ} & 0 & 40^{\circ}\end{array}\right]^T\\ \left(y_5\left(t_f\right),y_6\left(t_f\right),y_7\left(t_f\right),y_8\left(t_f\right)\right)&=\mathbf{V}^T\left[\begin{array}{cccc}0 & 0 & 0 & 0\end{array}\right]^T=(0,0,0,0)\end{aligned}. \qquad (5.31)$$

This ensures that the rotor and link angles match at the end of the maneuver so that there is no residual energy stored in the spring. One would expect the slew time to increase because the controller must now force the total motion of the system to zero. Figure 54 illustrates that this conjecture is correct, while Figure 55 verifies that motion ceases at t_f. Note also that in the zero flex case the flexible-body modes q_3 and q_4 are excited (see Figure 56) because they are not otherwise constrained.

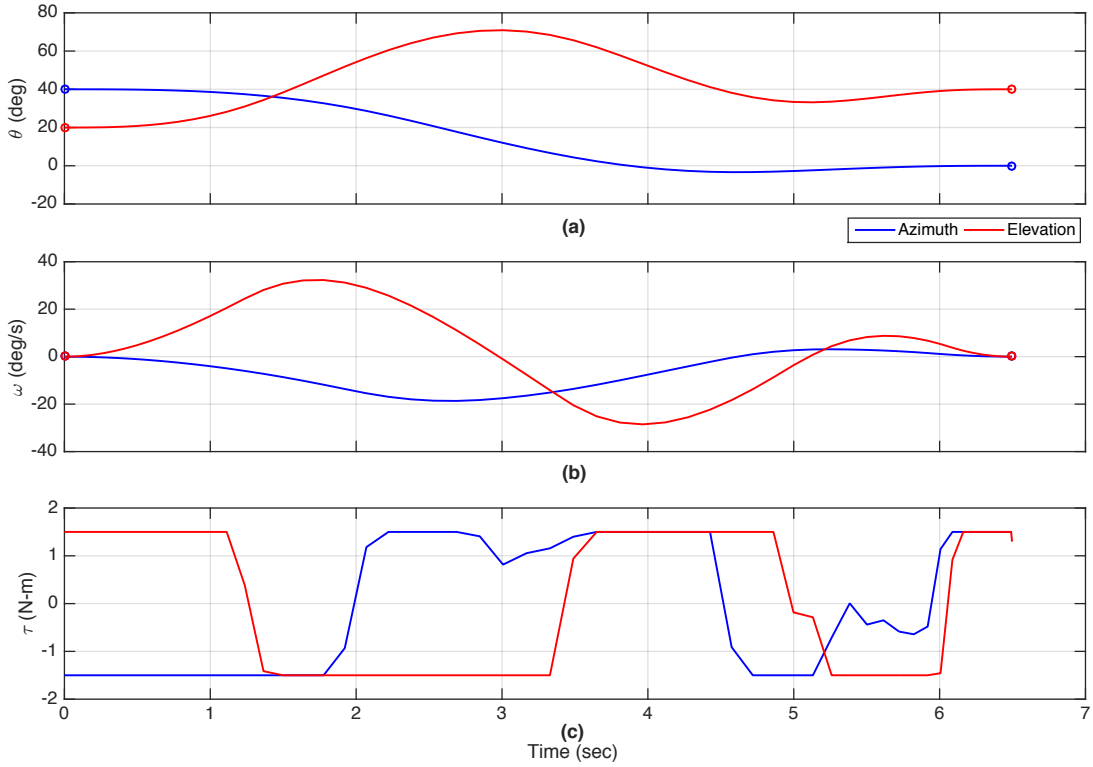

Figure 54. Minimum-time maneuver with endpoint flex constraint, $t_f = 6.496$, $k = 1$: (a) axes displacement; (b) axes angular rates; (c) input torques.

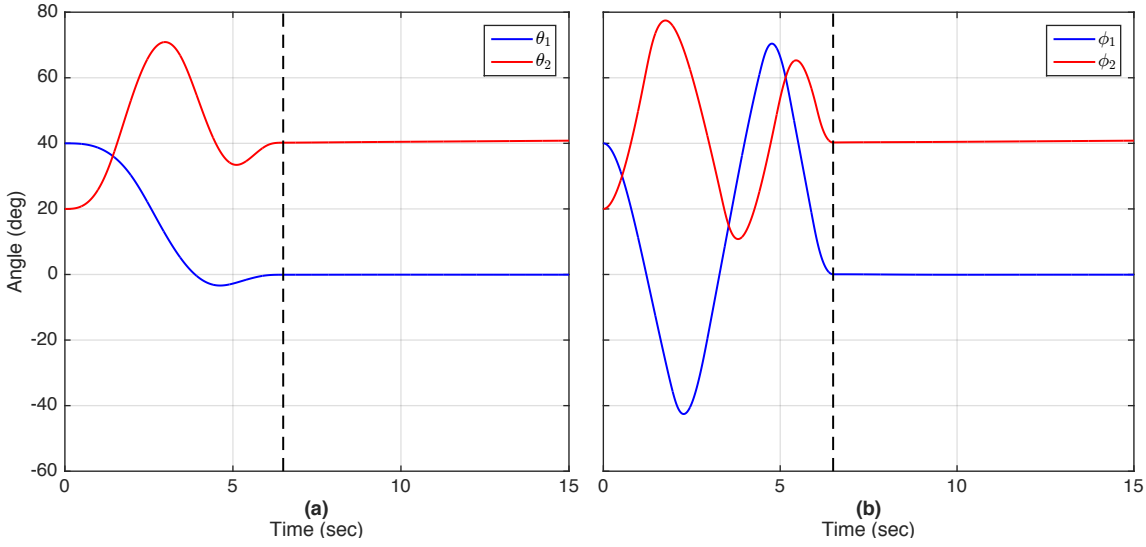

Figure 55. Flexible spillover for minimum-time slew of flexible double gimbal with terminal flex constraints: (a) axis; (b) rotor.

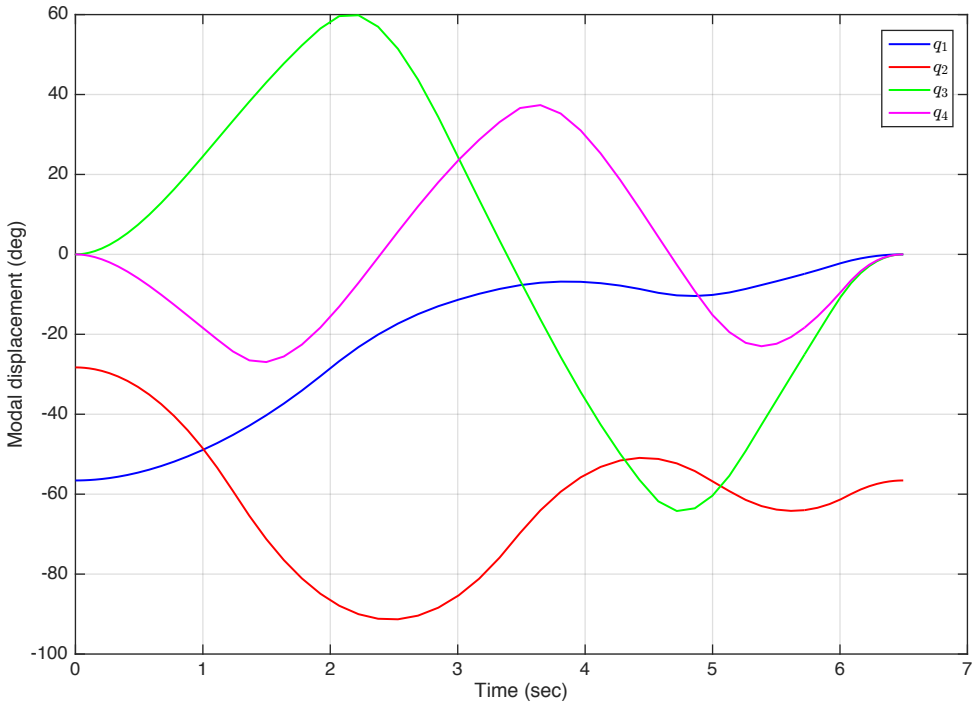

Figure 56. Displacement of system in modal space, zero flex constraints.

We can easily study the effects of limiting flexible-body motion now that we are operating in modal space. In the context of this problem, such a constraint would limit the relative displacement between the rotor and the link. To illustrate this, the following constraint may be added:

$$\begin{aligned} |q_3| &\le 10^{\circ} \\ |q_4| &\le 10^{\circ} \end{aligned} \quad . \tag{5.32}$$

Figure 57 shows that due to (5.32) the maneuver time increases dramatically because the control torque must be modulated to manipulate the relative displacement at each joint.

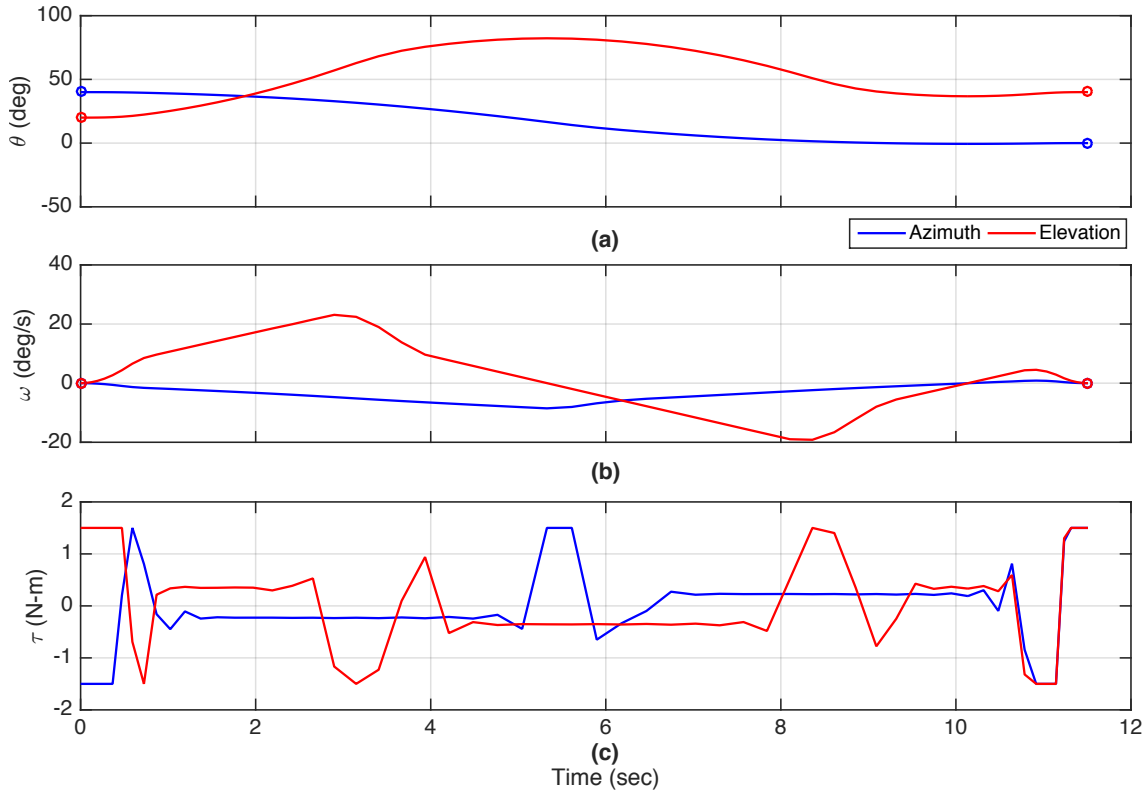

Figure 57. Minimum-time maneuver with flex constraints $\left(k=1,\ t_f=11.51\right)$: (a) axes displacement; (b) axes angular rates; (c) input torques.

Figure 58(a) shows that for this solution the flexible-body modes are properly constrained and that the rigid-body modes respond better to the input torques since much less energy is stored in the spring of the joints. Figure 58(b) confirms that the rotor and axis more closely track each other, showing that constraining the flexible modes allows the elastic displacement to be controlled. The final displacements of the rotors and links are the same, so the antenna does not oscillate at the end of the slew.

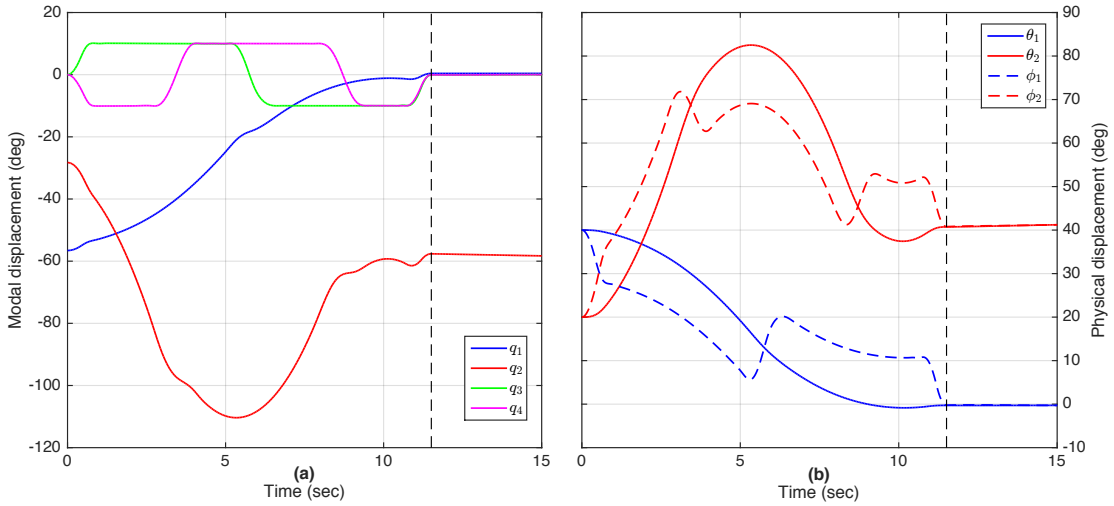

Figure 58. Flexible effects for maneuver with flex constraints: (a) modal space; (b) physical space.

If the endpoint flex constraint on vibrations were removed, the antenna would continue to move after the controller shuts off (see Figure 59). The motion is, however, slower than that in Figure 53 because of the imposed constraint on the displacements of the flexible modes. Thus, the proper combination of constraints on the flexible modes both during the slew maneuver and at the terminal time appears to be the best way to reduce slew times for flexible systems.

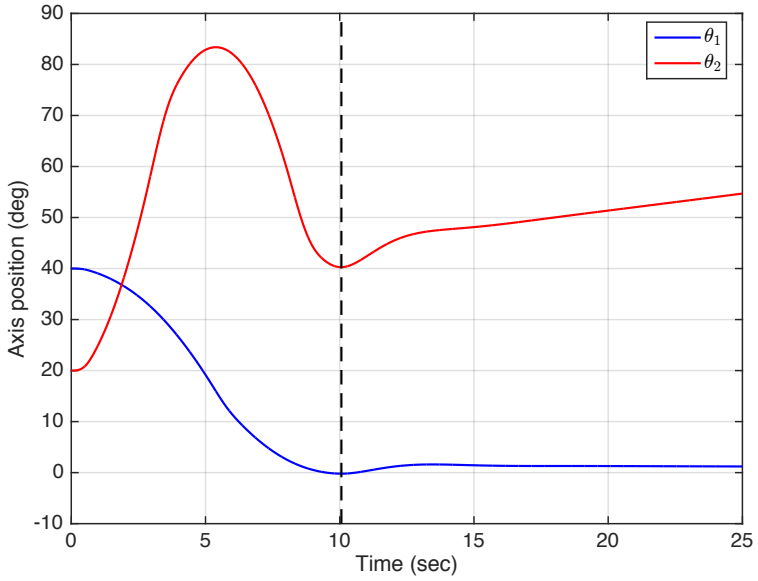

Figure 59. Link angle for maneuver with constrained flexibility.

A comparison of the slew maneuvers for the DGM in this chapter is shown in Table 2. The computed torque maneuver (without the nonlinear terms) executes nearly five times slower than the optimal control maneuvers. The rigid DGM executes the fastest but does not take into account the flexible effects of the system. The optimal control solutions for the flexible DGM provide the most realistic representation of the slew maneuvers while enabling designers to set constraints on flexible motion. Even with the constraints, these slew maneuvers execute faster than those using conventional control.

Table 2. Comparison of slew times (in seconds) for a flexible DGM.

	Computed torque control	**Optimal control**	**Time Savings**
Unconstrained	20	4.5	77.5%
Zero terminal flex	Cannot execute	6.5	67.5%
Zero terminal flex and path constraint	Cannot execute	11.5	42.5%

D. SUMMARY

This chapter demonstrated the application of the optimal control concepts developed in Chapter IV to a nonlinear dynamical system having characteristics of a real spacecraft antenna. The effects of constraining modal displacement both during the maneuver and at the terminal time were discussed. The fastest slews, as expected, occurred with unconstrained modal displacement. These, however, require control effort after the slew to eliminate the spillover motion of the antenna. This chapter showed that the most effective method to constrain flexibility is to define a path constraint and a terminal constraint on flexible motion. This ensures a time-optimal solution can be produced that limits vibrations and ensures the antenna will remain pointed at the desired target after the slew is complete.

The key innovation in Chapter V and this thesis is the separation of the nonlinear terms from the model by representing them as a fictitious torque. This allowed a nominal modal model to be utilized for optimal control while retaining the nonlinear effects as part of the optimal control solution. Using this approach, the modal properties of the system become readily apparent, and the optimal control solution operates as desired when applied to the full nonlinear dynamical system in physical space.

THIS PAGE INTENTIONALLY LEFT BLANK

VI. CONCLUSION

This thesis addressed a problem in satellite design and operations where a control system must accommodate the effects of slewing a flexible appendage while maintaining accurate orientation and minimizing disturbances on the spacecraft bus and other payloads. The TDRS, for example, has limited availability of its single access antennas due to the capabilities of its current control systems. Typical slew maneuvers are executed slowly to reduce disturbances and avoid exciting flexible modes, thereby reducing customer access times. This thesis resolved this issue by determining optimal control effort for rapid slew maneuvers by taking advantage a satellite structure's modal properties rather than discounting them. This thesis presented a new way of finding optimal controls for flexible systems with complicated nonlinear dynamics. Typically, the nonlinearities are simplified or assumed away to make analysis easier. However, this often yields inaccurate results, especially for large slew maneuvers.

A simple linear mass-spring-damper system was used to illustrate the value of modal analysis to understanding the behavior of flexible structures. Modal analysis of a notional spacecraft antenna was then explored by using a 3-DOF mass-spring-damper system model where applied forces cause coupled motion (translation) of each DOF. Computed torque control was used to demonstrate that flexible effects can only be constrained by increasing slew time, which counters the goal for control system design.

Pontryagin's Principle was applied next to the same 3-DOF system, and an optimal control problem was defined. Through modal analysis of the system, the motion of each DOF was uncoupled in modal space. Flexible effects could then be constrained in modal space, so that the optimal control solution could be used to reduce slew times while simultaneously avoiding excitation of the modes. These results showed that it is possible to apply motive forces in a manner that utilizes flexible properties advantageously.

Optimal control and modal analysis were applied to a simplified model of an actual spacecraft antenna mounted on a DGM. The DGM was updated with elastic joints to model flexibility. The nonlinear terms in the equations of motion presented a problem for modal analysis in that the modal model was time-dependent. A novel approach was used to recast the nonlinearities as fictitious torque inputs to the system. This approach removed the time-dependency, yet provided a nominal modal model that accurately described the motion of the original nonlinear system. It also enabled the application of effective flex constraints for optimal control solutions. In the optimal control solution, the controller used the available torque to execute a rapid slew while meeting the desired flex constraints. The maneuver time for the flexible DGM was decreased by approximately 42% compared to the conventional computed torque control solution. Thus, the throughput of an antenna system such as the TDRS single access antenna could theoretically be improved using the results of this thesis.

A. TRANSITION TO PRACTICE

Transforming the dynamics of a system from physical space to modal space has other advantages. Realistically, a control system designer would be given the natural frequencies and damping ratios of a structure rather than having to derive them. If this is the case, optimizing the control is simple. The natural frequencies and damping ratios for each mode easily translate to the coefficients of the modal space dynamics equations, as demonstrated in Chapter II. These coefficients comprise the modal mass, damping, and stiffness matrices and are used to determine the modal behavior of the system. This model can then be incorporated with a nonlinear dynamics model as was done in Chapter V to develop rapid slew maneuvers that accommodate flexible effects according to the specification of the mission.

B. FUTURE WORK

Future research can explore the modeling of the behavior of systems with hysteretic and non-proportional damping. Uncoupling such systems is far more

complicated than those presented in this thesis. The simplified DGM used in this thesis assumed zero distance between the azimuth and elevation rotors and the spacecraft body; future models can incorporate these offsets to study the impact of more complicated dynamics on the controller's ability to minimize vibrations and maintain accurate pointing. This model also assumed unit values for stiffness and damping for both axes and did not address the impact of different constants for each axis. Transition to practice would require working with the correct model for the flexible appendage in question.

This thesis applied elasticity to the gimbal joints of a spacecraft antenna to model the flexibility of the system. Another method would be to model the behavior of a flexible cantilever attached rigidly to a base structure. The results of such a model could then be added to those of a model with elastic joints to extend the applicability of the results.

THIS PAGE INTENTIONALLY LEFT BLANK

LIST OF REFERENCES

[1] B. Menrad. (2014, Oct. 2). Tracking and data relay satellite. [Online]. Available: http://tdrs.gsfc.nasa.gov/tdrs/114.html

[2] M. Thai. (2015, Jul. 23). Tracking and data relay satellite (TDRS) fleet. [Online]. Available: https://www.nasa.gov/directorates/heo/scan/services/networks/txt_tdrs_fleet.html

[3] A. G. Sears, "Design and experimental implementation of optimal spacecraft antenna slews," M.S. thesis, Dept. of Mechanical and Aerospace Engineering, Naval Postgraduate School, Monterey, CA, December 2013.

[4] F. L. Lewis, et.al., *Robot Manipulator Control: Theory and Practice*, 2nd ed., New York: Marcel Dekker, 2004, Ch. 4.

[5] B. Bishop, et. al., "Rapid maneuvering of multi-body dynamic systems with motion compensation," presented at AIAA/AAS Astrodynamics Specialist Conference, San Diego, CA, 2014. Available: doi 10.2514/6.2014-4297

[6] I. M. Ross, *A Primer on Pontryagin's Principle in Optimal Control,* 2nd ed. San Francisco, CA: Collegiate Publishers, 2015.

[7] D. J. Ewins, *Modal Testing: Theory, Practice, and Application*, 2nd ed., Baldock, Hertfordshire, England: Research Studies Press Ltd., 2000, Ch. 1–2.

[8] S. Adhikari, "Damping models for structural vibration," Ph.D. dissertation, Engineering Dept., Univ. of Cambridge, Cambridge, England, 2000.

[9] P. Guillaume. (n.d.). Modal analysis. Dept. of Mechanical Engineering, Vrije Universiteit Brussel, Belgium. [Online]. Available: http://mech.vub.ac.be/avrg/publications/ModalAnalysis.pdf. Accessed Jul. 23, 2015.

[10] P. Avitabile, "Back to basics," *Experimental Techniques*, vol. 26, no. 3, pp.17–18, May 2002.

[11] R. Allemang, “Vibrations: Analytical and experimental modal analysis,” class notes for Mechanical Vibrations II (UC-SRDL-CN-20-263-662), Dept. of Mechanical, Industrial and Nuclear Engineering, University of Cincinnati, Cincinnati, OH, spring 1994. Rev. February 24, 1998, Ch. 5. [Online] Available: http://docslide.us/documents/compendium-558446d89be98.html

[12] H. P. Gavin, “Classical damping, non-classical damping, and complex modes,” class notes for CEE 51 Structural Dynamics, Dept. of Civil and Environmental Engineering, Duke University, Durham, NC, fall 2014. [Online]. Available: http://people.duke.edu/~hpgavin/cee541/ComplexModes.pdf

[13] D. Trumper, “Understanding poles and zeros,” class notes for *2.14 Analysis and Design of Feedback Control Systems*, Dept. of Mechanical Engineering, Massachusetts Institute of Technology, Cambridge, MA, spring 2014. [Online]. Available: http://web.mit.edu/2.14/www/Handouts/PoleZero.pdf

[14] M. W. Spong, “Modeling and control of elastic joints,” *Journal of Dynamic Systems, Measurement, and Control*, vol. 109, Dec. 1987, pp. 310–319.

[15] J. W. Strutt, Baron Rayleigh, *The Theory of Sound*, Vol. 1, 2nd ed., New York: Dover Publications, 1945, Ch. 4.

INITIAL DISTRIBUTION LIST

1. Defense Technical Information Center
   Ft. Belvoir, Virginia

2. Dudley Knox Library
   Naval Postgraduate School
   Monterey, California